UNIVERSITY OF CALIFORNIA,
IRVINE

Nanoporous Quartz Crystal Microbalance: Increasing Sensitivity 1000x and Beyond

DISSERTATION

submitted in partial satisfaction of the requirements
for the degree of

DOCTOR OF PHILOSSOPHY

in Physics

by

Michael James Milgie

Thesis Committee:
Professor Peter Taborek, Chair
Professor Zuzanna Siwy
Professor Ilya Krivorotov

2019

DEDICATION

For my family and friends

TABLE OF CONTENTS

LIST OF FIGURES

LIST OF TABLES

ACKNOWLEDGMENTS

I would like to express the deepest appreciation to my committee chair, Professor Peter Taborek, who has the attitude and the substance of a genius: he continually and convincingly conveyed a spirit of adventure in regard to research and scholarship, and an excitement in regard to teaching. Without his guidance and persistent help this dissertation would not have been possible.

I would like to thank my committee members, Professor Zuzanna Siwy and Professor Ilya Krivorotov, whose research and work is truly an inspiration. I thank them for their feedback on my advancement, and have enjoyed working with them.

I would like to thank my undergraduate professors Dr. Vaman Naik, Dr. Ratna Naik, and Dr. Jin Wang; for introducing me to experimental scientific research, and igniting my passion for it.

I would like to thank the post-docs; Dr. Michelle Lee, and Dr. Masa Nakamoto, for their effort and assistance with our 27 MHz experiments, along with Professor Ken Shea.

I would like to acknowledge and thank my undergraduate students Weiyang Qin, Tejas Dethe, Luke Molitor, Robert Flynn, Andrew Hutchings, and Alisa Snow. They were of great assistance in helping this project stay ahead of schedule and provided an excellent opportunity to develop my leadership skills.

Mark Steinborn and the UCI Physical Sciences Machine shop are acknowledged for assistance in fabrication of tools. Their help has substantially improved my machining capabilities.

I would also like to thank Ferdinand Badescu and Ben Avila for their assistance in learning to fabricate PCBs. I have found this to be a useful and enjoyable addition to my skillset.

Lastly, I would like to thank and acknowledge the support, encouragement, and advice provided by all of the above, along with my family, and many other graduate students and professors. Thank you for pushing me to pursue my passion.

CURRICULUM VITAE

Michael James Milgie

EDUCATION

Ph.D. in Physics **2019**
University of California, Irvine
Dissertation: Nanoporous QCM: Increasing Sensitivity 1000x and Beyond
Chair: Professor Peter Taborek

M.S. in Physics **2019**
University of California, Irvine
Thesis: Calibration of Scintillation Detectors in the MEG II Experiment
Chair: Professor William R. Molzon

B.S. in Physics **2013**
University of Michigan
Thesis: Relaxation of Fe_3O_4 Nanoparticles using Magnetic Hyperthermia
Chairs: Professors Vaman Naik and Ratna Naik

WORK EXPERIENCE

Development Engineer, Lecturer, Teaching Assistant, & Research Assistant **2014 - 2019**
University of California, Irvine

Undergraduate Researcher: Quantum Optics Lab **2013 - 2014**
University of Michigan

Research Assistant **2012 - 2013**
Wayne State University

PUBLICATIONS

Increasing QCM Sensitivity 1000x for Thiol Adsorption using Nanoporous Gold **2019**
Langmuir (in preparation)

Impact and Spreading of Normal and Superfluid Helium Drops **2019**
Mathew Wallace, David Mallin, Michael Milgie, and Peter Taborek
Physical Review Letters (in preparation)

Calibration of the Scintillation Detectors in the MEG II Experiment **2019**
Terence Libeiro, Michael Milgie, Yumei Zhang, and William Molzon
Eur. Phys. J. C (Submitted 2019)

Design of the MEG II experiment **2018**
Eur. Phys. J. C (2018) 78: 380. https://doi.org/10.1140/epjc/s10052-018-5845-6

Multiple Interferometer Interaction Free Measurement using Polarized Light **2016**
Jin Wang, Kevin Pitt, and Michael Milgie
Journal of Physics B: Atomic, Molecular and Optical Physics, Volume 49, Number 4

ABSTRACT OF THE DISSERTATION

Nanoporous Quartz Crystal Microbalance: Increasing Sensitivity 1000x and Beyond

By

Michael James Milgie

Doctor of Philosophy in Physics

University of California, Irvine, 2019

Professor Peter Taborek, Chair

We report experimental results of the adsorption and desorption kinetics of 1-octadecanethiol onto porous gold quartz crystal microbalances (QCM). Fabricated porous gold substrates range in thickness from 75 nm to 3 μm. The porous gold was fabricated using a two-step process of sputtering and etching. First, an alloy of gold and silver was sputtered onto a flat gold QCM with the desired ratio of roughly 70 atomic percent silver and 30 atomic percent gold. Second, the sputtered silver from the alloy was removed by etching in concentrated nitric acid, leaving a gold nanoporous structure on the surface. This porous gold structure on the QCM surface greatly increases the surface area of the sensor, allowing much more thiol to be adsorbed.

Experimental adsorption kinetics are compared to a Langmuir isotherm model. Thiol adsorption on porous QCM in n-Hexane is presented with concentrations ranging from 10nM (5ppb) to 3mM (900ppm). Thiol adsorption and kinetics on a nominally flat gold surface are included for comparison. Optimized sputtering conditions for porous gold substrates lead to a 1000-fold increase of thiol adsorption over flat gold QCM. It follows that the high specific area of porous gold can amplify the final sensitivity of a flat QCM by

more than 3 orders of magnitude. We further present evidence that the three orders of magnitude sensitivity increase we achieve is the maximum enhancement possible when used in liquids for thiol detection. We verify our theoretical model of the QCM, describe our fabrication technique, characterize our substrates, and detail the uses of our porous gold QCM.

PREFACE

The quartz crystal microbalance was first developed in 1959 by Günter Sauerbrey while working on his doctoral thesis at the Technical University of Berlin, Germany [1,2]. By evaporating gold electrodes onto an AT-cut quartz crystal Sauerbrey was able to directly measure the mass of thin films in vacuum to an accuracy of 10^{-10} g [2]. In the 1980s the QCM was immersed into liquids where its use as a surface-analytical tool were realized [1]. Through the 1990s the uses of a QCM in liquid environments were explored and it was found to have many novel uses in soft condensed matter. Over the past 60 years quartz crystal resonators have become common, growing to a 4.5 billion US dollar industry in 2010 and a QCM flew to Mars in 1997 on NASA's Mars Rover [1,2]. In more recent years the QCM has been picking up fame as an emerging equipment for point of care applications in biological clinics, however the unprecedented capability of this technology is not yet fully realized [3]. The QCM is attractive due to its ultra-sensitive detection properties, reproducibility, precision, and accuracy.

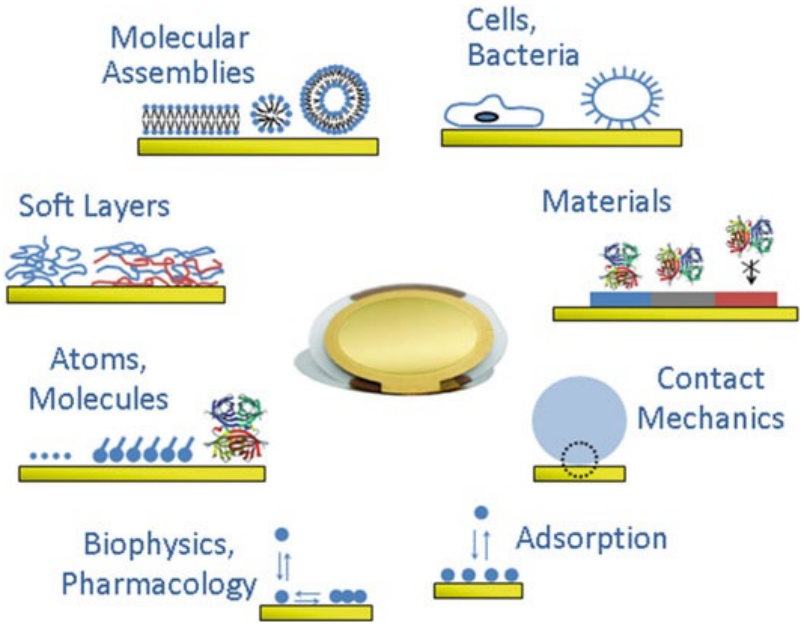

Figure 1: Various soft condensed matter applications of the QCM are displayed above [1].

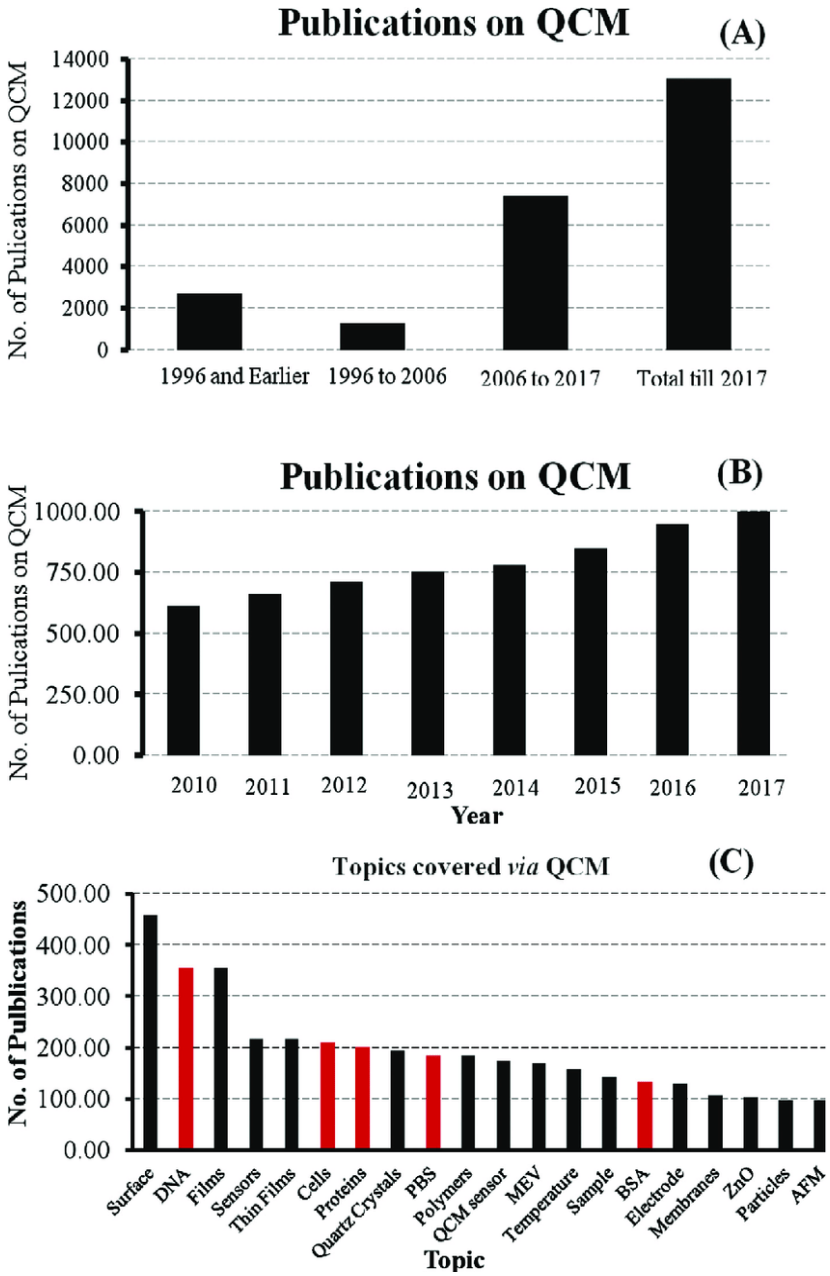

Figure 2: As QCM technology has advanced its use in modern research has grown in popularity. With modern advancements allowing the sensor to work in liquids it has found use in a wide variety of applications. Scopus estimates there are currently more than 14,000 publications focused on the QCM and its various applications [3].

Much recent work has been focused on using the QCM as a real time, on site diagnosis tool. There are currently 17 diseases found to have clear biomarkers in human breath [4]. They include diabetes, lung cancer, breast cancer, Parkinson's disease, and liver failure. Having a tool to detect such diseases in real time has the potential to drastically

change modern medicine. The QCM shows promise towards achieving this potential as a medical sensor, however there is still improvement to be made on commercially available units.

Since the year 2000 enhancements to the traditionally flat QCM sensing surface have been made by introducing porous and other exotic surface structures[5–9]. These surface modifications have thus far been able to improve the sensitivity up to 100 times for specific helium sensing applications. For use as a biosensor, surface modifications have allowed a 10-fold increase in sensitivity. They also allow the limit of detection (LOD) to be improved to below 10 nM or less than 5 ppb as we will demonstrate. This dissertation focuses on the fabrication, characterization, and uses of our porous gold QCM that has increased the QCM sensitivity beyond that of any current publication.

CHAPTER 1: QUARTZ CRYSTAL MICROBALANCE

1.1 The Properties of Quartz

Quartz is a piezoelectric material that has the ability to transform electrical energy into mechanical energy, producing motion and vibration. This vibrational effect is utilized by applying an alternating electric field which causes the quartz crystal to resonate mechanically. Quartz as a mechanical resonator has a high quality, reliability, and accuracy. The quartz is grown and then cut most often with Stress Compensated (SC) and AT orientations. Different cuts of quartz produce different properties for the resonator. These cuts are defined by the two rotation angles theta and phi of the crystal axis. SC-cut crystals have a double rotation with a theta angle of 34° and a phi angle of 22°. This causes SC-cut resonators to oscillate in two planes of motion. This motion in both the x and z directions is called face shear mode oscillation. SC-cut crystals are commonplace in modern digital electronics as a stable clock. They work extremely well in vacuum and air, however their motion produces longitudinal waves in liquids that destroys their resonance [10].

AT-cut crystals have a theta angle of 34° and a phi angle of 0°. This causes the quartz to oscillate in the thickness sheer mode meaning there exists only one direction of oscillation. This allows AT-cut quartz to be used in liquids since it produces no longitudinal waves, and instead drags the liquid only to the viscous penetration depth [1]. These crystals are easily processed as they do not require the precision that SC-cuts require. AT-cut quartz is commonly used to make QCM for applications in vacuum, air, and liquid. This cut gives the QCM good stability and reliability as a mass measuring tool with sub-monolayer accuracy.

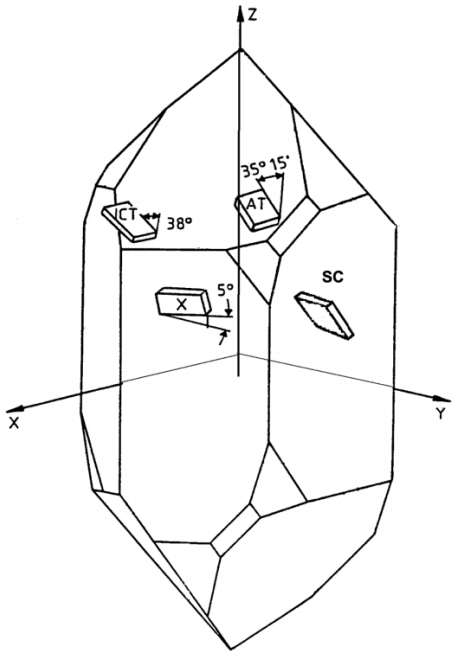

Figure 3: Various cuts of quartz crystal are displayed above. SC-cut quartz is commonly used as a stable clock signal for digital electronics. AT-cut quartz is often used for sensing monolayers of mass in vacuum, air, and liquids[1,10].

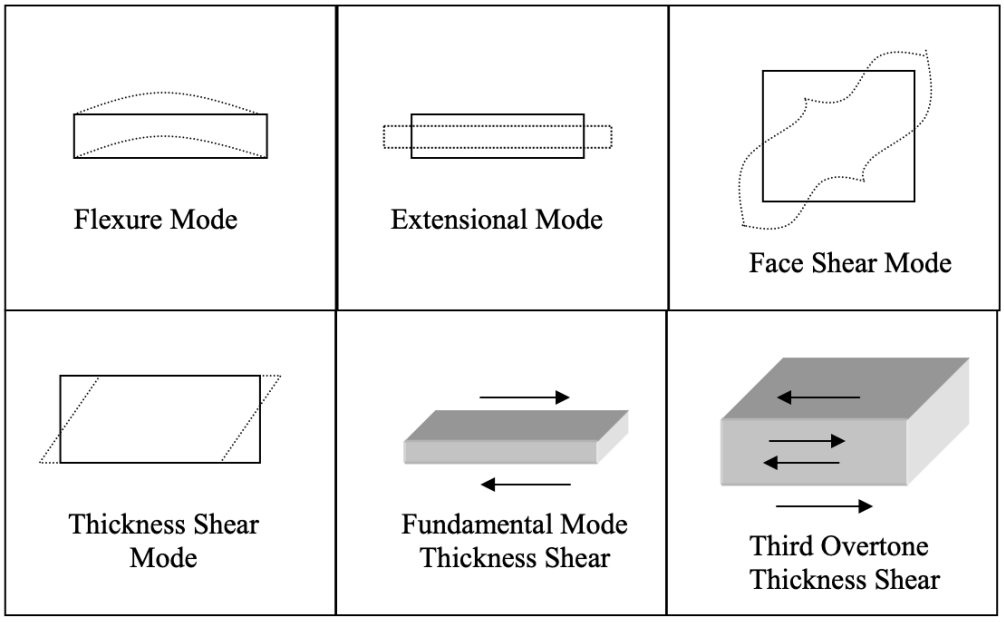

Figure 4: The various modes of mechanical displacement from applied electric field in quartz crystal is displayed above. Common modes of piezoelectric actuators are seen in the flexure and extensional modes. The face shear mode is found in SC-cut quartz and the thickness shear mode is found in AT-cut quartz. These resonators oscillate at odd overtones (1,3,5…) as displayed [11,12].

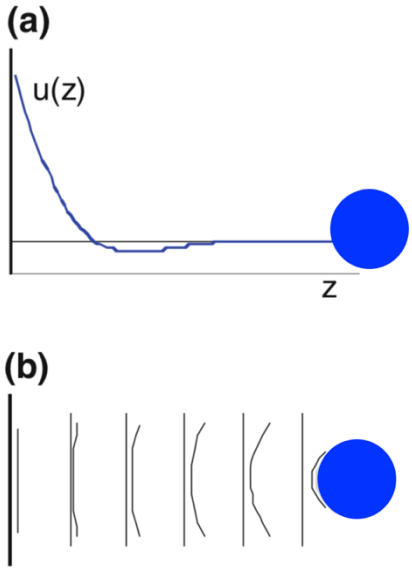

Figure 5: Thickness shear mode waves rapidly decay in liquids and gasses as shown in (a). The typical penetration depth of a 5 MHz oscillator in water is ~250 nm. Mass or objects located outside of this penetration depth are not observed. In contrast, compressional waves which occur in face shear mode oscillators, such as SC-cut crystals, may reflect off objects such as the container in liquid experiments (b) [1].

1.2 QCM Working Principle

A QCM is a quartz crystal disk with a typical thickness of 330 μm and diameter ranging from 1.5 to 2.5 cm. They are most commonly made from AT-cut quartz but are also available with SC orientations. AT-cut crystals were chosen for this experiment as they have an inflection point around room temperature and perform well in liquids. AT-cut crystals are also less expensive and more readily available when compared to SC cut crystals. SC-cut crystals are better suited for lower and higher temperature purposes, and further boast a higher Q than AT-cut crystals.

Once a crystal wafer is properly cut, it then has electrodes evaporated onto both sides. When a voltage is applied to the electrodes on the QCM a shear deformation is produced due to the inverse piezo-effect. When an AC voltage is applied to the QCM that

matches one of the acoustic resonance frequencies of the sensor, the amplitude of oscillation and current drawn becomes large. The quality of the resonance or Q is defined as $Q = f_r/(2\Gamma)$ where f_r is the fundamental resonance frequency and Γ is the half-bandwidth. A QCM can easily achieve quality factors of 10^5 with even higher Q obtainable in cryogenic systems [1].

Despite being called a microbalance a QCM actually measures an areal mass density in units of mass per unit area. Modern versions of the sensor have sensitivity well into the ng/cm^2 range [1]. By depositing a film onto the QCM the thickness of the oscillator is increased. Since the standing shear wave on the QCM has antinodes at the surfaces of the sensor, adding a film increases the wavelength and thus decreases the resonance frequency. A simple mathematical explanation of this is seen in the equation below, where λ is the wavelength of sound, cq is the speed of sound, dq is the thickness of the QCM, and df is the film thickness.

$$f_r = \frac{cq}{\lambda} = \frac{cq}{2(dq+df)} \quad (1)$$

The simple mathematical equation above suggests the frequency shift is proportional to the film thickness. However, in the more detailed analysis to be shown, the QCM actually measures the film's mass per unit area.

The QCM used in this study are 5MHz AT-cut oscillators purchased from Stanford Research Systems (SRS) model number 0100RX1. These crystals have a chromium adhesion layer ~10nm thick and a polished gold 1.27cm diameter sensing surface ~100nm thick [13]. The quartz itself has a 2.54 cm diameter and a thickness of 330 μm. The typical Q of a flat SRS QCM

cleaned and in air is ~12,000 as shown in Figure 8. The larger front electrode with smaller back electrode ensures the entire active area is homogenously covered.

Figure 6: Front (left) and back (right) of the 5MHz SRS QCM used in this study. The shape of the electrodes confines the oscillations to the center of the sensor where the two gold circular electrodes overlap. The gray coating seen is the chromium adhesion layer. The two U-shaped gold surfaces on the back of the sensor allow for both electrical contacts to be on one side. This allows the front of the sensor to be used in liquids, while avoiding any electrochemistry. The larger front electrode is connected to ground to keep electric fringe fields away from the sample while the smaller back electrode is connected to the RF source.

The active area of the QCM sensing surface is not completely uniform, but rather is a distribution with the most sensitive area being found at the center of the electrodes [14,15]. This is related to the amplitude of vibration of the quartz itself in the region of overlap between the two electrodes. It is this center area that is sensitive to mass change at the surface of the QCM causing a frequency change. The sensitivity forms a Gaussian curve that is most sensitive in the direction of the shear mode displacement as seen in the figure below.

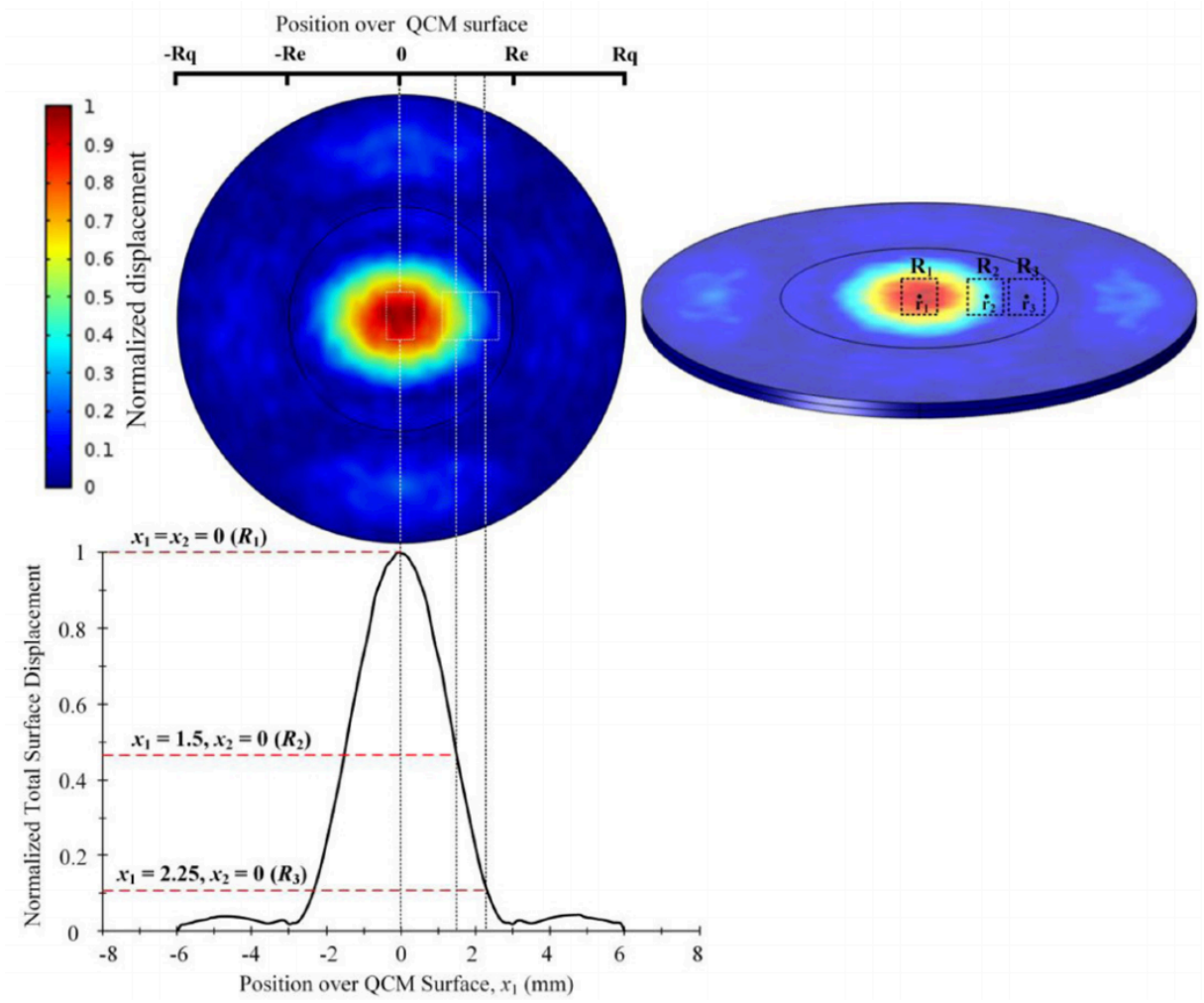

Figure 7: A finite element method (FEM) simulation of the displacement of an AT-cut QCM during oscillation is displayed above. The position of the electrode is displayed with a black circle where the radius is described as Re. The quartz radius is labeled as Rq and shows that the majority of the quartz has no displacement shown in blue. The only observed displacement is found near the center of the overlapped electrodes. This demonstrates the active area of a QCM is most sensitive near the center of the oscillator. The sensitivity is not perfectly symmetric, but rather is slightly elongated in the direction of oscillation. The line plot shows the Gaussian-shaped normalized displacement of the QCM [15].

To measure the frequency of the QCM, we place the crystal into a SRS O100RH Teflon holder that allows the sensor to be used in liquids. The holder is then connected to a HP Keysight 8751A network analyzer that is controlled through LabVIEW. The network analyzer sweeps a specified frequency range and measures the amplitude of oscillation of

the QCM. A typical amplitude plot of a flat SRS QCM in air can be seen below. A fitting function is then used in LabVIEW to fit the data and find the peak resonant frequency as will be later discussed.

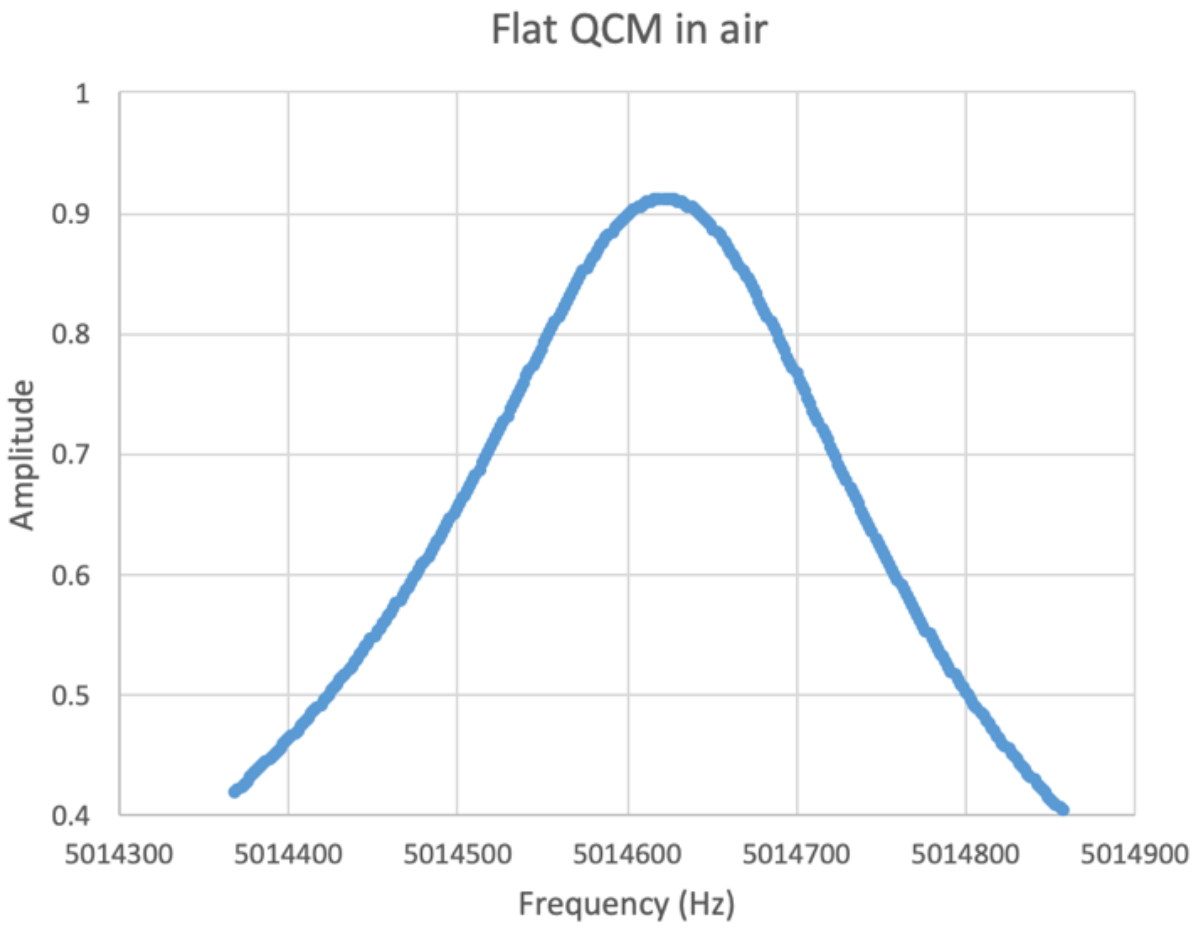

Figure 8: The fundamental frequency of a flat 5 MHz SRS QCM measured in air can be seen above. The amplitude was measured using a network analyzer taking 300 amplitude points over a 500Hz span. The measured Q from the plot above is found to be 11,744.

As was mentioned in equation 1, the thickness of the quartz determines the fundamental resonant frequency of the QCM. With the 5MHz QCM we use for this study we have a quartz thickness of 330 μm providing us good durability for sputtering, cleaning, and liquid experiments. The sensitivity of our 5MHz oscillator is known to be 17.7 ng Hz^{-1} cm^{-2} [13]. This means for a 1Hz shift in frequency, 17.7 ng of mass has been added per square

centimeter. As the thickness of the quartz decreases, the fundamental resonant frequency of the QCM increases, and as will later be discussed in more detail, so does the sensitivity.

Other typical commercially available QCM sensors can be purchased with a 10 MHz fundamental frequency having a thickness of 167 μm with a sensitivity of 4.42 ng Hz^{-1} cm^{-2} from 3t-analytik and OpenQCM [16,17]. Initium produces a higher frequency QCM commercially available, the AFFINIX Q4, that has a fundamental frequency of 27 MHz with a sensitivity of 0.61 ng Hz^{-1} cm^{-2} [18]. The 61 μm thick quartz makes the sensor rather fragile, however we succeeded in fabricating porous gold on these 27 MHz QCM and further increased their sensitivity. The highest frequency QCM that is commercially available has a fundamental frequency of 100 MHz from AWSensors [19,20]. This high fundamental frequency (HFF) 100 MHz sensor has a thickness of 17 μm, a theoretical sensitivity of 0.04 ng Hz^{-1} cm^{-2}, and was used in a recent 2018 study to detect pesticides in honey [21]. From these specifications we can see the fundamental frequency has a linear relationship with the thickness of the quartz. We further note the sensitivity increases with the base fundamental frequency squared, as will be shown in the theory section.

1.3 QCM: Uses and Thiols

Since the QCM has been discovered it has become commonplace in many experiments, and has found new uses more recently as an extremely precise detection tool. QCM are most commonly used to monitor the deposition rate in sputtering and evaporation systems. They have been used as a gas monitoring system in vacuums since 1964 [22]. More recently since QCM use in liquids has become prevalent, they have been highly effective at measuring the affinity of molecules to functionalized recognition sites. By using a gold sensing surface, the QCM is capable of being an extremely selective and sensitive

chemical detector. Gold is also chosen because it is chemically inert and can be used with many solvents [1]. The gold sensing surface is often used to atomically bind with sulfur. Sulfur is found on a chemical molecule known as a thiol and forms a self-assembled monolayer (SAM) on gold. SAMs of thiol on gold are well studied, it is known that the gold-sulfur bond is quite strong taking at least 126 kJ/mol to remove the monolayer [23,24].

This dissertation primarily focuses on the use of QCM sensors to detect thiols. Thiols were specifically chosen for their versatility. Once a thiol is attached to a gold surface, it can then be functionalized to bind with specific agents. Some examples of thiols functionalized to detect a specific target are detection of antibodies, pesticides, biomolecules, explosives, stem cells, DNA, salmonella, and many more [13,21,25–28]. As a medical sensor a QCM with functionalized thiols have been used for real time on-site detection of glucose levels, influenza, food chemical contaminants, and drug resistant bacteria [3,29]. A simple diagram of functionalizing thiols on a QCM can be seen below.

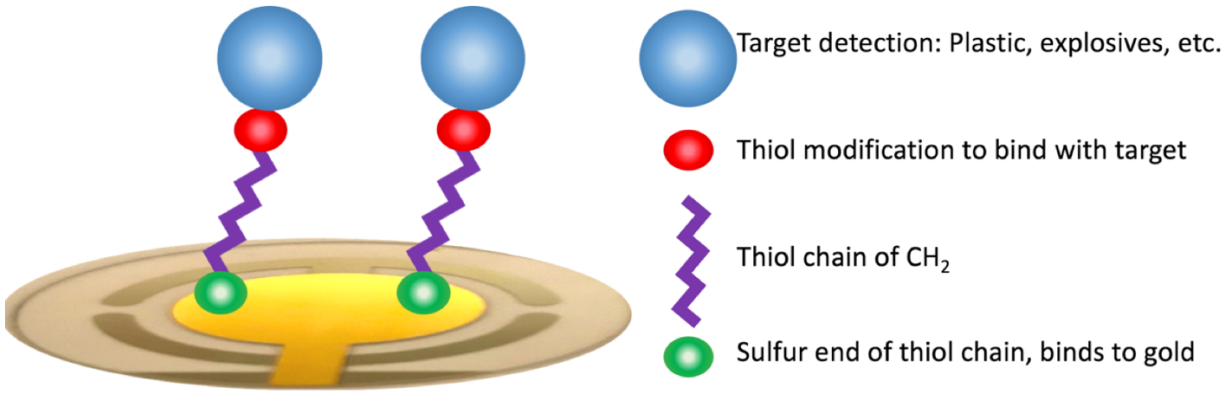

Figure 9: A QCM can be seen above with the sulfur in green binding with the gold substrate. The thiol chain is then modified to functionalize the sensor to detect specific targets such as explosives, biomaterials, or contaminants. By functionalizing a thiol on a QCM the potential uses for a device with such sensitivity and specificity are limitless.

Thiols are an organic-sulfur compound that contain a carbon-bonded sulfhydryl group. They are the sulfur analog of alcohol, where sulfur takes the place of oxygen. Many thiols have a strong smell, resembling that of rotten eggs, and are what makes skunk spray have a bad smell. The smell of natural gas is due to thiols added as an odorant. The primary thiol we have chosen to use for our experiment is 1-octadecanethiol $CH_3(CH_2)_{17}SH$. This specific thiol has been chosen because it has well studied results for flat QCM, giving us a baseline to compare our results with [30–34]. 1-octadecanethiol has a known surface coverage of 330 $\frac{ng}{cm2}$ and forms an ordered monolayer with the thiol tilted at 30° from the norm [35].

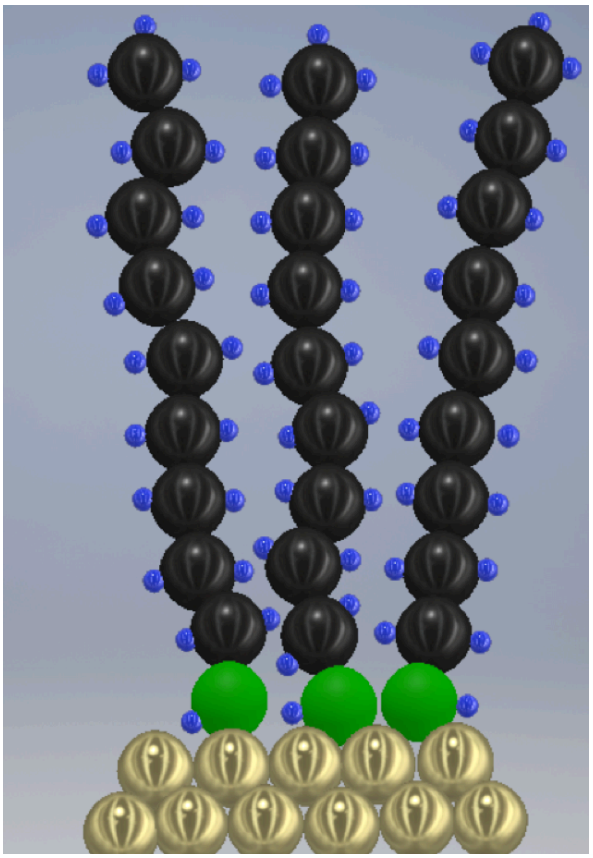

Figure 10: A cartoon of 1-octadecanethiol bonded to a gold surface is displayed above. The sulfur is depicted in green and is bonded strongly to the gold surface. The thiol has a chain of carbon atoms in black, with hydrogen in blue. 1-octadecanethiol is roughly 2nm in length, and has a chain of 18 carbon atoms. In reality the thiol are tilted at 30° from the norm when forming a monolayer on gold. This angle changes based on the substrate.

1.4 Increasing QCM Sensitivity

Various methods exist to increase the sensitivity of the QCM. As described earlier, increasing the fundamental frequency of the QCM increases the base sensitivity with the fundamental frequency squared. However, increasing the fundamental frequency of the QCM also has the negative side-effect of increasing bandwidth, lowering the Q-value, and decreasing stability. For example, with a 5 MHz QCM temperature variations have a small effect on the baseline stability with noise around 2 Hz/hr. In contrast, on a 27 MHz QCM temperature fluctuations of 50 Hz/hr can be observed. This makes temperature stability and measurement crucial for higher frequency QCM. Another consideration in selecting an appropriate QCM for an experiment is penetration depth. As the fundamental frequency increases, the viscoelastic effects increase in importance because the penetration depth of the shear wave decreases. A 100 MHz QCM can easily have a penetration depth smaller than the size of bioadsorbates that are trying to be detected.

A second method employed to increase the stability and sensitivity of the QCM more recently, especially for use in liquids, has been changes to the geometry and setup of the experiment. Before the year 2000 QCM experiments performed in liquids were always performed with both sides of the device submerged in liquid. These older QCM devices were of often connected to electronics using a wire holder that does add extra stress to the crystal wafer. However, in the past 20 years, this setup has changed. Instead of allowing both sides of the QCM to be in contact with a liquid, one side is placed in a pocket of air. By placing only one side of the QCM in liquid, the amplitude and Q of the resonator is improved.

Placing the back side of the QCM in an air pocket with the front side in liquid works well when both sides are at similar pressures. However, it has been shown that slight fluctuations in the pressure of liquid can cause bending of the QCM [36]. This bending can cause resonance frequency responses of the QCM, especially in thinner plates. Caution must be taken to equalize the pressure of the air pocket, and measurement environment when performing experiments at higher or lower pressures. Further, the thickness of the quartz also defines the maximum pressure gradient allowed. Nonetheless these holding devices have given the QCM sub monolayer sensitivity in liquids. Teflon is often used as the holding material as it is chemically inert.

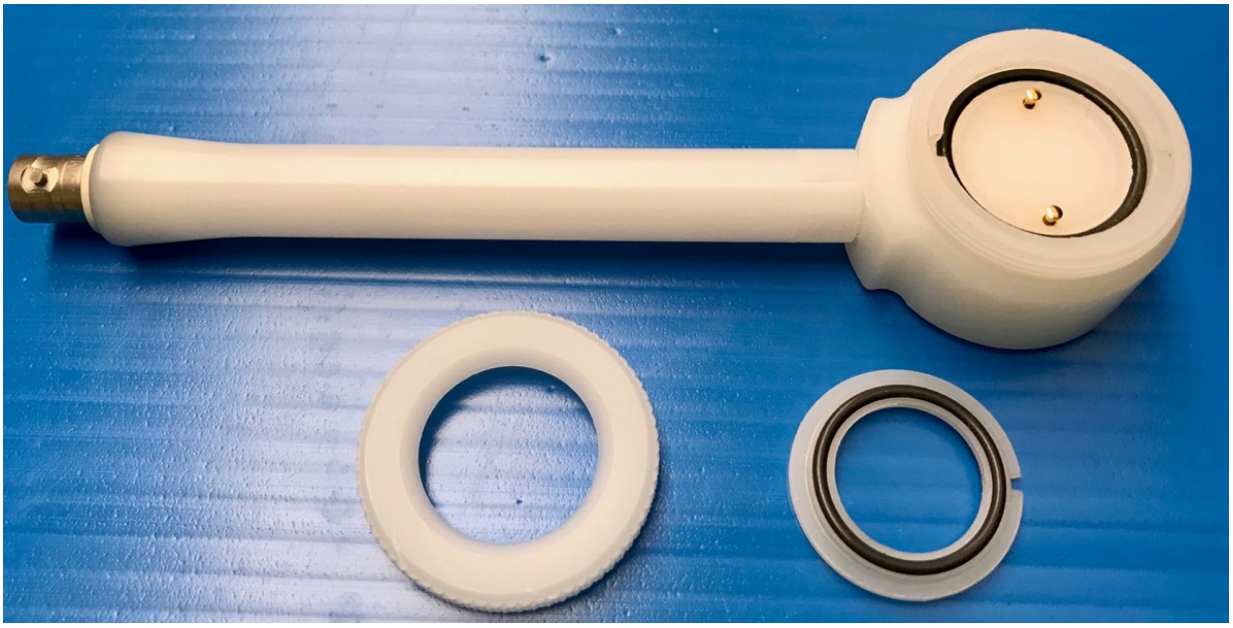

Figure 11: A typical QCM Teflon holder used for liquid measurements. Both QCM electrodes make contact to the two pins in the holder. The Viton O-rings provide an air tight seal to the back face of the QCM. This holder is suitable for use in bulk liquids and can also be modified to work with a flow cell.

While the base frequency of the QCM does determine the mass sensitivity constant, this should not be confused with the limit of detection. The mass sensitivity constant describes how much the frequency of the QCM will change with a given addition of mass. Higher frequency QCM do indeed have a larger frequency change for a given amount of mass being added, however this comes at the cost of bandwidth, Q, and stability. 5 MHz QCM have a short term frequency repeatability of order of 0.1 Hz. This provides a noise equivalent mass of 1.7 ng/cm^2. Using a density of water for example, this translates to a noise equivalent thickness of 17pm [1]. The 5 MHz QCM easily has sub-monolayer sensitivity, but this nonetheless leaves room improvement.

An example of the need for an improved limit of detection is provided by Noort et. al. [37]. In this experiment a flat QCM is used as a biosensor for ligands and compared to a porous gold QCM that increases the sensitivity by a factor of 3. The group found the binding capacity of the ligand was limited on the flat QCM. However, the porous gold QCM substantially extended this binding capacity. They demonstrated this effect by binding immobilized anti-myoglobin at concentrations ranging from 25 to 100 mg/ml. During the experiment the flat QCM showed little to no response from these additions, while the porous QCM respond clearly from each addition of immobilized ligand. Further, the porous gold QCM showed a clear indication of concentration dependent responses. The frequency shift for the porous QCM was larger for higher concentrations of the ligand, as seen below.

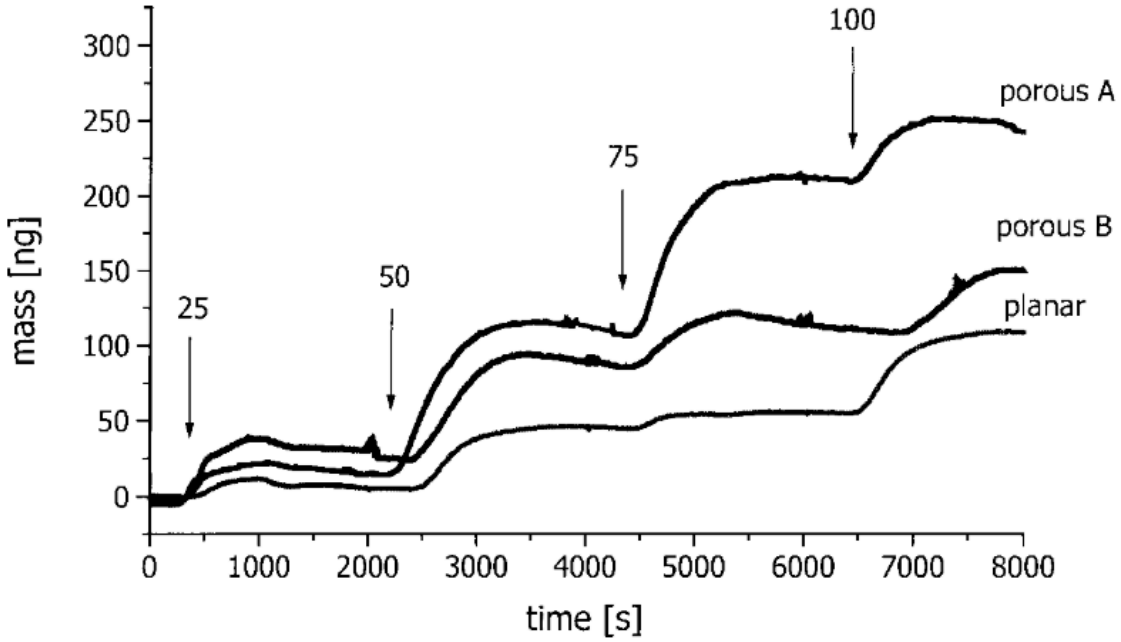

Figure 12: Two porous gold QCM are compared to a traditional flat QCM for the detection of immobilized anti-myoglobin with concentrations ranging from 25-100 mg/ml. The porous gold QCM fabricated for this study was found to have a 3 factor increase in sensitivity. It showed clear concentration dependence on the frequency response until the QCM was fully loaded and could no longer adsorb more ligand [37].

Another interesting use of surface modified QCM was demonstrated by Taborek et. al. [6,38]. In their experiment, porous QCM were used to study superfluid transitions and capillary condensation. A helium isotherm was measured on a standard commercially available QCM and was found to show no hysteresis as is expected. On porous QCM a clear hysteresis loop was discovered, as seen below. In this experiment they start with a QCM in a cryostat under vacuum. They then slowly add helium gas into the cell and measure the thickness of the helium film that is deposited on the QCM. Once vapor pressure is reached at $P/P_o=1$ the helium is slowly removed back to vacuum. The isotherms were used to construct phase diagrams showing hysteresis closure points and superfluid onset. Hysteresis due to capillary condensation was found to exist in all porous gold substrates. Thin films of CaF2 we found to act like rough surfaces, showing no hysteresis until a thickness of 40 nm was reached.

Interestingly this helium isotherm experiment allows for a useful characterization technique for porous QCM. By analyzing capillary condensation and the hysteresis loop associated with it a great wealth of information is available about the structural properties of the porous sample. The characteristic pore length, volume of the porous media, and number of individual cylinders can be calculated [38]. Taborek and Lazarowich found their porous gold had mesopores with a characteristic diameter of 10-15nm, with the number of individual cylinders approaching 0.75 trillion.

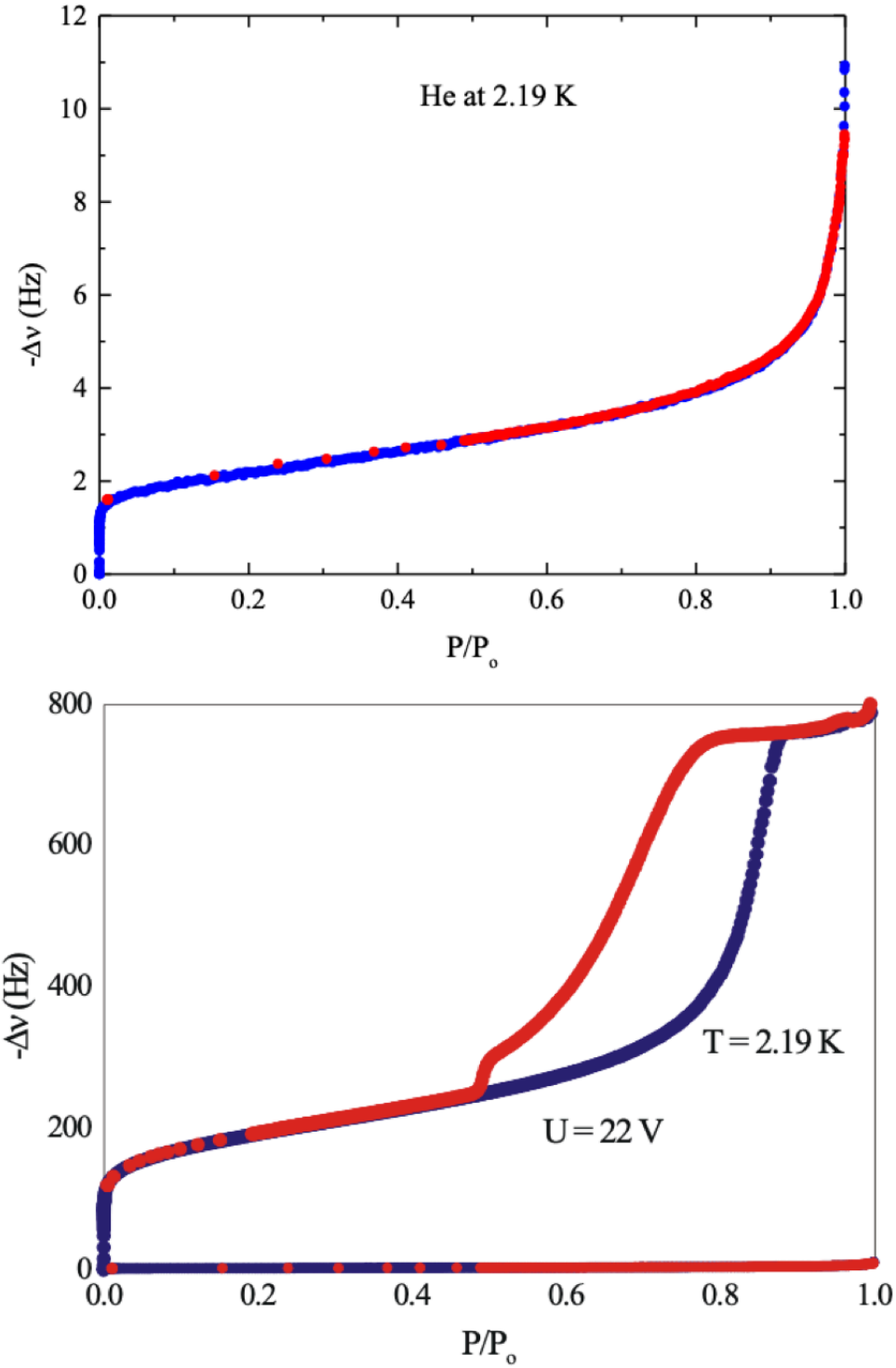

Figure 13: The adsorption and desorption of a helium film is displayed above. In the top image, a flat commercially available QCM is used, and shows no hysteresis behavior as expected. The blue data is the adsorption of helium, whereas the red data is desorption. In a QCM modified with a porous structure, as seen in the bottom image, a clear helium isotherm is found to exist due to capillary condensation. Both the flat and modified QCM results are displayed in the bottom image for comparison [5,6,38].

There are two methods to improve the limit of detection of QCM, both of which were implemented above by Taborek et. at. The first method is to improve the sensitivity of the device by lowering the noise floor. Taborek achieves this first feat by performing experiments in a low temperature environment, with stabilized temperature, and using SC-cut QCM ideal for low temperature experiments. All of these factors lower the noise of the QCM and increase the quality of the measurement. Yet, despite these ideal circumstances, there is still a desire to improve the sensitivity and limit of detection.

The second way to increase the limit of detection for QCM is to increase the number of adsorption sites per unit area with a porous capture layer. Since the QCM sensitivity and limit of detection is dependent on the mass per unit area, increasing the size of the QCM in the x-y plane has no effect on either. A 1 cm diameter QCM or a 1 meter diameter QCM would theoretically have the same base sensitivity and detection limit. However, by increasing the surface area of the QCM in the z-direction the sensitivity can be increased. Adding surface roughness to the QCM does increase the number of adsorption sites on the QCM and thus increases the limit of detection [1,39]. Further, by adding a porous structure onto the surface of the QCM, the sensitivity and limit of detection can be greatly increased, as shown by Noort and Taborek above.

In recent years, enhancements to the traditionally flat QCM sensing surface have been investigated [40]. As the 2001 Noort et. al. example above has demonstrated, even a 3 fold increase in adsorption proves advantageous for biological detection [37]. In 2004 Chan et al. sputtered a porous gold substrate to measure helium 4 films finding a 40x increase in sensitivity[8]. In the same year, Declerck et al. used electrochemistry to grow porous gold finding an 11x increase in 1-octadecanethiol adsorption in liquids [7]. In 2006 Taborek et

al. sputtered a porous gold QCM to increase sensitivity for helium isotherms finding a 64x increase with a 3.3 μm thick substrate [6]. The next year Taborek et al. created a 13 μm thick porous alumina QCM that increased sensitivity of vapor pressure 120x [5]. To our knowledge, no published result has gone beyond this record of 120x enhancement of QCM sensitivity from surface modifications. In 2016 Nature Scientific Report, Bhargava et al. published a novel sea-urchin like structure made of gold on a QCM, allowing a 5x sensitivity increase for the detection of mercury vapors [9]. All of these publications demonstrate the need for a QCM with greater surface area and thus sensitivity. In this study we improve on the previous work reported, however let us first understand the theory behind a QCM and what allows porous surfaces to work so well.

CHAPTER 2: THEORY OF THE QCM

2.1 Overview of QCM Theory

Since the birth of the QCM, much work has been done to theoretically model and understand its resonance. It has allowed the QCM to provide quantitative analysis for a tremendously diverse set of homogeneous and heterogeneous samples. As our understanding of the theory behind the QCM has improved, its use has evolved from measuring thin uniform films in vacuum, to complex materials like DNA in liquids. In this chapter we present and derive some of the major advances in QCM history.

We begin with a simple derivation of one of the first discoveries, the Sauerbrey equation using the wave equation and simple assumptions. We then introduce the consequences of its use in liquids with the penetration depth and the dependence on frequency. This is followed by the breakthrough by Kanazawa and Gordon who in the 1980s discovered a model for the frequency change of a QCM in liquids for the first time. The 1991 results from Martin et. al. are then provided to unify the simultaneous effects of mass and liquid loading using a modified Butterworth-Van Dyke equivalent circuit model.

We then present a detailed derivation of these models based on a parallel plate resonator. This model introduces the small load approximation, described as the single most important equation of the physics of QCM. We use the small load approximation to discuss the limit of detection of QCM, and the importance of base resonant frequency for use in liquids. We move on from there to modern day research in non-ideal films such as DNA, biomolecular objects, and our results with thiols. These results describe how current models do not exactly characterize these films that fall somewhere between a solid and liquid. We then describe the field of porous gold surface modifications, the optical

properties of porous gold, and the electromechanical properties of porous QCM. Next we describe the chemistry and kinetics of thiol adsorption on gold, compare diffusion with the Langmuir isotherm model, and describe thiol desorption. We conclude with how our understanding of the theory of the QCM has allowed us to improve the sensitivity of the device by more than three orders of magnitude.

2.2 A Simple Derivation of the Sauerbrey Equation

To mathematically model the QCM and derive the frequency shift due to adsorbed thin films, we first assume the quartz is infinite in the x, y plane [41]. Letting z=0 be centered at the origin and perpendicular to the plane allows the quartz to be symmetric in z. A standing wave is then described as

$$f(z,t) = e^{-ikct}\,[A\sin(k\,z) + B\cos(k\,z)] \tag{2}$$

The shear mode oscillations require the boundary condition to be stress free at the faces of the QCM giving $\frac{\partial f}{\partial z} = 0$. Taking the derivative of equation 2 with respect to z we get

$$\frac{\partial f(z,t)}{\partial z} = e^{-ikct}\,[k\,A\sin(k\,z) - k\,B\cos(k\,z)] = 0 \tag{3}$$

$$\frac{\partial f\left(\pm\frac{\xi}{2},t\right)}{\partial z} = e^{-ikct}\left[k\,A\sin\left(\frac{k\,\xi}{2}\right) \pm k\,B\cos\left(\frac{k\,\xi}{2}\right)\right] = 0 \tag{4}$$

Since we are modeling the displacement as a conjugate pair rather than a complex number we set B = 0 making the cosine term go to zero, and thus giving us $\frac{k\,\xi}{2} = \frac{N\,\pi}{2}$ where N is odd [38]. Using the definition of a wave $\lambda = \frac{c}{\nu}$ where λ is the wavelength, ν is the frequency, and c is the speed and substituting we get the following.

$$k\,\xi = \pi\,N \tag{5}$$

$$\frac{2\,\xi}{n} = \frac{c}{\nu} \tag{6}$$

This equation describes how the frequency of the QCM is dependent on the properties of the quartz it is made from, specifically the speed of sound in quartz. Solving equation (6), differentiating in finite terms of ξq, and letting $\xi = \frac{cq}{2\,N\,\nu}$ in (5) gives us

$$d\,\nu = -\frac{2\,N\,\nu^2}{cq} d\xi q \tag{7}$$

Therefore, the change in frequency is proportional to the added film on top of the quartz. To put this equation into more useful terms, we use mass = density · volume, and allow the QCM to have a surface area A.

$$\Delta\,\nu = -\frac{2\,N\,\nu^2 \rho_f}{cq\,\rho_q}\frac{m}{A} \tag{8}$$

The above leads us to the famous Sauerbrey result where f is the change in frequency due to rigid mass added to the sample, f_0 is the fundamental resonant frequency, $\frac{m}{A}$ is the mass added per unit area, N is the harmonic of resonance (e.g. 1,3,5…), μ_q is the shear modulus of quartz = 2.947 x 10^{11} g cm^{-1} s^{-2}, and ρ_q is the density of quartz = 2.648 g cm^{-3} [1,2,13,38].

$$\Delta\,f = -\frac{2\,N\,{f_0}^2}{\sqrt{\mu_q\,\rho_q}}\frac{m}{A} \tag{9}$$

The above equation is intended for use in vacuum with perfectly rigid structures on the surface of the QCM. It is excellent at measuring deposition rates in sputtering or evaporation systems. Nearly every modern day evaporation and sputtering system includes a QCM used to monitor the film being deposited. Using the frequency from this QCM along with the Sauerbrey equation, the thickness of the film can be monitored in real time to produce a film of the desired thickness. The Sauerbrey equation even holds up well for thiols on a QCM. We can use equation 9 above to calculate the expected frequency shift

for the thiol used in our experiment, 1-octadecanethiol, with its known surface coverage of 310 - 330 $\frac{ng}{cm2}$ [31,42–44]. Using an ideal 5 MHz flat QCM we calculate an expected frequency shift of 17.5 - 18.7 Hz for a monolayer of thiol on a clean gold surface. This result is in good agreement with our experimental results, along with other publications. However, this equation neglects viscous drag from liquids as we will now discuss.

2.3 QCM Penetration Depth in Liquids

Due to the non-slip boundary condition imposed at the interface between a liquid and solid, when a QCM oscillates the liquid at the surface is pulled with it. This motion of the surface will drag the liquid to a penetration depth δ, and is dependent on the fluid dynamic viscosity η, and density ρ, as seen below.

$$\delta = -\sqrt{\frac{\eta}{\pi f \rho}} \tag{10}$$

Using the above equation, we can calculate the penetration depth for various liquids and demonstrate the effect of higher frequency QCM on this depth as well. For water we use typical room temperature values of $\eta = 1.002 \times 10^{-3} \frac{N s}{m^2}$ and $\rho = 998.02 \frac{kg}{m^3}$.

Liquid	δ at 5MHz	δ at 10MHz	δ at 27MHz	δ at 100MHz
Pure Glycerol	27 μm	19 μm	12 μm	6 μm
Water	253 nm	179 nm	109 nm	57 nm
N-Hexane	166 nm	117 nm	71 nm	37 nm

Table 1: The penetration depths of pure glycerol, water, and n-hexane are displayed above for QCM with various fundamental frequencies. The penetration depth is calculated from equation 10 using typical liquid values at room temperature.

From the above table it is clear that the shear wave of the QCM will penetrate deeper into a more viscous fluid like Glycerol. This high viscosity forces the QCM to drag a large volume of liquid, damping its resonance. This damped resonance decreases the amplitude and broadens the resonance curve. This effect lowers the Q of the QCM in

liquids with a larger penetration depth. There is a tradeoff between sensing depth and the quality of resonance. The QCM has a higher Q in n-hexane than it does in water, however it also cannot sense mass on the surface as deeply into the liquid. As discussed earlier, with higher fundamental frequency the penetration depth also becomes shorter. This effect can be problematic for 100 MHz HFF QCM when trying to detect larger biological molecules.

Since liquid is dragged by the QCM, it causes a decrease in frequency that is dependent on the density and viscosity of the solution. A quantitative understanding of the effects of liquid loading on the QCM is a prerequisite for proper interpretation of experimental results in liquids [13]. Mathematically modeling the QCM in liquids was first done by Glassford, and later by Kanazawa and Gordon [45,46]. Glassford first studied the effect of adding a liquid drop onto a QCM, and found the response of the liquid was less than a deposit of a solid mass of the same mass per unit area. He derived this effect analytically using the Navier-Stokes equation to determine the velocity distribution of the droplet, and Rayleigh perturbation analysis to determine the effect [45]. This effect, as we now know, is largely due to the limited penetration depth of the shear wave in liquids.

2.4 Kanazawa & Gordon Equation

Kanazawa and Gordon later studied the immersion of the QCM in liquids finding it was the solution's properties that determined the effect on the crystal. This discovery allows us to predict the effect of various liquids on the QCM frequency. The equation below describes the frequency change of a QCM due to immersion in liquid. It is dependent on the fundamental frequency of the QCM f_0, the sheer modulus of quartz μ_q, the density of quartz ρ_q, as well as the liquid properties of dynamic viscosity η_L, and the density of the liquid ρ_L.

$$\Delta f_{\text{liquid}} = -f_0^{3/2} \frac{\sqrt{\eta_L \rho_L}}{\sqrt{\pi \mu_q \rho_q}} \quad (11)$$

The Kanazawa and Gordon mathematical model above can predict the change in frequency for a flat QCM in various liquids. In their original 1985 publication they used this equation to successfully model experimental data of varying concentrations of glucose and sucrose in water ranging from 0 to 30 percent by weight [46]. They further verify the model using two separate QCM, one with a fundamental frequency of 5 MHz, and the other 9 MHz. We present the predicted change in frequency for water and n-hexane below for the various frequencies of QCM used in our studies in the table below.

Liquid	**$-\Delta f_{liquid}$ 5MHz**	**$-\Delta f_{liquid}$ 10MHz**	**$-\Delta f_{liquid}$ 27MHz**
Pure Glycerol	31 kHz	87 kHz	390 kHz
Water	0.7 kHz	2 kHz	9 kHz
N-Hexane	0.3 kHz	0.9 kHz	4 kHz

Table 2: Predicted frequency change of flat QCM of base frequency 5 MHz, 10 MHz, and 27 MHz in water and n-hexane. This frequency change is due to the liquid loading of the QCM. It is a frequency change with respect to a base frequency in vacuum. The model used is from Kanazawa and Gordon taking liquid values at room temperature.

A simple experiment can be performed to verify the Kanazawa and Gordon model for a flat QCM system. To do this, one can measure the base frequency of a flat QCM in water, and then measure the change in frequency from this baseline when adding increasing amounts of a second solution. The second solution must be soluble in water and ideally have a larger density and viscosity. By monitoring the weight percentage of the second solution added to water, a curve can be created, and the Kanazawa Gordon equation can be fit to the curve. Glycerol is an ideal candidate for this experiment due to good solubility, larger density, and larger viscosity. Deviations from theory are found with higher concentrations of glycerol below and in the original work of Kanazawa and Gordon.

It is believed these deviations from theory are caused by strains induced by mounting and hydrostatic pressure [46]. The increased penetration depth at these high viscosities also increase the noise to signal ratio, causing more room for error.

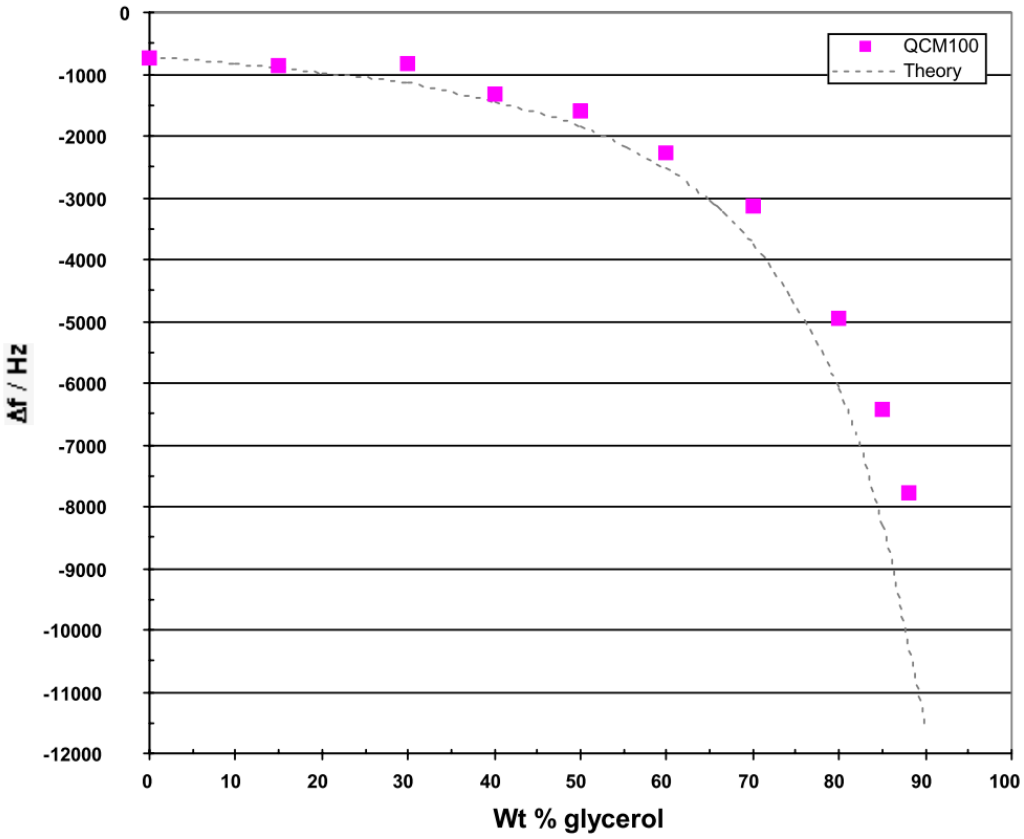

Figure 14: The frequency shift of a flat SRS 5 MHz QCM immersed in water vs the weight percent of added glycerol is displayed above. The data is fit to the Kanazawa and Gordon equation for the dependence of frequency shift in liquid [13,46].

We have now described the theoretical effects of adding solid and liquid masses individually to the QCM and described the effect on the resonant frequency. Adding a solid mass to the surface of a QCM is described well by Sauerbrey seen in equation 9, and decreases the resonant frequency. Immersing the QCM in a liquid also decreases the frequency and is described well by the Kanazawa Gordon equation seen in equation 11. We now wish to combine these two effects, so that we can observe a solid mass loading the QCM while in a liquid environment.

2.5 Modified Butterworth-Van Dyke Equivalent Circuit

In 1991 Martin et. al. derived a model that was capable of combining both the Sauerbrey equation for solid mass with the Kanazawa Gordon equation for liquid loading [47]. This allowed the simultaneous characterization of a QCM with both a surface mass layer and a contacting Newtonian liquid load for the first time. To do this, they used a continuum electromechanical model to derive the electrical admittance for AT-cut QCM, as will soon be described in more detail. The resulting model is a modified Butterworth-Van Dyke equivalent circuit. These circuit elements are explicitly related to physical properties of the quartz, the perturbing mass layer, and the contacting liquid. The model predicts the additive nature of liquid and mass loading in changing the resonant frequency. The liquid and mass loading is indistinguishable when looking at only the frequency, and not the amplitude of the QCM. Due to viscous coupling, the frequency shift due to a liquid and a thin film can be seen below [47]. The solid mass loading is the left term of the equation and the liquid is on the right in equations 12 and 13 below. We note that these equations are simply the sum of the Sauerbrey equation and the Kanazawa Gordon equation we presented above.

$$\Delta f = -\frac{2 N {f_0}^2}{\sqrt{\mu_q \rho_q}} \frac{m}{A} - \frac{2 N {f_0}^2}{\sqrt{\mu_q \rho_q}} \frac{\sqrt{\eta_L \rho_L}}{\sqrt{4 \pi f_0}} \tag{12}$$

$$\Delta f = -\frac{2 N {f_0}^2}{\sqrt{\mu_q \rho_q}} \left(\frac{m}{A} + \frac{\sqrt{\eta_L \rho_L}}{\sqrt{4 \pi f_0}} \right) \tag{13}$$

Having presented the frequency change of the QCM due to simultaneous solid films and liquid loading, let us look at the Martin et. al. modified Butterworth-Van Dyke equivalent circuit model. The prior equations are focused only on the frequency change of the QCM, but more information is available from the amplitude plot of resonance. The

frequency changes of the QCM by itself cannot distinguish between a solid mass and a liquid. However, as will be shown, by modeling the QCM as an equivalent circuit, and observing the amplitude plot of resonance, these two types of loading can be distinguished.

A perfectly solid and rigid mass added to the QCM simply decreases the frequency. However, coupling a viscous liquid to the oscillating surface of the QCM causes both a decrease in resonant frequency and a damping of the resonant oscillation. This damping manifests as an increase in the series resonance resistance R, of the QCM. Independently measuring the resistance of QCM oscillation allows for quantification of the viscous loading at the crystal surface. Both the frequency change and the resistance of the QCM are routinely used as independent measurements of mass and viscous loading. The modified Butterworth-Van Dyke equivalent circuit model was applied to derive the effect of viscous loading on the resistance of oscillation seen below. Where ΔR is the change in series resistance, n is the number of sides in contact with liquid, $w_s = 2\pi f_s$ is the angular frequency at series resonance, and L_u is the inductance of the QCM in air unperturbed with a typical value in mH [13,47].

$$\Delta R = \frac{n w_s L_u}{\pi} \left(\frac{\sqrt{2 w_s \eta_L \rho_L}}{\sqrt{\mu_q \rho_q}} \right) \tag{14}$$

With the above equation we can predict the change in resistance caused by changing the viscosity of a solution. We showed earlier the Kanazawa Gordon equation works well to predict the frequency change by adding glycerol into water. We can do the same with the modified Butterworth-Van Dyke equivalent circuit model above to predict the change in resistance using the same experiment. We note our oscillator works well up until about 88 percent glycerol by weight, after which the resistance becomes too great to overcome.

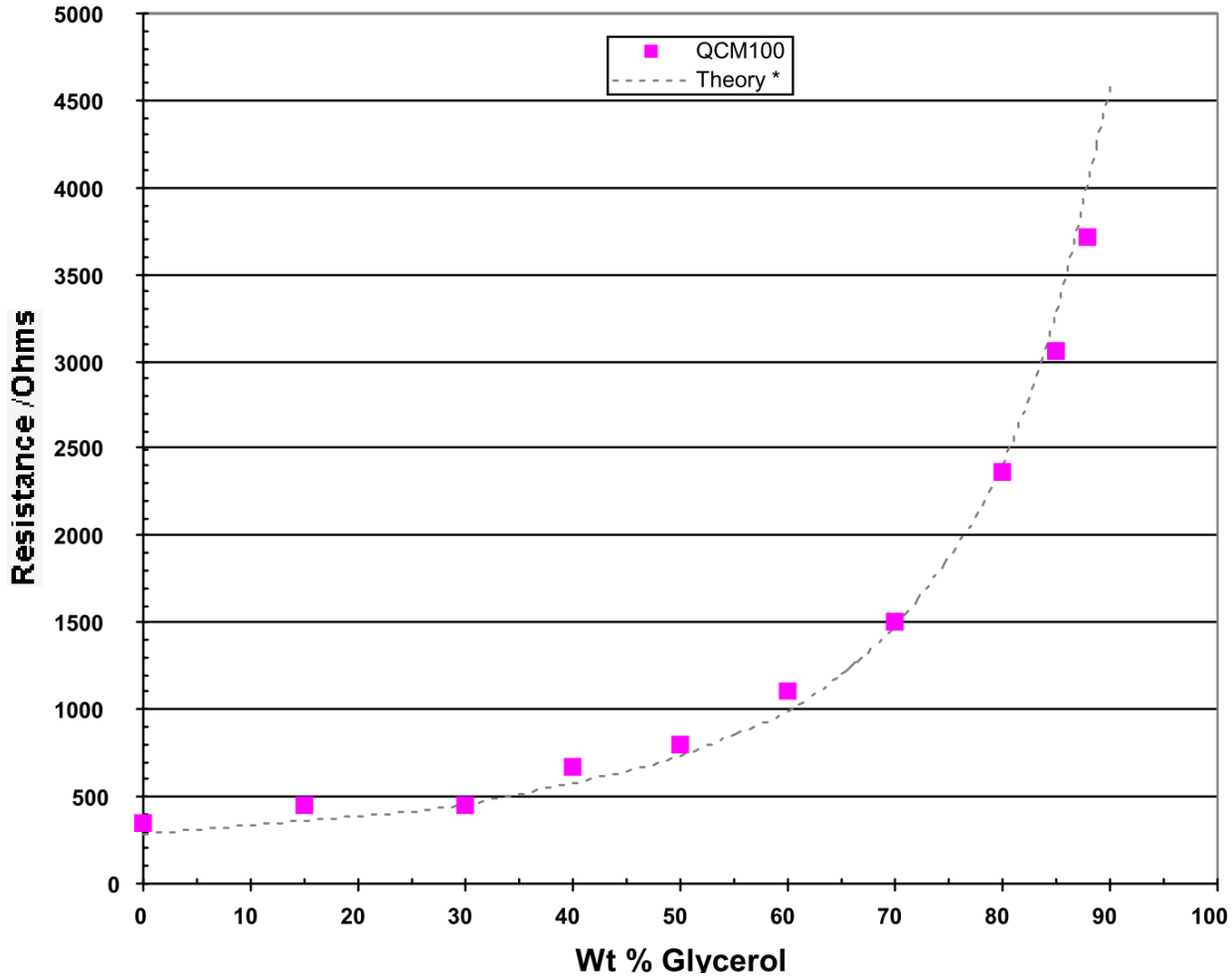

Figure 15: The resistance change of a flat SRS 5 MHz QCM with one side immersed in water vs the weight percent of added glycerol is displayed above. The data is fit to the modified Butterworth-Van Dyke equivalent circuit model described by Martin et. al. for the dependence of resistance on a change in the viscoelastic properties of the liquid [13,47]. The model fits the experimental data exceeding well until the viscosity becomes too great for the QCM to oscillate.

Simply put, the viscoelastic effects of liquids force the QCM to drag more mass with the its motion. This additional liquid mass is dragged to the penetration depth, and damps the oscillatory motion of the QCM. This dampening of the QCM in the model of a simple circuit equates to a resistive term. Theory predicts that perfectly solid and ridged mass added to the surface has no resistive term, and thus only changes the frequency of the QCM, but not the amplitude. However, liquids do carry a resistive term for the QCM due to their

viscoelastic properties and the no slip boundary condition.

If the simplified equivalent circuit model of the QCM had no resistance, we would get a perfect amplitude of 1. However as seen in Figure 8, the amplitude for a clean and unloaded QCM is 0.92 in air. The resistance for this flat QCM oscillating in air comes primary from three sources. The wires connecting the QCM to the network analyzer have a finite resistance, this term is small but nonetheless non-negligible. Longer wires do indeed increase the resistance of the system, and much work is often done experimentally to place the QCM as close as possible to the measuring system. Secondly, even air causes an increase in dissipation when compared to vacuum. Finally, the QCM itself has some finite intrinsic dissipation dependent on the volume and frequency of the quartz. Nonetheless all these factors combined produce a roughly 8% smaller amplitude in air with ~30 cm of wire than a perfect resonator could achieve in absolute vacuum. This baseline level of dissipation is relatively minor and inconsequential to most QCM experiments.

In the modified Butterworth-Van Dyke equivalent circuit a frequency shift of the QCM is modeled as an inductance term. This inductance term changes frequency of the QCM independently of the amplitude or resistance of the oscillator. Inductance is found in both liquid loading and mass loading causing a downwards shift in frequency and indicate mass has been added to the sensor. While both liquid and solid mass have an inductive term, each has its own contribution to the resonant frequency as they depend on slightly different variables. This effect is analogous to the effect on frequency described above in the Sauerbrey and Kanazawa Gordon equations. The liquid inductance is dependent on the density and dynamic viscosity of the liquid. Whereas the solid mass inductance term is dependent on the density of the thin film. The QCM itself also has intrinsic capacitive,

resistive, and inductance terms. The governing equations for the modified Butterworth-Van Dyke equivalent circuit are displayed below. The area term in the QCM intrinsic capacitance is the electrode area.

$$C_{QCM} = \frac{8\,\xi^{2}\,A}{\pi^{2}\,N^{2}\,\mu_q\,h} \tag{15}$$

$$L_{QCM} = \frac{1}{w_s{}^{2} C_{QCM}} \tag{16}$$

$$R_{QCM} = \frac{\eta_q}{\mu_q\,C_{QCM}} \tag{17}$$

$$\Delta\,L_{solid} = \frac{2\,L_{QCM}\,w_s\,\rho_s}{N\,\pi}\frac{1}{\sqrt{\mu_q\,\rho_q}} \tag{18}$$

$$\Delta\,L_{liquid} = \frac{L_{QCM}\,w_s}{N\,\pi}\left(\frac{\sqrt{2\,\eta_L\,\rho_L}}{\sqrt{w_s\,\mu_q\,\rho_q}}\right) \tag{19}$$

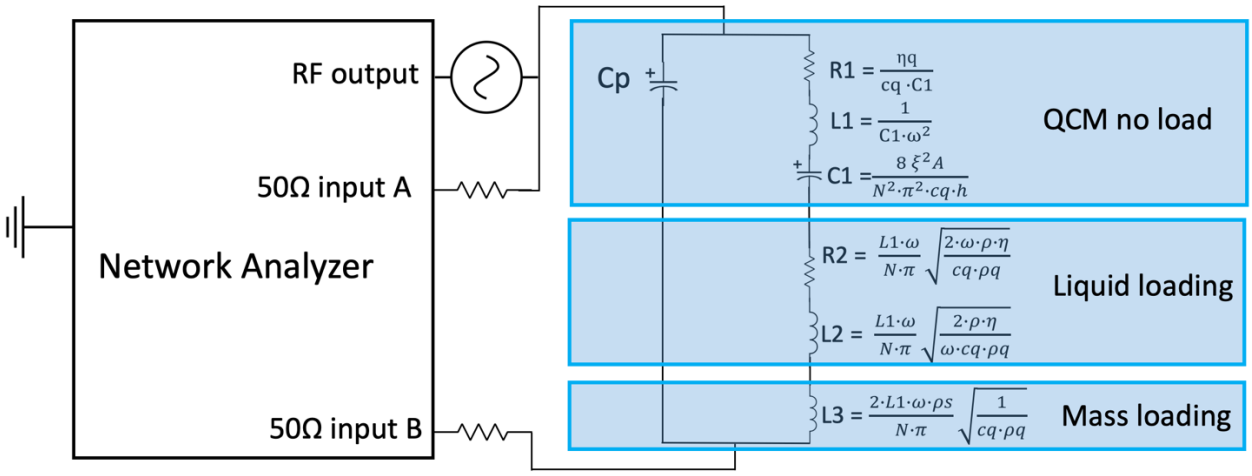

Figure 16: The modified Butterworth-Van Dyke equivalent circuit for a QCM can be seen above connected to a network analyzer. The RF output is tied to input A and connected to the back side of the QCM to drive the oscillator and measure the input power. The front face or liquid side of the QCM is connected to input B to measure the output power and allow an amplitude plot to be measured. The QCM itself is an RLC circuit, with a liquid loading term having resistance and inductance, whereas mass loading only adds an inductance. Liquid loading depends on the viscosity and density of the substance being used [46]. Mass loading is dependent on the density of the material binding with the surface of the QCM [48].

2.6 Acoustic Impedance Model

An alternative way to model the QCM as an equivalent circuit is based on treating it as a parallel plate resonator. In this model the QCM acts as an acoustic impedance. Its properties are constrained in the stress-velocity ratio at the interface between the sample and the crystal. This model is the analog of a transducer with the acoustic ports closed. In QCM sensing, rather than emitting a signal, it instead responds to stress exerted by the crystal. This equivalent circuit of a piezoelectric resonator is displayed below.

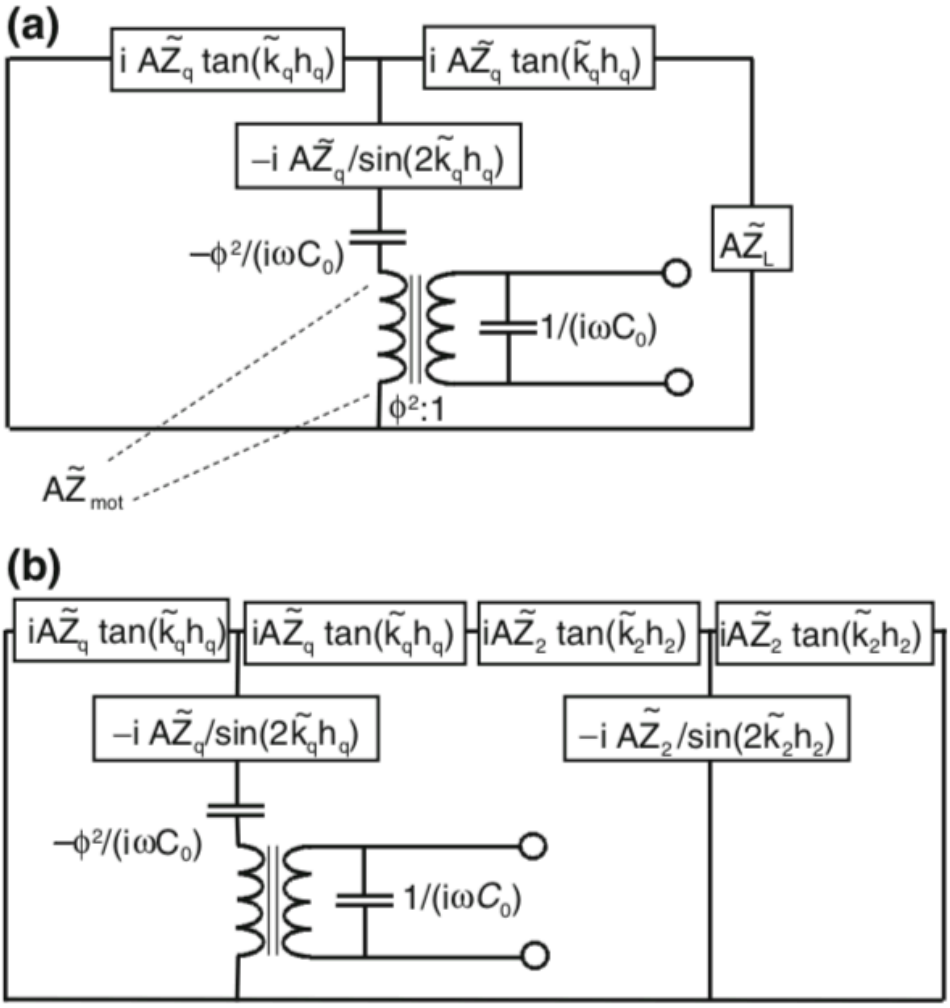

Figure 17: A simplified model of the QCM is displayed above treating it as a parallel plate resonator. In image (a) the sample is represented by the load impedance AZ_L. Z_L is multiplied by the area to turn the device into a mechanical impedance. In image (b) the piezoelastic resonator is loaded with a viscoelastic material. Kirchhoff electrical rules apply everywhere [1].

From applying Kirchhoff laws to the above figure we can arrive at the mechanical impedance of the QCM seen below.

$$\tilde{Z}_{mot} = -\frac{\phi^2}{i\omega C_0} - \frac{i\tilde{Z}_q}{\sin\left(2\tilde{k}_q h_q\right)} + \left(\left(i\tilde{Z}_q \tan\left(\tilde{k}_q h_q\right)\right)^{-1} + \left(i\tilde{Z}_q \tan\left(\tilde{k}_q h_q\right) + \tilde{Z}_L\right)^{-1}\right)^{-1} \quad (20)$$

We now use a Taylor expansion in k_q around $k_{q,oc} = n\frac{\pi}{2h_q}$

$$\begin{aligned}\tilde{Z}_{mot} &\approx -\frac{\phi^2}{i\omega C_0} + \frac{i\tilde{Z}_q}{2}\left(\tilde{k}_q h_q - \frac{n\pi}{2}\right) + \frac{\tilde{Z}_L}{4} \\ &= -\frac{\phi^2}{i\omega C_0} + i\frac{n\pi}{2}\frac{\tilde{Z}_q}{2}\left(\frac{2\tilde{k}_q h_q}{n\pi} - 1\right) + \frac{\tilde{Z}_L}{4} \\ &= \frac{1}{4}\left(-\frac{4\phi^2}{i\omega C_0} + in\pi\tilde{Z}_q\frac{\tilde{\omega} - \tilde{\omega}_{OC}}{\tilde{\omega}_{OC}} + \tilde{Z}_L\right)\end{aligned} \quad (21)$$

The above equation found from the simplified circuit above can be used to derive the Kanazawa Gordon equation for liquid loading we previously described. This independent model produces the same result when solving for the angular frequency term. This equation plays central importance in deriving the small load approximation. The small load approximation provides another method to relate the load on the QCM to a frequency shift.

2.7 The Small Load Approximation

To derive the small load approximation, we begin with equation 21 above. We let the angular frequency be the resonance frequency with the load impedance being set to zero. We will call w_r the loaded resonance. We find the frequency shift for the small load approximation below.

$$\frac{\Delta\tilde{f}}{f_0} = \frac{1}{2\pi}\frac{\tilde{\omega}_r - \tilde{\omega}_{ref}}{f_0} = \frac{i}{\pi Z_q}\tilde{Z}_L \quad (22)$$

For the small load approximation, the load Z_L must be smaller than Z_q, the impedance of the quartz. This means to be true, frequency changes measured must be much smaller than the resonant frequency of the QCM. In general, for most applications this holds true, as the measured frequency shift is usually many orders of magnitude smaller than the resonant frequency.

Equation 22 has been described as the single most important equation of the physics of the QCM [1]. As long as the measured frequency shift is much smaller than the fundamental frequency, the shift is proportional to the load impedance at the crystal surface. This equation allows the frequency shift to be calculated for a huge variety of material. It can be used for samples like sand, cells, a droplet, or any other complicated heterogeneous material. The concept of load impedance tremendously broadens the application range of a QCM. It is a link between the QCM and complex samples. If the stress-velocity ratio of the sample can be calculated, a quantitative analysis of the QCM can be used [1]. We can rewrite the small load approximation below using $Zq = \frac{2m_q}{f_0}$.

$$\Delta f = \frac{i}{2 \pi m_q} Z_L \tag{23}$$

The above version of the small load approximation shows the only parameter that converts the acoustic load to a frequency shift is the is the mass per unit area of the crystal. This same equation can be derived from various other formalisms such as from the frame of a plane-wave. From this equation we can also derive the famous Sauerbrey equation. Now that we have derived the small load approximation we have the tool we need to prove our earlier claims that the change in frequency is proportional to the mass added rather than the thickness. This added mass could be a thin film, but this result equally applies to

tightly adsorbed nanoparticles. The only assumption is that the samples deformation is negligible. As we later discuss, this assumption is not always valid.

The interfacial traction for a perfectly rigid sample is defined as the product of areal mass density and acceleration. This gives us $\sigma_s = -\omega^2 \mu_s m_f$ where μ_s is the amplitude and m_f is the mass per unit area. Using this we find the load impedance below, we then insert this into the small load approximation.

$$Z_L = \frac{-\omega^2 \mu_s mf}{i \omega \mu_s} = i \omega m_f \tag{24}$$

$$\frac{\Delta f}{f_0} \sim \frac{i}{\pi Z_q} i \omega m_f = -\frac{2 n m_f f_0}{Z_q} = -n \frac{m_f}{m_q} \tag{25}$$

Above we have derived the Sauerbrey equation using the small load approximation. The imaginary part in equation 25 is zero. The Sauerbrey equation only works if the layers do not increase the bandwidth. We can rearrange this result in terms of areal mass density m_f to obtain the common equation that describes the mass added per unit area to the QCM. In this form c is commonly referred to as the mass-sensitivity constant that we have described earlier, and now finally derived.

$$m_f = -c \frac{\Delta f}{n} \tag{26}$$

We now turn our attention back to equation 25, where we note the mass-sensitivity constant scales as f_0^{-2}. An improved mass sensitivity constant does not directly translate to an improved noise-equivalent mass. As the frequency increases, so too does the scattering. This scattering on the frequency readings is inversely proportional to the Q. To truly improve the noise-equivalent mass, one must optimize the Qf_0 product. This is shown by inverting the Sauerbrey equation below.

$$m_f = \frac{Z_q}{2}\frac{1}{f_0}\frac{\Delta f}{f} \tag{27}$$

This ties back in to our earlier discussion on the limit of detection. The minimum detectable frequency shift is a fraction of the bandwidth α. This is described in the equation below.

$$\delta(m_f) = \frac{Z_q}{2}\frac{1}{f_0}\frac{\delta(\Delta f)}{f} = \frac{Z_q}{2}\frac{1}{f_0}\frac{\alpha\Gamma}{f} = \frac{\alpha Z_q}{4}\frac{1}{f_0 Q} \tag{28}$$

The above equation indicates a narrow bandwidth allows for a more precise reading of frequency. It further describes the limit of mass detection. It is clear this limit scales as $1/Qf_0$. As a consequence, the limit of detection increases linearly with frequency, not quadratically as the Sauerbrey equation would suggest. Further, in liquids it is even less advantageous to increase the frequency than in air. This is because in liquids the bandwidth increases as $f_0^{3/2}$. This causes the noise-equivalent mass in liquids to scale as $f_0^{-1/2}$ [1].

Equation 28 provides more insight into the selection of a QCM for a given experiment. While higher frequency QCM often boast higher sensitivity on their specifications; when used in liquids, they actually have a worse limit of detection. For use in liquids, a 5 MHz QCM actually has a better limit of detection than a 27 MHz QCM by a factor of 2.3. This consequence arises purely from the bandwidth increase caused by liquids as predicted by the small load approximation. This effect is modeled below for Newtonian liquids.

$$\begin{aligned}\frac{\Delta\tilde{f}}{f_0} &= \frac{i}{\pi Z_q}\tilde{Z}_L = \frac{i}{\pi Z_q}\tilde{Z}_{liq} = \frac{i}{\pi Z_q}\sqrt{i\omega\rho_{liq}\eta_{liq}} \\ &= \frac{-1+i}{\sqrt{2}\pi Z_q}\sqrt{\omega}\sqrt{\rho_{liq}\eta_{liq}}\end{aligned} \tag{29}$$

2.8 Heterogeneous Mass Loading: Viruses & DNA

With the working theory of the QCM now fully described in detail, let us turn our attention towards non-ideal situations. Thus far we have described liquids and solid rigid masses being added to a QCM. However, often samples we are trying to detect, such as cells, DNA, or in our instance thiols, are not perfectly rigid. These samples bind to the surface of the QCM strongly like a solid would, however are not perfectly rigid as they extend into the viscoelastic liquid. These heterogeneous samples do not agree perfectly with the Sauerbrey equation or the simplified circuit models we have thus far presented. Since these samples are not perfectly rigid, they in fact dissipate energy and have a resistive term. This dissipation causes them to fall somewhere in-between a perfectly rigid sample and a liquid.

To investigate this, Johannsmann et. al. studied the dissipation effects of adsorbed nanospheres on QCM in 2009 [49]. In this paper the group attempts to understand the energy dissipation mechanisms that operate in these films as the adsorbed mass is sheared at megahertz frequencies in liquid QCM experiments. To do this they compare FEM and experimental results for globular proteins and viruses with various attachment geometries. They compare the effects of direct attachment, attachment via multiple anchors, and attachment via a single anchor. The group discovered that the dissipation is dependent on the geometry of attachment, but not on the internal properties of these particles. The dissipation is due to small-angle rotation of the adsorbed sphere in the flow field of the fluid, and small-amplitude slippage. The group concludes that the dissipation is primarily determined not by the adsorbate itself, but rather the linking method to the substrate.

Thus far our mathematical models have assumed perfectly rigid structures being added to the QCM that cause no dissipation. Now we will briefly present the models used

by Johannsmann et. at. that allow the dissipation for these semi-rigid films to be determined [49]. These are based on the small load approximation discussed in detail earlier. The QCM dissipation D, is related to the frequency shift f, and the bandwidth Γ seen below. This is essentially equivalent to the resistance of the oscillator R.

$$D = \frac{2}{f}\,\Gamma \tag{30}$$

$$R = \frac{\pi}{16\,A\,f_0^3\,d_{26}^2\,Z_q}\,\Gamma \tag{31}$$

In the resistive term above A is the effective electrode area, d_{26} is the piezoelectric strain coefficient 3.1 pm/V, and Z_q is the acoustic impedance of AT-cut quartz 8.8 x 10^6 kg/m^2s. These parameters are related to the dissipated energy via the relation below.

$$\Delta D = \Delta Q^{-1} = \frac{\dot{E}}{\omega\,E} \tag{32}$$

In the above equation Q is the quality of resonance we discussed earlier, $\dot{E}$ is the rate of energy dissipation in the sample, and E is the total energy contained in the resonators motion. This last relation makes it clear that quantitative interpretation of QCM data requires some knowledge of the mechanism by which the energy in an adsorbed layer is dissipated.

When the thin film is much smaller than the penetration depth of the QCM, energy lost due to the film can be parameterized in terms of the frequency-dependent elastic compliance J' . For a thin film in liquid, the ratio of the change in dissipation and frequency, called the Df ratio is seen below, where η_L is the viscosity of the liquid.

$$\frac{\Delta\Gamma}{-\Delta f} = \omega\,J'\eta_L \tag{33}$$

The energy dissipated from these heterogeneous films could originate from two possibilities. The first is the energy is dissipated inside the adsorbed film. This would cause

dissipation to be linked to the particles elastic compliance. However, by applying the continuum approach, this possibility proves inadequate [50–52]. Instead, Johannsmann et. al. argues the dissipation arises from the contact zone between the oscillator and the adsorbed heterogeneous film [49]. The group finds that more than 90% of the energy is dissipated in the liquid. Thus dissipation measurements provide information about the linkage between particles and their surface, rather than the particles themselves. These dissipation and frequency shifts can be calculated from an extension of the small load approximation seen below. Here Δf^* is the complex frequency shift, Z_L is the load impedance, $< \sigma >$ is the laterally averaged tangential stress, and $\dot{\mu}$ is the lateral speed at the crystal surface.

$$\frac{\Delta f^*}{f_0} = \frac{i\, Z_L}{\pi\, Z_q} = \frac{i}{\pi\, Z_q} \frac{< \sigma >}{\dot{\mu}} \tag{34}$$

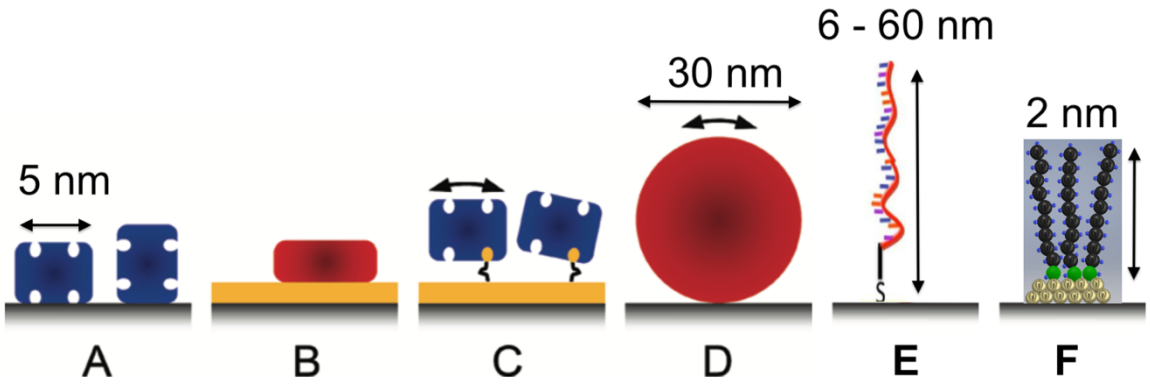

Figure 18: Various binding/adsorption geometries are displayed above along with typical sizes. In panels A and B the adsorbates bind to the substrate over an extended area, this is typical with avidin or streptavidin to gold. In panel B a lipid support layer is used seen in yellow. In panel C the adsorbates are attached via a flexible linker molecule such as with streptavidin bound to a biotinylated support lipid bilayer. In panel D we see adsorbates bound to the surface over a limited contact area such as is common with the cowpea mosaic virus. In panel E we display thiolated DNA that have typical size of 6-60nm. In panel F we displayed the 1-octadecanethiol used in our experiments. Adsorbates in panels C, D, and E have more freedom to move causing greater dissipation compared to panels A and B [49]. In this study we will determine how thiol compares to these other adsorbates.

Adsorbates like avidin or streptavidin seen in panels A and B in the figure above produce very little dissipation, so little, it is close to the limit of detection for the QCM. These adsorbates act as nearly ideal perfectly rigid masses, and obey the ideal models presented previously. Therefore, these globular proteins are too intrinsically rigid to induce appreciable dissipation of energy at megahertz frequencies. The flexible linker molecule displayed in panel C is roughly 1 nm in length, and greatly increases the dissipation for these same adsorbates. This causes them to no-longer be ideal rigid masses, and they now produce detectable dissipation. When a flexible linker is added, the rotation of the protein causes dissipation in the liquid. For larger adsorbates with a limited contact area like that found in panel D with cowpea mosaic virus, Johannsmann et. al. performed FEM calculations to test the effect of perfectly rigid samples on a soft spacer layer, along with a rigid substrate with a compliant particle. The results of this FEM calculation are displayed below.

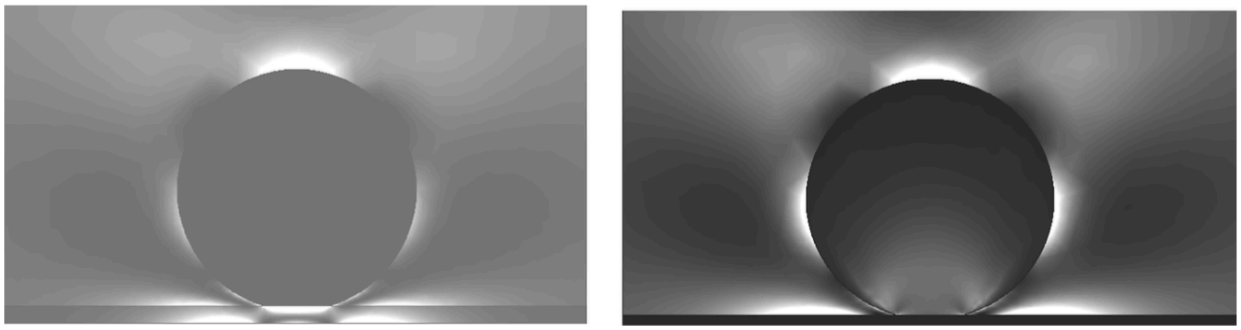

Figure 19: The spatial distribution of dissipated energy in a model of the 30 nm diameter cowpea mosaic virus is displayed above. White areas have higher rates of energy dissipation. In the left image the virus is assumed to be perfectly rigid bound to a soft spacer layer. In this simulation the majority of the energy is dissipated in the soft adhesion layer where the rigid mass is bound. The rest of the energy is dissipated in the liquid as it flows around the virus. Alternatively, the right image shows a rigid substrate with a slightly deformable virus. In this instance no energy is dissipated by the solid and rigid substrate. Rather the energy is primary dissipated in the liquid surrounding the virus, with some energy being dissipated by the virus itself [49].

The results above demonstrate that a perfectly rigid adsorbate does not exhibit any dissipation. We instead see this dissipation in the surrounding liquid, and in the softer substrate. However, when we have a solid substrate, we see no dissipation in the planner layer and instead see dissipation only in the softer adsorbate and surrounding liquid. Both of these results reproduce experimental observations equally well. Where the energy is dissipated is dependent on the specific substrate, adsorbate, and binding method. All of these results demonstrate that the specific elastic properties of small particles play little effect on dissipation, but rather how they bind to the surface makes a large difference. That is to say, more energy is dissipated in liquid flowing around particles that can move than in liquid flowing around stationary objects [49]. These models are valid for small nano-sized particles that are not perfectly rigid. However, these results are strikingly different from that of elongated films such as with DNA.

In the past decade many QCM experiments using DNA films have been explored. We present some relevant results by Papadakis and Gizeli et. al [53,54]. This group studied the dissipation of QCM when binding to various lengths and geometries of DNA. The lengths of these DNA strands ranged from 6nm to 60nm. They found the QCM was capable of characterizing multiple double stranded DNA of various lengths. It was determined that the QCM energy dissipation per unit mass observed when binding to DNA is directly related to its intrinsic viscosity. This is an interesting new effect; as all previous models we have presented have shown that the solid adsorbates have no viscosity. Previously the density of the solid causes a frequency shift, and with viruses, we see a small dissipation term that is independent of elastic properties. With DNA however, due to their length, binding geometry, and binding method, a viscosity term can be found. This viscosity provides

quantitative information on the size and shape of the adsorbed molecule. This was verified by demonstrating double and triple helix DNA could be distinguished based on dissipation. The group further could discriminate between different bending positions along the chain.

In two more separate studies of DNA assembly and hybridization it was found as the surface coverage on the QCM increased, so too does the dissipation or apparent viscosity of the film [55,56]. These studies suggest that the large DNA strands are entrapping additional water, further increasing resistance and thus dissipation. All of these studies are suggesting DNA falls somewhere between a solid and liquid when being adsorbed onto a QCM. It acts not as a perfectly rigid ideal mass, but rather a viscoelastic material, that carries with it additional liquid. The groups conclude that since the DNA carries with it additional water, the total mass of just DNA is not simple to extract. However, the complexity of mass measurements does not impair the qualitative evaluation of the QCM on kinetics. In addition, the QCM is able to provide valuable insight into the structure of the film, viscoelastic properties, and changes to the geometry upon hybridization [56].

From the above examples we have described a variety of the non-ideal semi-rigid films often used in QCM experiments. Tightly bound adsorbates with multiple anchor points like the 5nm streptavidin show dissipation that is barely detectable and can be modeled well as a solid mass. Larger adsorbates like the 30nm cowpea mosaic virus show some dissipation. This example demonstrates that the specific elastic properties have little effect on the dissipation, and instead provide information on the binding of the adsorbate to the surface. Finally, with 6-60 nm DNA we see the film has its own viscosity, and acts as something between a solid and a liquid. The DNA traps additional liquid that it carries with it, acting as a viscoelastic material. With these various models now presented we turn our

attention back to 1-octadecanethiol, the primary adsorbate used in our research.

2.9 Thiol Mass Loading

Since 1-octadecanethiol has a length of 2nm it is much smaller than DNA or the cowpea mosaic virus. Unlike the 5nm streptavidin however, it only has one anchor point to the gold sensing surface, yet is nonetheless smaller. From these other examples we expect our thiol to have a slight dissipation. The single anchor point and chain of CH_2will increase dissipation like DNA, but its small size will trap and carry very little additional liquid. A demonstration of the minor dissipation caused by 1-octadecanethiol on a flat QCM is displayed in the figures below.

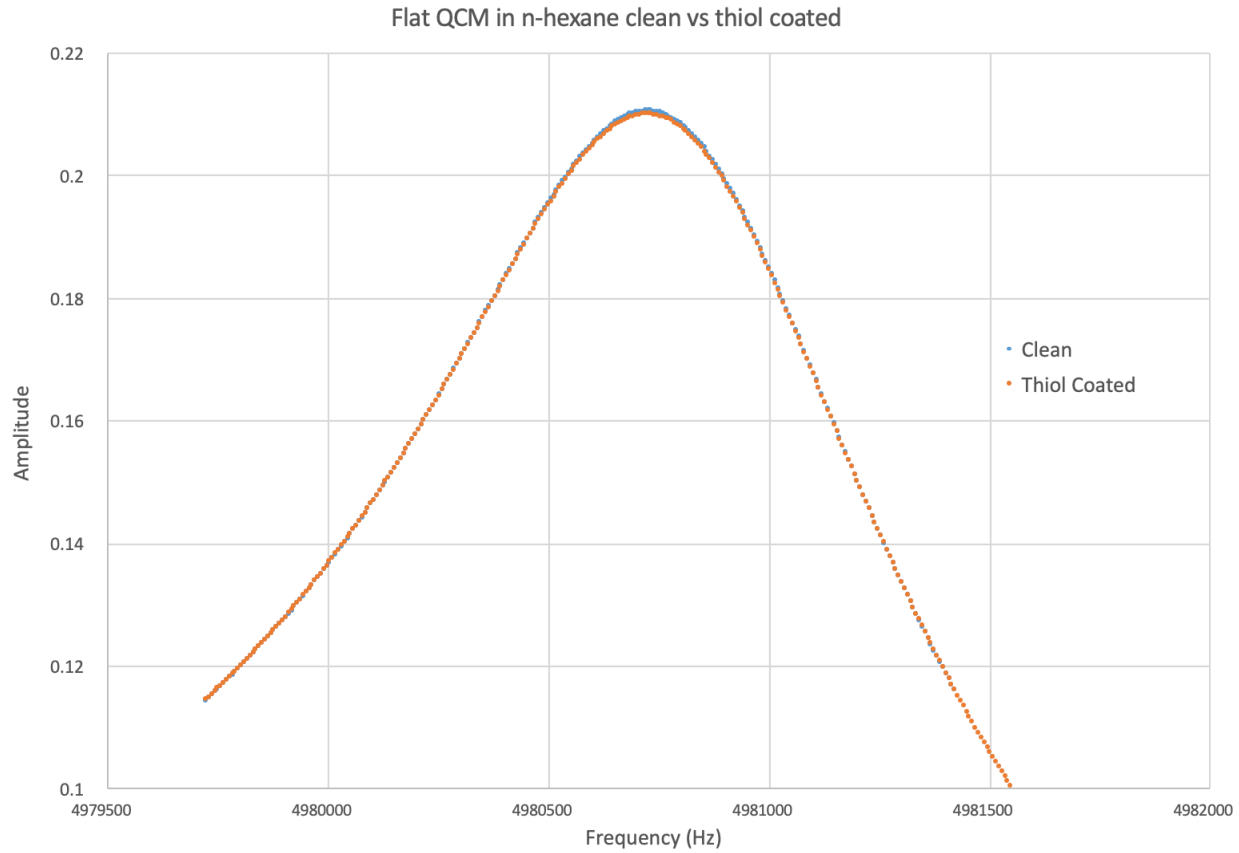

Figure 20: Amplitude plot of a flat QCM resonance in liquid n-hexane is displayed above. We display the amplitude of a clean QCM vs the thiol coated resonance. From this figure it is clear the thiol produces a very slight dissipation.

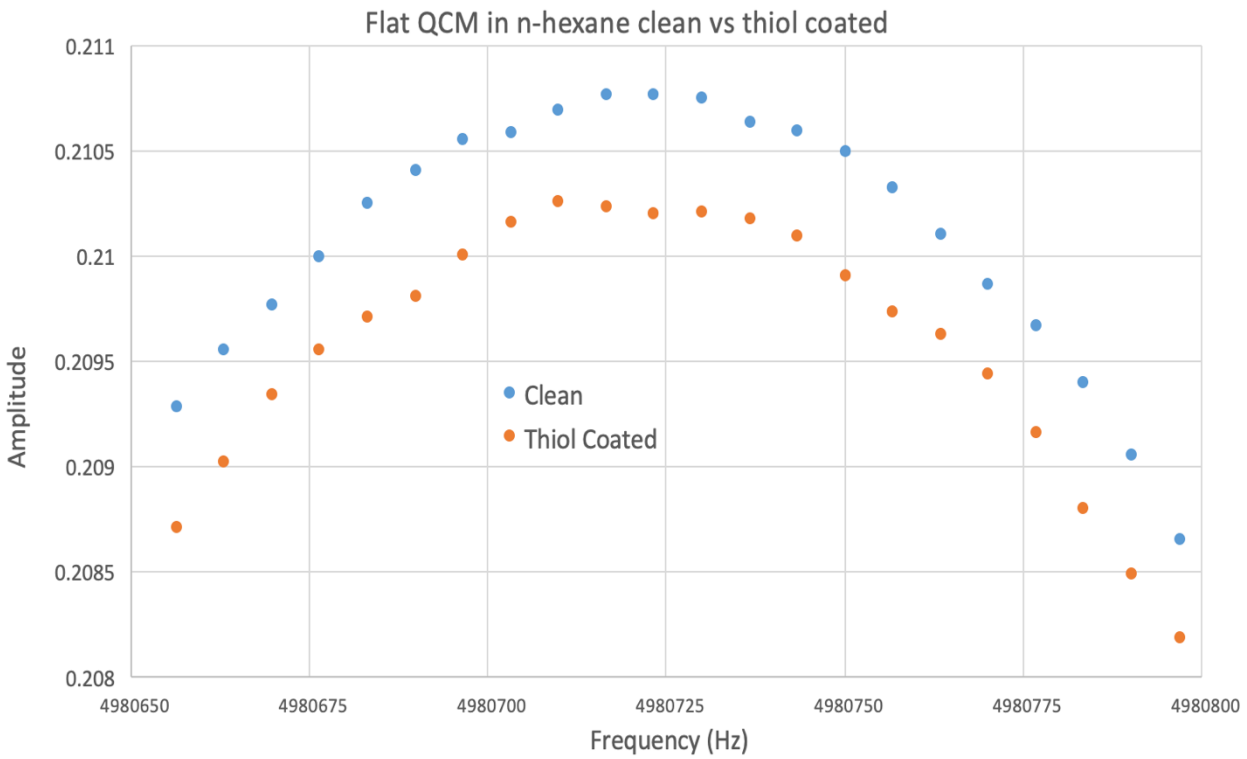

Figure 21: A closer look at the dissipation for 1-octadecanethiol on a flat QCM in liquid is displayed above. The plot shows the thiol increases dissipation by 0.00057, or a 0.27% decrease in amplitude from a clean state to a monolayer coating. The span of the above plot is 150 Hz, and the amplitude is the measured signal divided by the input.

The minor dissipation caused by thiol is often inconsequential to most QCM experiments and measurements. However, in our porous QCM, when we are adding hundreds or even 1000 times more thiol than a flat QCM, this dissipation may be of consequence. If the dissipation caused by adding thiol is a linear effect, for a 100 times more sensitive substrate we would expect a change in dissipation of 0.06. For a 1000 times more sensitive substrate if we assume a linear model for dissipation the sample would no longer oscillate in liquid. The slight dissipation caused by thiol for thicker porous gold substrates actually produces a limit to the maximum possible sensitivity increase. Below we use the circuit models of our QCM to quantify the resistance induced on the QCM due to the addition of thiol.

Now that we have fully modeled the QCM for solids, liquids, and non-ideal masses we wish to determine the resistive term for our not perfectly rigid thiols. To do this we rely on our aforementioned models and equivalent circuit. We use Mathematica to fit our experimental amplitude plot using a nonlinear model fit based off our governing equation. The fit treats the QCM circuit as a modified RLC oscillator. The Mathematica fit outputs estimated values for the resonant frequency, total inductance, total resistance, and total capacitance. By comparing a clean QCM and coated QCM we can determine the change in resistance caused by our thiol. The fit of our Mathematica model to our QCM amplitude plot is displayed below.

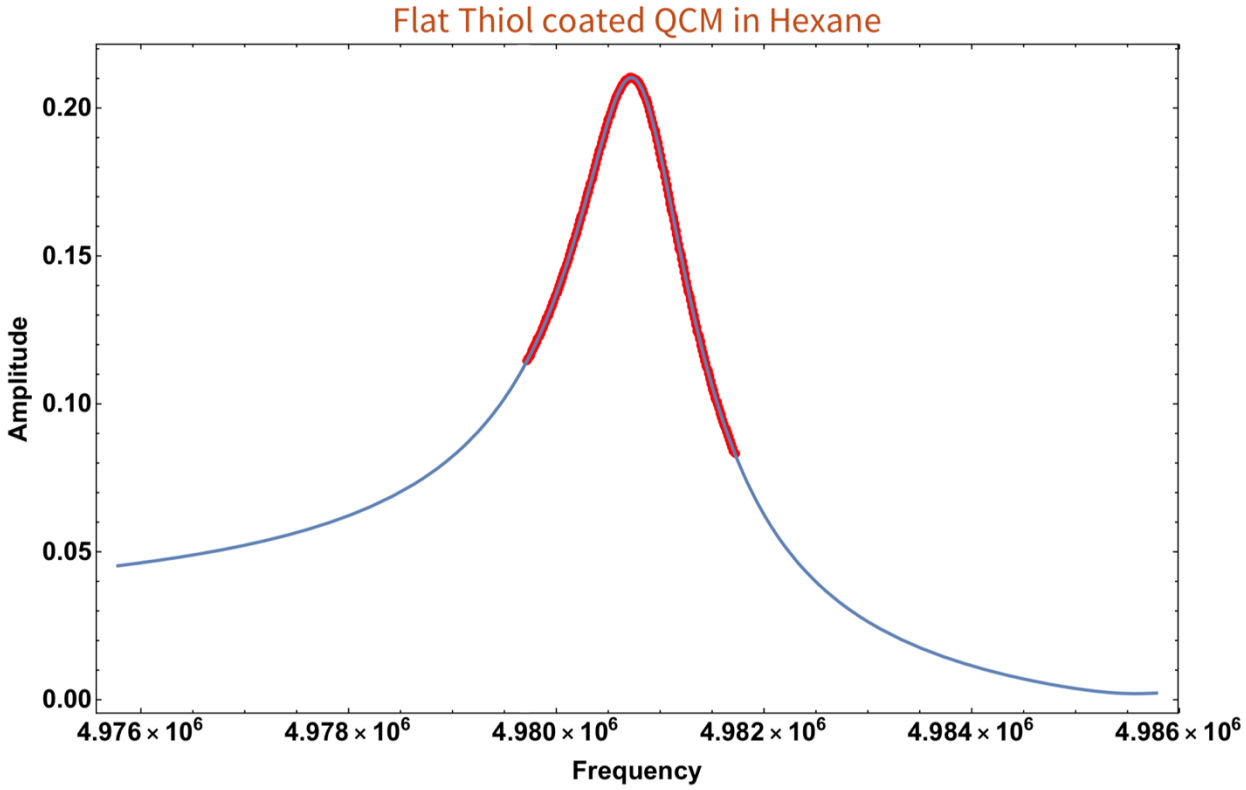

Figure 22: Using our aforementioned models we fit the QCM data in Mathematica to determine the values for the resistive term for both clean flat QCM and thiol coated QCM in liquid n-hexane. The model plotted in blue fits the raw data from the QCM shown in red seen above.

The Mathematica fit above estimates the total resistance of our QCM oscillating in the liquid environment. This resistive term sums all the resistance in the circuit coming from the intrinsic resistance to the system and QCM, the resistance of the liquid, and the resistance of the coating. Nonetheless by subtracting a baseline resistance to a thiol-coated resistance we can determine the resistance on a flat QCM caused by 1-octadecanethiol. The fit estimates a resistance for the entire system to be 189 Ω . The change in resistance due to a thiol coating on a flat QCM in liquid n-hexane is 0.58 Ω. The change in resistance due to the thiol coating is then 0.31%. This result is similar to our estimate based on the change in amplitude of 0.27%.

An example of the additional dissipation of thiol on a porous QCM is displayed in the figure below. The 1 μm porous QCM below adsorbed 66 times more thiol than a flat QCM. The change in amplitude due to the thiol coating was 53 times more than a flat QCM produces. We detail the results of dissipation in porous QCM of various thicknesses in the experimental section. We use the same method displayed above to determine the limitation dissipation creates on the possible sensitivity increase of surface modified QCM. The extra sensitivity of the porous sensors we fabricate definitively demonstrate the dissipation caused by these small 2 nm thiol monolayers.

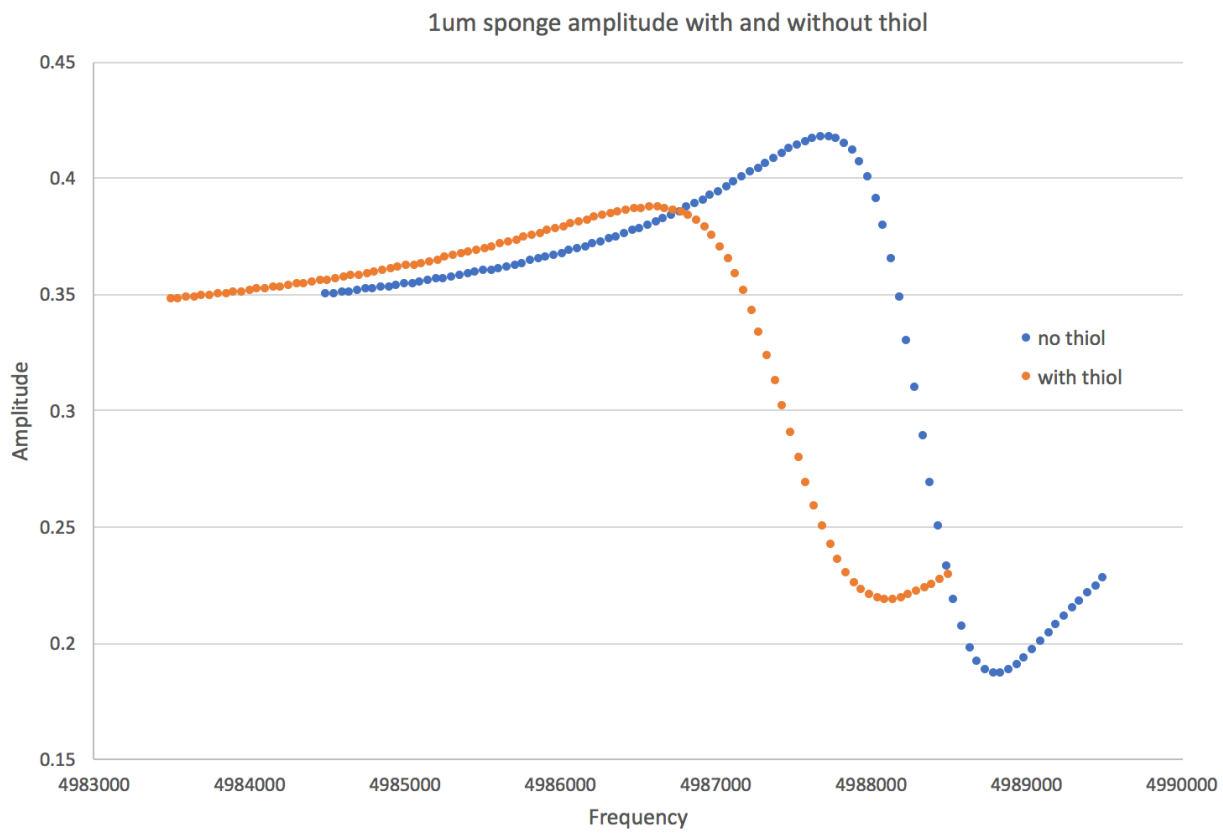

Figure 23: The amplitude of a porous QCM in liquid n-hexane can be seen above. While theory suggests mass loading has no dissipation, we still see a resistance from the addition of thiol to the QCM, and thus see a slight decrease in amplitude. This resistance is observed because the thiol is not perfectly rigid. The thiol is also dragging additional liquid, increasing the dissipation of the sensor.

2.10 Porous Substrates: Working Principle

From the above mathematical models and equivalent circuits, we have seen that a viscoelastic material such as a liquid has a resistance. This resistance causes the amplitude of oscillation to decrease to the penetration depth seen in equation 10. A typical decay length in a liquid such as water is found to be ~250 nm [46,57]. However, solid mass loading added to the surface of the QCM has no resistive term, and thus changes the frequency without decreasing the amplitude. This principle is what allows a QCM to measure mass added to the surface so precisely, and explains why it works so well for

measuring depositions from sputtering or evaporation. The mass added to a QCM from these two deposition techniques is a solid and rigid film. Thus the amplitude of oscillation propagates through these materials without decreasing the amplitude as demonstrated below [57].

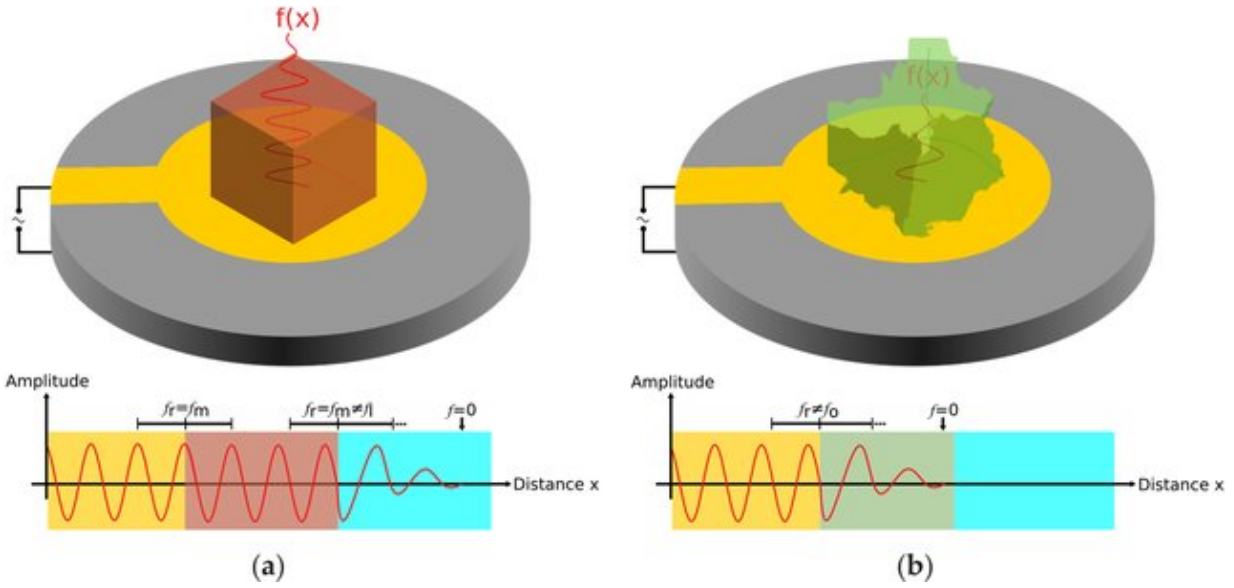

Figure 24: The amplitude of a QCM propagates without deterioration through a solid deposited mass as seen in (a) above. This rigid mass oscillates with the same amplitude and does not decay until the wave leaves the solid surface. The yellow color represents the gold coating on the QCM, the red represents a solid mass such as copper, and the blue represents a liquid. However, in (b) we see the coating material is viscoelastic represented in green. This material cannot follow the vibrational acceleration causing energy to be dissipated, and thus decreases the amplitude of the signal [57].

Since QCM see little to no deterioration of amplitude through solid films such as metals, it allows novel structures to be added to the surface to increase the area. Increasing the surface area in the x-y plane has no effect on the sensitivity of a QCM. A 1mm QCM sensing surface, or a 1cm QCM sensing surface both have the same sensitivity, and would both have the same frequency shift due to a monolayer being added. This is because the QCM frequency shift is in terms of mass per unit area. However, by increasing the surface area z-direction, by adding a porous structure, the surface area can be

increased while also increasing the sensitivity [5–9,38]. The principle that a solid and rigid mass added to a QCM has no deterioration of the amplitude, is what has allowed us to increase the sensitivity of our flat QCM by more than three orders of magnitude.

Our theoretical focus thus far has been dominated by the working principles and models for flat QCM and the effects adsorbates have on them. Now that we have introduced the effect of thiols on our porous structure, let us turn our attention to the properties of porous structures and the work done with them thus far. In the past 15 years interest has grown in porous gold films due to their unique properties of electrical conductivity, chemical stability, and high specific surface area [58–67]. Porous gold has been used in diverse fields from liquid wetting, chemical detection, Raman sensors, and study of chemical kinetics [6–8,37,38,68–71]. The use of porous gold as an electrochemical glucose sensor is another growing field due to its high sensitivity and large surface area [72–76].

Various methods have been used to fabricate these porous structures such as self-assembly, electrochemical, de-alloying, and templating. Each of these fabrication techniques produces a structure with slightly different properties[6–8,37,38,68,71,76–94]. The specific surface area of porous gold depends largely on pore size that ranges from 5-100 nm [71]. This causes the specific surface area to range from 1.5 – 12 $\frac{\mathrm{m}^2}{\mathrm{g}}$. Each of these fabrication techniques, various atomic percentages of gold, and various thicknesses produce porous structures with differing optical properties [91–94].

2.11 Porous Gold: Optical Properties

The optical properties of porous gold is a field of study in its own right. Maroof et. al. examined the optical properties of porous gold using ellipsometry and spectrophotometry [94]. In this study they determined such films show unique dispersion in their optical

response across all NIR wavelengths. The refractive index displayed non-metallic characteristics, while the extinction coefficient showed metallic properties. It was later discovered that the properties of gold films are dependent on occupancies of voids. In another study, Dixon et. al demonstrated the optical properties are dependent on the thickness of the structure [93]. Where thick films have novel properties and thin films act much like bulk material.

In our work we have noticed macroscopic optical properties of the porous gold can give indication of the porosity of the structure. We find brown-red porous structures have a smaller surface area than black porous structures based on thiol adsorption. We further notice thicker porous gold substrates gain a more matte look, while thinner samples are more reflective to white light. We also observe a dependence on the atomic ratio of gold on the color. The brown substrates tend to have 34 - 39 atomic percent gold, whereas the samples from 27 - 33 atomic percent gold appear more black. In lower concentrations of gold, we often get a variety of colors seen in the bottom left of the figure below where a rainbow of red, orange, yellow, and green are seen before the sample appears black at the edges. Porous gold with too little gold often delaminate from the solid gold substrate due to having too much silver in the alloy. Whereas samples with too much gold cannot be fully etched to remove all the silver.

The optical properties of porous gold and even gold nanoparticles are their own field of study and not the focus of this work. However, these properties can provide insight into the fabrication process of our porous structures. Even adding thiol to the porous gold we use can produce optical changes to the structure visible with the naked eye. These thiol coatings can produce a white-grey matte finish on the porous gold until it is removed. This

observation is actually used in optical studies of gold nanoparticles for detection of proteins and thiols [95–97]. The figure below displays some of the optical properties of our porous gold that we have observed through our studies.

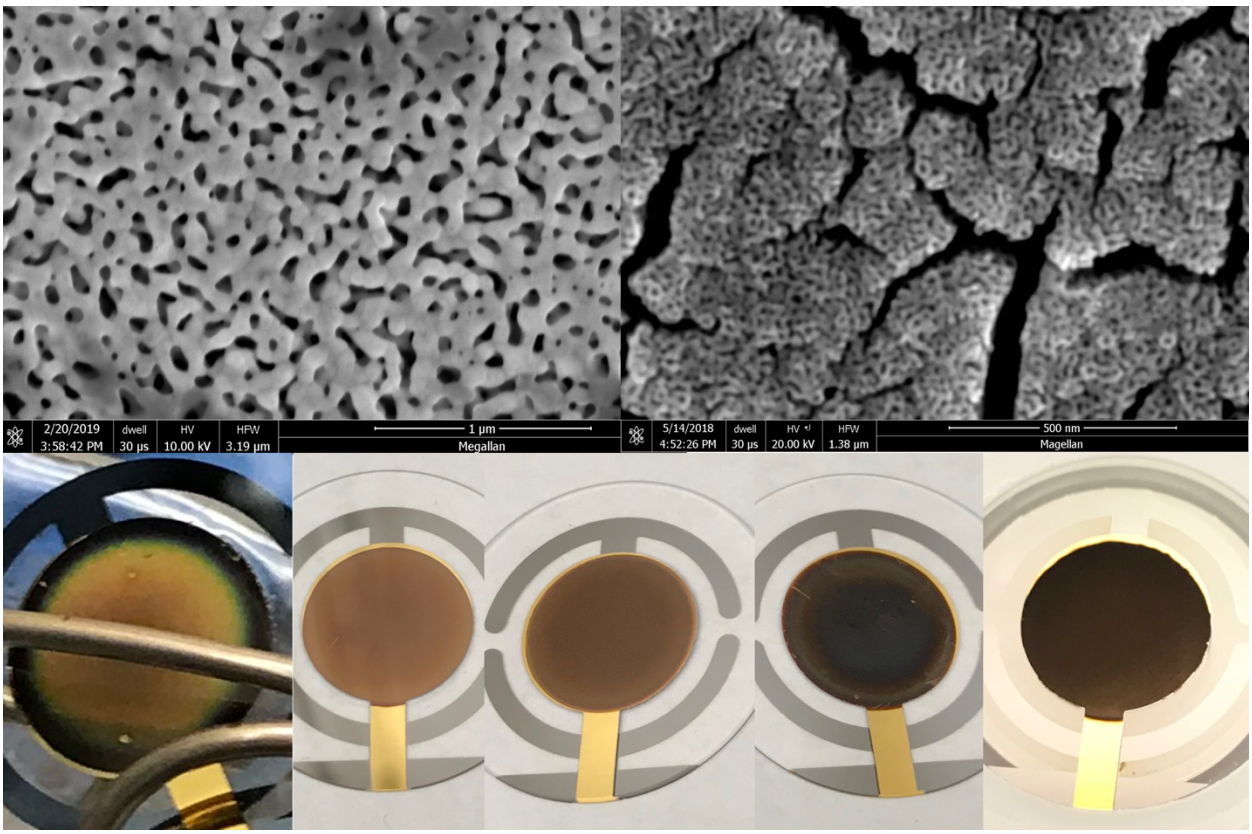

Figure 25: SEM and macroscopic optical properties of various porous gold structures are displayed above. The SEM image on the top left shows what a typical substrate looks like that is brown-red in color. We note this sample is porous, but lacks the small 10nm pores observed on the SEM image on the top right. The SEM image on the right is typical of porous gold that macroscopically appears black. The black porous gold has a higher specific surface area due to these small nanopores. They further demonstrate increased thiol adsorption. The porous gold on the bottom left image was produced with only 25 atomic percent gold, this substrate showed a variety of colors from red to black at the edges. We then display an array of porous gold ranging from brown-red with a higher concentration of gold (34-39 atomic percent), to the ideal black color observed with a ratio near 30 atomic percent gold.

2.12 Porous Gold: Theory Correction

The electromechanical properties of a porous gold QCM work similar to a flat QCM that we have described earlier. The additional mass due to the porous surface adds an inductance term, lowering the base resonant frequency of the oscillator. This inductance term plays little effect on the amplitude of oscillation and simply acts by shifting the frequency downwards. The additional gold is not perfectly rigid and also adds a small resistive term, similar to what was demonstrated above with thiol. Lastly the modified surface changes the intrinsic base capacitance of the oscillator.

The porous gold surface modification adds three simple corrections to the model we have presented above. This is also described by Yu et. al. who used a porous gold QCM to detect proteins in 2005 [63]. When taking QCM measurements the output provides the total values for resistance, capacitance, and inductance. It is only though the experimental process that individual terms such as the resistance due to liquid can be determined. We display these corrections below where PG refers to porous gold. This is by no means a comprehensive breakdown of all the individual contributions to the resistive or inductive terms, but rather a simplification to categorize many small effects. For example, the effects of surface stress and energy dissipations due to non-shear couplings are included in the broader terms for the intrinsic resistance and inductance of the QCM.

$$R_{total} = R_{QCM} + R_{PG} + R_{liquid} + R_{solid} \tag{35}$$

$$\frac{1}{C_{total}} = \frac{1}{C_{QCM}} + \frac{1}{C_{PG}} \tag{36}$$

$$L_{total} = L_{QCM} + L_{PG} + L_{liquid} + L_{solid} \tag{37}$$

Porous gold oscillating on a QCM surface causes interesting effects on the liquid inside it. While on a flat QCM the liquid is sheared and the oscillatory wave penetrates to a specified depth, on a porous structure this becomes more complicated. Devices with textured surfaces, either patterned or completely random, literally trap fluid inside them. This trapped liquid is forced to move synchronously with the oscillating crystal surface rather than undergoing a progressive phase lag as occurs with a viscously coupled liquid [53,98]. This causes the liquid to behave like an ideal mass layer contributing almost no change to the dissipated energy.

We observe this effect to be true with our experimental measurements. Instead of seeing the effects of thousands of layers of viscously coupled fluid dragging, massively damping the oscillator, we instead see little change in the dissipated energy of porous media in liquid. While the porous media does drag more fluid than a flat QCM, this additional fluid acts similar to an ideal mass layer. We verify that liquid trapped in our porous structure acts much like a solid due to the small pore size and large penetration depth in the next chapter.

2.13 Thiol Adsorption: The Langmuir Isotherm Model

With the physics now thoroughly described we move on to the chemistry of the experiment. Thiols used on metal surfaces are used for a variety of applications. As a detection tool, thiols can be modified to add specificity to QCM experiments for detection of specific proteins, cells, or molecules. They also can be used to control the properties of metallic interfaces. A self-assembled monolayer of thiol offers straightforward regulation of surface wetting properties, and have been used for corrosion protection. We demonstrate these wetting properties in the next chapter. Further, thiols have applications for

lithographic patterning and to build photoresponsive structures.

As we mentioned earlier, thiol binds strongly to the surface of gold, however this binding requires a chemical reaction. The adsorption reaction of thiol to gold is described by the reaction below.

$$\mathrm{Au(s)} + \mathrm{RS-H(solv.)} \leftrightharpoons \mathrm{RS-Au(s)} + \frac{1}{2}\mathrm{H_2(solv)} \quad (38)$$

The reaction takes place at the gold surface where the thiol reacts with the gold to form a gold thiolate monolayer (Au-SR) and hydrogen. The hydrogen is believed to disassociate and propagate into the solvent. The evidence for this comes from the lack of a S-H bond observed in Raman scattering studies performed after thiol is adsorbed to gold surfaces. The reaction is reversible, and thus there is both a chance for a thiol to adsorb or desorb from the surface. Hydrogen does not seem to play much of a role in the process of desorption, as desorption experiments performed under atmosphere and 1 atm of hydrogen both produce the same desorption rate. The thiol however is much more energetically favored to bind to the surface than to desorb. This causes a monolayer to quickly be formed over the gold surface [31].

The adsorption of thiol does not happen instantaneously, but rather takes some finite time that is substantially slower than, but dependent on the aliquot mixing time. The kinetic response of this reaction can be modeled using a modified Langmuir isotherm. This model is based on the assumption that adsorption is limited to one monolayer. It further assumes all surface sites are equivalent and that adsorption to one site is independent of the occupancy condition of adjacent sites [31]. This model has been shown to work exceedingly well for flat QCM by Blanchard, Noort, and Jiang among many others [31,37,99]. While the specific assumption that all surface sites are equivalent does not

necessarily hold true for porous gold, the model nonetheless can be applied with success. There is also debate in the field on the assumption of no interaction between thiols on the basis of physical and chemical interaction. While the thiol chains likely interact with each other, the timescale of these interactions is much larger than the adsorption rate modeled by the Langmuir model due to the short range nature of dispersive forces.

The Langmuir isotherm model nonetheless provides a useful tool to model the kinetics of adsorption of thiols on gold surfaces. The binding rate is dependent on concentration, the number of binding sites, and the affinity constant. The bound mass is described below as m, where m_{max} is the maximum mass uptake ($dm/dt = 0$), t_0 is the time at which adsorption starts, and k_a is the adsorption constant.

$$m = m_{max}(1 - e^{-k_a (t-t_0)}) \tag{39}$$

The adsorption constant itself is dependent on the association rate k_{as}, the bulk concentration [A], and the disassociation constant k_d seen below.

$$k_a = k_{as}[A] - k_d \tag{40}$$

The affinity constant for disassociation k_D is defined below [37].

$$k_D = \frac{k_d}{k_{as}} \tag{41}$$

Equation 39 above is frequently used to fit experimental QCM adsorption data to the Langmuir isotherm model. From the fit of experimental data with this model the adsorption constant can be determined. This constant is based on concentration, stir speed, geometry of the experiment, and porosity as will be discussed in the following chapter.

2.14 Thiol Desorption & Self-Exchange

While many studies are often focused on the adsorption kinetics [31,44,50,51,96,99,100], other studies focus on desorption [6,38,42]. In the Taborek et. al. publications previously discussed, desorption of liquid helium on porous substrates provided insight into capillary condensation. Studies on thiol desorption provide insight into the stability and self-exchange in thiol the monolayer [42]. Schlenoff et. al. performed a study using radiolabeled thiols to determine coverage, thermal stability, and photostability of octadecanethiol immersed in solution. In this study a monolayer of the radiolabeled thiol was bound to various metal surfaces. The monolayer coated metal was then placed in solutions with no thiol (pure solvents), or solutions with normal thiol that was not radiolabeled. After various periods of time ranging from hours to six days, the metal samples were examined to determine the desorption and stability of the radiolabeled thiol.

Schlenoff et. al. determined the coverage of octadecanethiol on gold surfaces was independent of concentration. They found a surface coverage was 330 $\frac{\text{ng}}{cm2}$ for octadecanethiol on gold and was dependent on surface roughness. No evidence of a thiol multilayer was observed for gold; however, copper did support 10-30 multilayers. Spontaneous desorption of thiol from the gold surface was observed for all pure solvents used, with each solvent having a differing quantity of desorption. They show the quasi-steady-state limiting coverages reached after long immersion times are a function of substrate and solvent seen below [42].

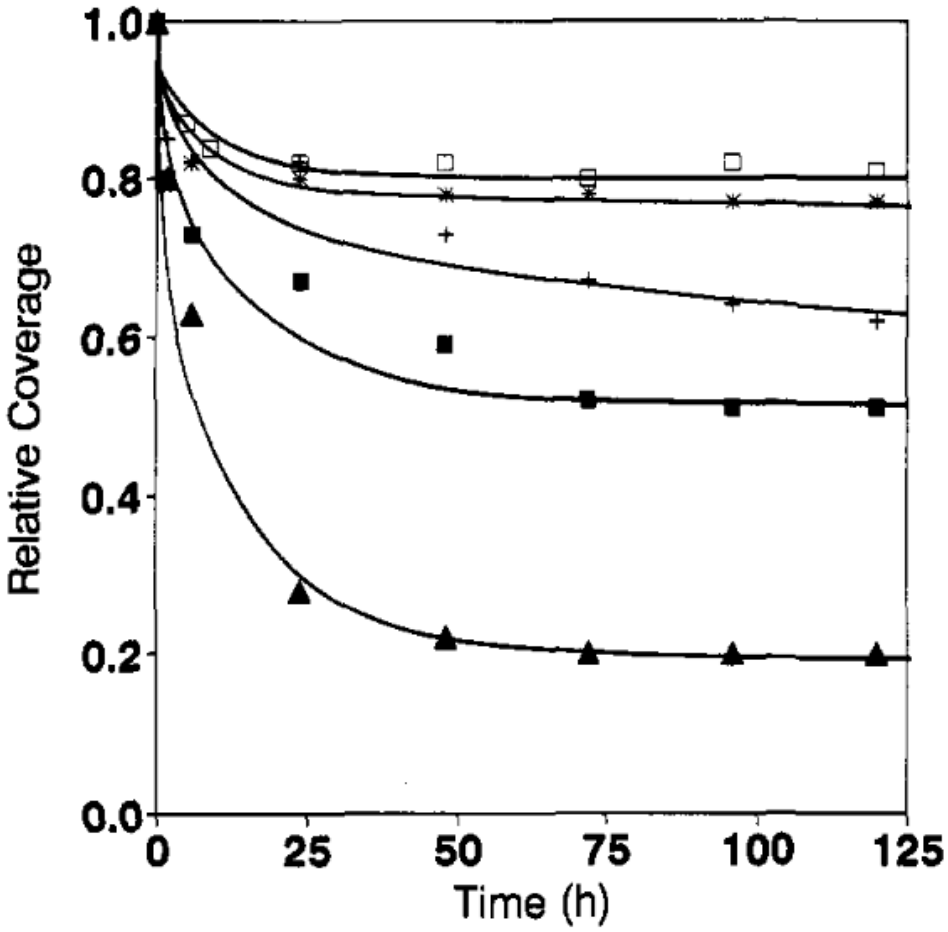

Figure 26: After a monolayer of radiolabeled octadecanethiol is adsorbed to a gold surface, it is then placed in a pure solvent to monitor desorption. It is clear in all the solvents an equilibrium is eventually reached. The solvents used were 0.1M aqueous $HClO_4$ (□), water (*), hexane (+), ethanol (■), and THF (▲) [42].

From the above figure we see that the thiol-gold bond is indeed a two-way reaction. Once a thiol is added to the gold surface, some of it can be removed by desorption when placed in a pure solvent. This process is similar to the kinetics of self-exchange of thiol. To demonstrate self-exchange, the group placed radiolabeled thiol on the gold surface. They then immersed the sample in a solution of normal, non-radiolabeled thiol and observed the change in the quantity of radiolabeled thiol remaining on the surface over various time

periods. The results displayed below demonstrate the self-exchange rate is slightly dependent on the concentration of thiol in the solution.

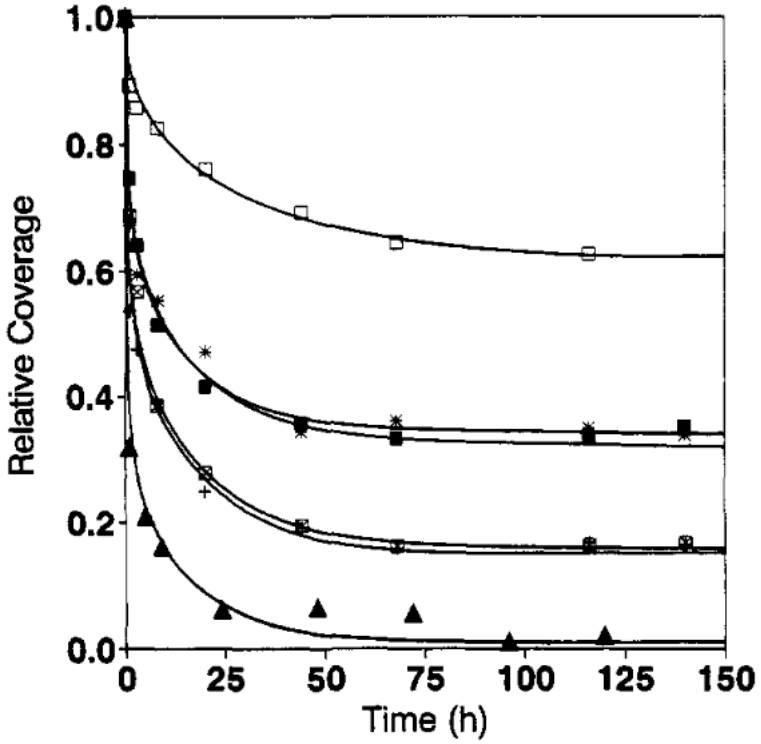

Figure 27: Self-exchange of octadecanethiol on gold in solutions of various concentrations are displayed. A radiolabeled thiol is placed onto the gold surface before immersion in solution with normal, non-labeled thiol, the remainder of radio-labeled thiol on the surface vs time indicates self-exchange. The solutions used are pure hexane (□), 1mM thiol in hexane (■), 10mM thiol in hexane (*), 100mM in hexane (+), saturated 500mM thiol in hexane (☒), and pure thiol (▲)[42].

2.15 Thiol Diffusion vs Langmuir Model

The desorption and self-exchange of thiol is part of a mechanism for attaining equilibrium adsorption coverage to maximize packing density. Reaching equilibrium for these extended thiol chains often requires additional time. Typically, when thiol binds to a surface it first rapidly forms a non-ordered layer. Over time through the self-exchange and the desorption process this monolayer is reorganized into an ordered film that maximizes packing density. While many groups argue the adsorption of thiol follow a Langmuir

isotherm model, Schlenoff et. al. argues that after re-evaluation of desorption and self-exchange data, a diffusion controlled adsorption is more apt. The model for diffusion controlled adsorption is displayed below, where D_{RSH} is the diffusion coefficient, and C_{RSH} is the concentration. To fit Blanchard's experimental results typical values of $D_{RSH} = 10^{-6}\ \frac{cm^2}{s}$ and $C_{RSH} = \ 3 \times 10^{-7}\ \frac{mol}{cm^3}$ provide a result of $5 \times 10^{-10}\ \frac{mol}{cm^2}$ in 2 seconds.

$$\text{number of mol./area} = \frac{2\, D_{RSH}^{1/2}\, C_{RSH}\, t^{1/2}}{\pi^{1/2}} \tag{42}$$

Our results indicate that the Langmuir model fits adsorption data for porous QCM much better than the proposed diffusion model displayed above. We note the Langmuir model fits well over the entire adsorption process, whereas the proposed diffusion model only works for specific intermediate time periods. The diffusion model fits poorly for the beginning of adsorption, this may however be due to mixing effects. Obviously the diffusion model also does not taper off to an equilibrium as shown in the Langmuir model. For the intermediate period where the diffusion model may be correct, we still see a better fit with the Langmuir model. Due to these factors we will stick with the Langmuir isotherm model to describe our kinetics in the next chapter and detail our results further. For now, we simply present a comparison of the diffusion model and Langmuir model to thiol adsorption on our porous substrates seen in the figures below.

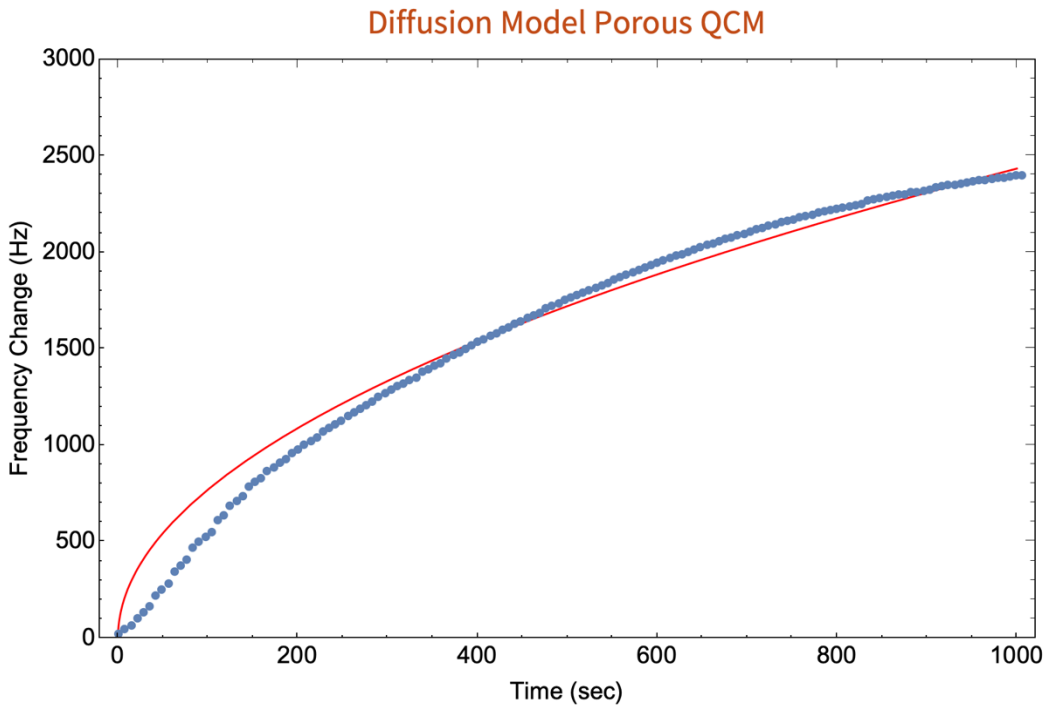

Figure 28: The diffusion model (eq. 42) proposed by Schlenoff et. al. is displayed above in red, and fit to adsorption data for 1-octadecanethiol onto our porous QCM. The lag of experimental data to the model in the short term time frame may be due to mixing effects. After 1000 seconds when the QCM adsorption tapers off, the model obviously diverges.

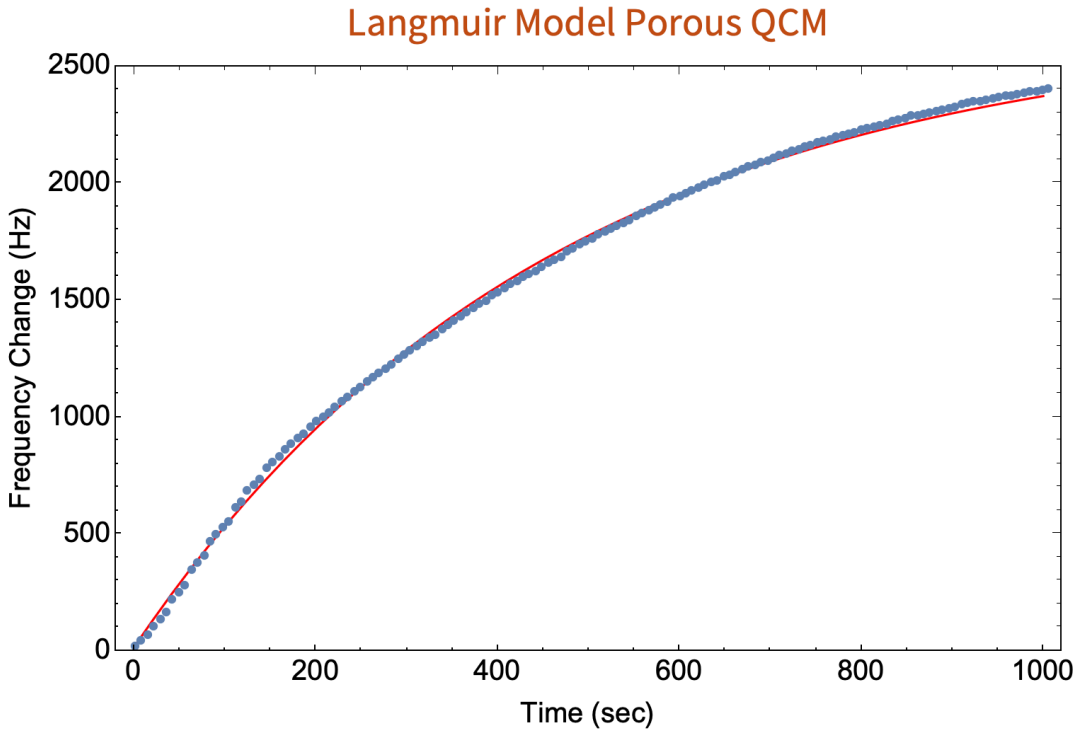

Figure 29: The Langmuir isotherm model (eq. 39) proposed by Blanchard among others is displayed above in red, and fit to adsorption data for our porous QCM in blue. This model fits the data exceedingly well.

2.16 Defect Sites & Conclusion

The exact mechanism of thiol desorption and self-exchange is still debated. Since self-exchange shows little dependence on concentration a bimolecular mechanism is unlikely. The bests models currently suggest exchange occurs via a desorption of a disulfide that is rate-limiting, and then replaced by a thiol. The most puzzling feature of exchange and desorption is that a significant fraction of thiol remains on the surface. In the desorption and exchange figures above more than half of the original thiol can remain on the surface over a period of 6 days. The rate of self-exchange and desorption tapers off and appears to go to zero. The proposed explanation for non-exchanging or desorbing thiols is from defect sites.

Defect sites on a gold surface could allow for a stronger binding energy to thiols. Surfaces made from sputtering or evaporation are known to be defect rich. Defects are also generated on gold when thiols are deposited, but these holes are actually pits in the underlying gold, rather than vacancies in the monolayer [42]. These defects on flat gold appear to be step-edges. Thiols have been shown to bind more strongly to these step-type defects by up to 6 kcal more than flat surfaces [42]. This additional 6 kcal would translate to a desorption rate 10,000 times slower than thiols on a flat surface. The figures above indicate the self-exchange and desorption rate are on the order of days. This means the rate of desorption of thiols bound to a defect site would be on the order of decades. Since porous gold is by nature, a defect rich surface, we explore the desorption of thiols on these substrates in the next chapter. Thiols binding to defect sites with a stronger energy also increases the adsorption energy making them more favorable to bind to the surface.

We have now completed our review of all the theory required to understand the QCM experiments performed in this dissertation. The models presented provide us insight into the workings of a QCM. This insight has allowed us to increase the sensitivity of the QCM by more than three orders of magnitude, beyond that of any publication. As we have shown, adding a solid and rigid mass to the sensor causes no additional dissipation. We utilize this property to increase the adsorption area of the QCM in the thickness direction by fabricating a porous gold substrate. From understanding the effects of viscous loading, we have described how lower frequency QCM such as the 5 MHz sensors used in this work, are more ideal for use in liquids. The theory behind ideal and non-ideal masses provide insight into the limitations of these surface modified devices. Lastly, the chemical basis behind the thiol-gold binding gives us a model to explain our kinetics.

Through this chapter we have presented a few of the variables that put a potential limit on the sensitivity increases possible to the QCM. The base resonant frequency puts a strict limit on the amount of solid mass that can be attached to the QCM while still allowing resonance. How the sensitivity scales with base resonant frequency further defines the optimal thickness of these surface modifications. The non-ideal properties of thiol in liquid causing a non-negligible dissipation from these coatings further restrain the maximum sensitivity increase possible for thiol adsorption in liquid. In the following chapter we present our experimental results to indicate the limit of sensitivity increase possible on a surface modified QCM. We find when used in liquids with thiol coating the limit is a 3 μm thick porous gold substrate, with a final sensitivity increase of 1000 times over flat sensors.

CHAPTER 3: NANOPOROUS GOLD FABRICATION & CHARACTERIZATION

3.1 Overview

In this chapter we present the detailed experimental work we performed to increase the sensitivity of the QCM by more than three orders of magnitude. We begin with our experimental setup including how we measure our QCM and collect data. We then discuss the cleaning process used to perform an experiment. The custom-built plasma cleaner we built is introduced along with the evidence used to verify our cleaning method. Our porous QCM fabrication technique is detailed along with the sputtering conditions used to tune our atomic ratio and porous gold. Next we present the results of a select few porous substrates.

We introduce our porous QCM results with two 50 atomic percent porous gold substrates that act much like a rough surface. We then describe our ideal 430 nm 31 atomic percent gold substrate that increases the QCM sensitivity extremely efficiently. We go into great detail characterizing this substrate because it is the most efficient per unit height at adsorbing thiol in low concentrations. We compare these results to other publications for reference, along with the theoretical sensitivity increase allowable in vacuum. To characterize the 430 nm substrate, we take SEM images and bind thiol to the sample over a variety of concentrations. We find this porous gold QCM can easily detect ultra-low concentrations of thiol in the 8 ppb range. We compare the amplitude of this porous substrate to a flat QCM in air, water, and n-hexane. With promising results and an 85-fold increase in sensitivity we move on to larger porous gold QCM.

We characterize our 2.56 μm and 3.0 μm thick porous gold QCM by performing high concentration thiol experiments. We find the frequency change of porous QCM is dependent on the concentration of thiol used. The 3.0 μm thick sample is found to increase

thiol adsorption by more than 1000 times. We then present our results with fabricating porous gold onto higher frequency 27 MHz QCM. The kinetics of our flat gold and porous substrates are then fit with the Langmuir isotherm model and found to be in good agreement. We perform desorption experiments and determine that our porous gold is defect rich, indicating the thiol binds to the surface stronger than on a flat QCM. We conclude the chapter with a summary of our experimental porous gold results.

3.2 QCM Data Collection

To perform our experiments, various methods to drive and measure the QCM have been explored. The SRS QCM-200 was tested, as it provides a Teflon holder for use in liquids, software to log the frequency, and is a user-friendly introduction to QCM measurements. The Teflon holder provided can be used with other measuring systems and is commonly used in liquid QCM experiments. Other advantages of the QCM-200 are the capacitive compensation feature, and variable measurement time scales. The high speed time setting offers 0.1 second measurements of frequency with 1 Hz resolution, whereas the 10 second time setting offers 0.01Hz resolution [13]. However, the QCM-200 only provides data for the frequency and resistance of the QCM being measured, and is not capable of providing an amplitude plot of the resonance. Without an amplitude plot the Q of the resonance cannot be measured. The QCM-200 works well for measuring thiol adsorption in liquids, especially at high speeds. Due to the high speed measurement capabilities of the device we use it for measuring adsorption kinetics of flat QCM.

The OpenQCM device is a simple, small, and portable QCM measuring system that was also explored. While this device may be useful as a low power and compact measuring tool for the QCM, it did not provide the necessary reliability and analysis capabilities

needed for our investigations. Nonetheless the device was capable of measuring thiol adsorption on our porous QCM in liquids without much problem. This is impressive considering the device is so simple; using only a Pierce oscillator circuit, along with an Arduino Micro as a clock, processor, and counter [17]. The eight component Pierce oscillator circuit was found to drive the QCM at resonance extremely efficiently. Once a QCM experiment is fully understood, the kinetics well known, and the sensor specified to detect a known ordinance, an OpenQCM like device may provide a useful solution as a low-power portable sensor.

For scientific research a network analyzer is by far the superior device to be used. Network analyzers are large pieces of scientific equipment, they are not portable at all, but are extremely accurate, precise, and provide much more data than the other devices being compared. The network analyzer can scan a specified frequency range, in specific intervals, and a power level input by the user. The output is then an amplitude plot of the frequency range that was scanned, and can then be fit to find the max frequency, Q, and amplitude. While we have done our experiments on various network analyzers, the primary one that was used was a HP Keysight 8751A network analyzer with built in high stability 10 MHz frequency reference. This device was controlled by our custom built LabVIEW VI to send commands and record data.

For all our experiments in liquids and air we powered the QCM with -10 dBm or 100 μW of power. Power output below -20 dBm had difficulty resonating the QCM in liquids and output a noisy signal with decreased amplitude. Increasing the power output in liquid experiments is common, however we observed no increase in amplitude or stability by increasing the power beyond -10 dBm. Power output beyond +5 dBm actually increased

noise in our experiments in liquids. For vacuum experiments 100 nW of power was more than ample. For low temperature experiments in vacuum we observed higher power outputs produced enough heat that the QCM was actively heated and was able to remove thin films of helium from the substrate. Thus low power settings are vital for delicate low temperature experiments, making a network analyzer greatly advantageous over the QCM-200 for low temperature measurements. Data was collected using 100 to 200 points, and typical scan time was between two and ten seconds.

Figure 30: QCM holders and measuring devices explored can be seen above with ruler for scale. The QCM on the top left was a custom holder made for low temperature helium experiments. The white rectangle in the top right is the OpenQCM device. The network analyzer can be seen as the large box at the bottom. Sitting in the middle is the SRS QCM-200 with Teflon holder displayed to the right of it. A small compact SC-cut QCM can be seen in the top right.

Once our amplitude plot data is collected, LabVIEW then applies a fit to these data points using the circuit based mathematical model described in the theory chapter. After a fit is applied to the data, the software takes the derivative of the function to determine the frequency of oscillation. The LabVIEW VI further records the Q of resonance, error of the fit, and max amplitude of oscillation. The raw network analyzer data can alternatively be fit in Mathematica using a nonlinear model fit and estimating the circuit parameters discussed above. These fit functions work well for both liquid and air measurements.

To best measure the peak frequency, the span of measurement is controlled based on the experiment. Air and liquid experiments work well with a span of 500 Hz. For low temperature experiments in vacuum a span of 50 Hz is ample. In liquid experiments, due to the increased inductance and resistance, the Q is lower and thus the amplitude plot is broader. Due to this factor, many of the amplitude plots provided in this dissertation include a broader span so the full resonance curve can be observed.

A typical amplitude plot with a span of 500 Hz used to measure frequency in our QCM experiments was displayed in Figure 8. Below we display examples of broader spans to demonstrate the entire resonant curve. Since the network analyzer is limited to 300 data points, selecting an appropriate bandwidth to measure the resonance allows for more accurate fits of the data. There can be a disadvantage to taking too many data points on the network analyzer, as it increases the scan time. When measuring the binding kinetics of thiols, measurement time can be an important factor to consider. The importance of choosing a suitable bandwidth is exemplified in the figure below. When a broad span is used very few data points are collected over the peak of resonance. However, when we use a smaller span, there is ample data to measure the resonance curve accurately. A balance of

scan time, number of data points required, bandwidth, and expected frequency change must all be considered when setting up a QCM experiment with a network analyzer. Both the Mathematica and LabVIEW programs we use are capable of fitting broad and narrow spans of frequency, but more accuracy is available on narrow spans.

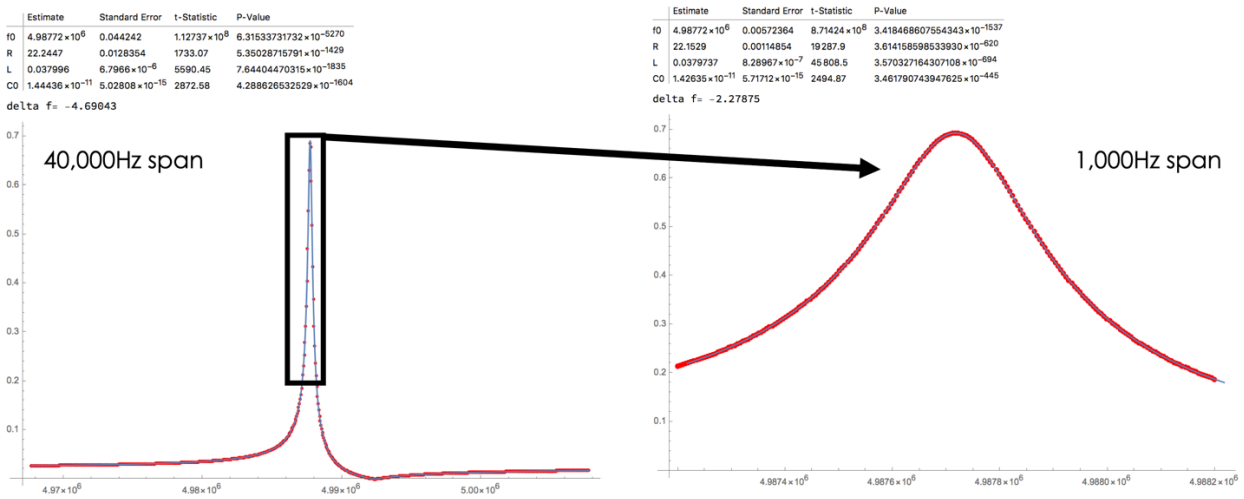

Figure 31: Our Mathematica fitting function can be seen above applying a fit to a QCM in air. The fitting function works well, even on an amplitude sweep with a large range, seen on the left. However, we take data on a smaller range, typically 500 Hz. This method allows us to accurately measure frequency changes of the QCMs.

3.3 Cleaning Technique and Verification

Since the QCM is sensitive to nanograms of mass added to the surface, thoroughly cleaning the sensor, holder, and all containers is crucial. Even small residues of contamination remaining on the holder or glassware can contain enough mass to fully coat a flat QCM. To clean our glassware, Teflon QCM holder, stir bar, and QCM we start with DI water mixed with soap and sonicate for a few minutes. We then rinse with DI water, isopropanol, ethanol, acetone, methanol to remove any acetone or evaporated contaminates, rinse with n-hexane twice as this is the solvent used in the experiment, and finally dry using inert nitrogen or argon gas. This cleaning process is iterated twice to ensure all contaminates and thiol is fully removed. This process works well enough that

we have not found it necessary to use chromic acid cleaning for our glassware. This solvent cleaning technique is fairly common in organic chemistry labs and mentioned by Sigma Aldrich for cleaning glassware [101]. However, this method does not clean the thiol bonded to gold. The strong S-Au bond requires more energy to remove the thiol, and simple sonication or solvents does not rinse the thiol away.

The common method to remove thiols from a gold surface is Piranha Solution. This technique involves using concentrated sulfuric acid mixed with hydrogen peroxide to drive a chemical reaction that cleans the gold surface of organic contaminates. However, this technique has the unfortunate consequence of etching away the chromium adhesion layer on the QCM sensor. This etching of the chromium adhesion layer causes the gold sensing surface of the QCM to delaminate and eventually fall off the QCM. Each time this cleaning technique is used, the quality and reliability of the QCM is deteriorated. Most publications suggest this method of cleaning can only be used a few times until the QCM is spent [1,7,13,30,31]. Further, piranha solution was recently found to both increase the roughness of gold surfaces and change the films crystal structure [102]. Since we are modifying the surface of a QCM and interested in the reliability and durability of this improved sensor we found a much less destructive technique to clean the gold surface of the QCM.

The alternative method used in this experiment to clean the gold surface of our QCM was oxygen plasma cleaning. Plasma cleaning allows us to remove all organic matter from the surface of the QCM sensor before we use it in our experiments. This is achieved by ionizing O_2 in a vacuum system, and has the advantage of being non-destructive to the QCM as well as being chemical free. Plasma cleaning also has an advantage over chemical

cleaning for our porous samples, as the plasma can quickly penetrate and clean porous media.

Figure 32: To clean our glassware and Teflon QCM holder we wash everything with DI water and soap, followed by sonication. We then rinse everything in the solvents seen above to remove all thiols and other foreign contaminants. This process is iterated twice to ensure proper cleaning. The QCM sensor follows the same procedure, and is then O_2 plasma cleaned to remove thiol bonded to the gold surface. A commercially available plasma cleaner can be seen on the right with QCM sensors inside. Typically, 100 watts of power was used for 10 minutes to ensure the QCM was clean.

We constructed our own plasma cleaner using a commercially available microwave oven along with a meter-long glass tube. This system is relatively simple and inexpensive to construct. The entire system could be built for less than $1000, which is 15 to 20 times less expensive than commercially available units. A roughing vacuum pump is used to remove air from the glass tube below 1 mTorr. A mixture of both air and oxygen from a gas cylinder is than added to the glass tube using a needle valve to control the pressure. The pressure is allowed to stabilize at 200 mTorr before the microwave is turned on. The microwave then ignites a nitrogen plasma in the central region of the tube. The nitrogen ignites a secondary oxygen plasma at both ends of the tube sticking out of the microwave. This secondary excitation of oxygen is also often found in in delicate instruments like a SEM.

It was found that placing the QCM inside the microwave where the nitrogen is ignited causes the sensor the sensor to be destroyed. The electromagnetic microwaves remove the piezoelectric property from the QCM and cause the sensor to no longer oscillate. However, when the QCM is placed in the oxygen plasma region on the outside of the microwave, the sensor is undamaged, adsorbs no additional heat, and is cleaned well in a short amount of time. We found our 1,100 Watt microwave had more power than necessary, so a Variac was used to control the power. Alternatively, if a Variac is unavailable, the power settings on a microwave could be used to control the power.

With the Variac, our microwave uses 600 watts of power and can fully clean a flat sample in 60 seconds. This cleaning time was roughly 10 times faster than commercially available units running at 100 watts. We observed commercially available units will also considerably heat up a sample, whereas our samples placed in the oxygen plasma remain at room temperature. To clean porous samples, we found a cleaning time of 150 seconds was ample to remove all surface contaminates. Cleaning times were tested up to 500 seconds but we observed no additional benefit in terms of contact angle or thiol adsorption.

A plasma cleaner does not magically clean all surface contaminates instantly. The cleaning rate is on the order of nanometers per second, and is typically used as a final cleaning step after chemical cleaning has been performed. In a plasma the gas atoms are ionized and excited to a higher energy state. As the atoms relax to their lower energy state they release a photon of light. This light is associated with the plasma and characteristic of each gas used. Oxygen plasma is known to be effective in breaking most organic bonds of surface contaminates. Ionized oxygen, ozone, and free electrons in the plasma further react with hydrocarbons and organic contaminants to produce an ultra-clean surface.

Figure 33: Our custom built plasma cleaner can be seen above. A commercially available microwave was used as our RF power source, and a Variac was used to control the power. The oxygen and air mixture flows into the glass tube through a needle valve to the left of the tube. The hose on the right of the picture leads to a pressure gauge and vacuum pump. The pink plasma seen inside the microwave is nitrogen. The yellow plasma found on both ends of the tube outside the microwave is a secondary ignition of oxygen. Since the oxygen is excited through a secondary ignition, it means no microwaves or heat can damage our sensor that is placed near the end of the tube.

The plasma cleaner was found to work well with just air and no additional oxygen, however without adding oxygen it took longer to fully clean the sample. When only oxygen was used it was difficult to fully ignite the plasma. A mixture of air and oxygen was found to work best for our cleaning applications, as it provides enough nitrogen to ignite the oxygen plasma, and enough oxygen to quickly clean our samples. To determine the effectiveness of our plasma cleaner we did a study of both the contact angle of water, and QCM thiol adsorption. The thiol adsorption showed consistent results of the custom built plasma cleaner removing thiol from the QCM without damaging the sensor.

Measuring contact angle is a commonly used technique to determine the cleanliness of a substrate. On a clean gold surface, the water will spread spontaneously over the metal

and produce no contact angle [103]. Conversely, a dirty or thiol coated gold surface will allow the drop of water to be more hydrophobic, and thus have a larger contact angle. The contact angle results seen below conclude a combination of both chemical cleaning and plasma cleaning produced the cleanest surface.

Figure 34: A macroscopic view of the contact angle of a drop of water placed onto an uncleaned QCM (left), and a clean QCM (right) can be seen above. The clean QCM was washed with DI water and soap, then an array of solvents, and dried with nitrogen. This chemical cleaning process was iterated twice. The QCM was then placed in our custom built oxygen plasma cleaner for 60 seconds before a drop of DI water was placed on the surface. It is known a clean gold surface will produce nearly no contact angle, whereas a dirty surface will produce a contact angle much larger as is demonstrated above [103].

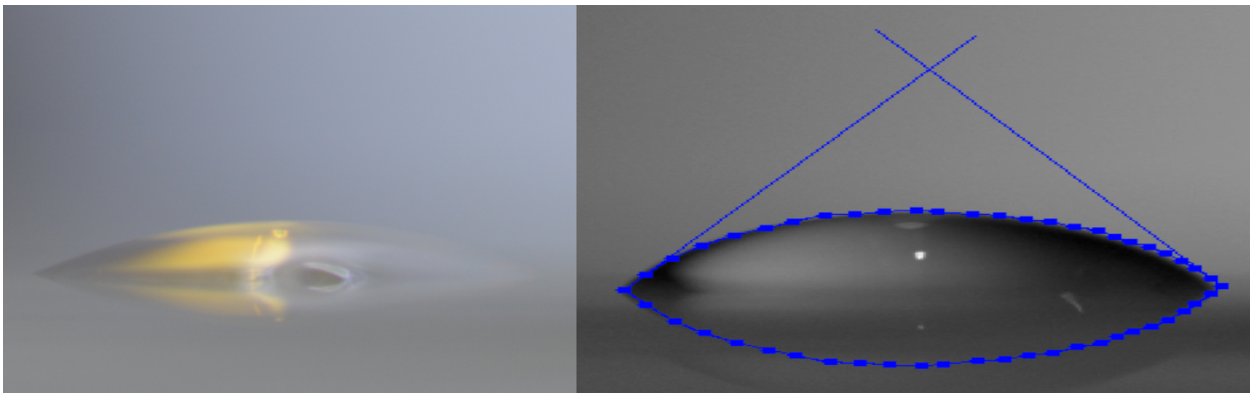

Figure 35: The detailed results from chemically cleaning the surface of a QCM can be seen above. The image on the left shows a color image of the water drop on a QCM cleaned with soap and water, along with our solvent cleaning method described above. ImageJ was used to add data points to the water curve, seen on the right, and measure the contact angle. The results show a contact angle of 20^{o} for a soap and solvent cleaned surface. This indicates the surface is not fully cleaned, and may contain trace thiols or other foreign contaminants.

Figure 36: The results from oxygen plasma cleaning for 60 seconds after chemically cleaning the surface of a QCM with solvents can be seen above. The angle was measured to be less than 2^{o} thus indicating a clean surface, free of thiol or contamination [103]. This is noticeable due to the flat nature of the drop and difficulty to see. The measurement indicated our cleaning method was sufficient for this experiment. It further provided an efficient and non-destructive method to clean our flat and porous QCM.

3.4 Flat QCM Baseline Thiol Measurement

To determine the baseline measurement of our experiment with a flat gold QCM we use 1-Octadecanethiol in n-hexane as was previously performed in other publications [30,31,35]. The solvent used was n-hexane 95% min. purchased from Fisher Scientific Catalog # H3064 due to its low sulfur compound content. The thiol was purchased from Sigma-Aldrich sku: O1858-25mL in powder form with 98% purity. A 1 mM stock solution of the thiol and n-hexane was mixed in a clean glass jar, and sonicated until fully dissolved.

To perform the experiment, 150mL of n-hexane was placed in a clean glass container. The QCM is cleaned along with the Teflon holder made for liquids, and placed into the container with n-hexane. A clean Teflon coated stir bar is added to the container to stir the n-hexane. The frequency of the QCM is allowed to stabilize in the n-hexane while stirred. Before use, the stock 1 mM thiol solution is sonicated for 5 minutes before 1.5 mL is removed in a new syringe and set aside to thermally equalize. After the QCM is stable, the thiol solution is injected into the n-hexane container with the QCM to measure the adsorption.

By adding 1.5 mL of 1mM thiol into a 150 mL of n-hexane we have a 0.01 mM or 3ppm concentration of thiol. As soon as the thiol solution is added the stable frequency of the QCM quickly drops as the sulfur in the thiol chain binds to the gold surface of the sensor. The gold surface quickly saturates after a self-assembled monolayer is formed and the frequency again stabilizes. Vericat et al. have found 1-octadecanethiol has a surface coverage of 330 $\frac{\text{ng}}{\text{cm}^2}$ [35]. Whereas the Blanchard et al. results suggest a surface coverage of 310 $\frac{\text{ng}}{\text{cm}^2}$ [30,31]. Our 5 MHz QCM has a known sensitivity of 17.7 ng Hz^{-1} cm^{-2} [13]. This means we should expect a frequency shift between 17.5 - 18.7 Hz to fully coat our 5 MHz flat gold QCM. Our results seen below show we find a frequency shift of 18 ± 0.5 Hz correlating to a surface coverage of 320 $\frac{\text{ng}}{cm2}$.

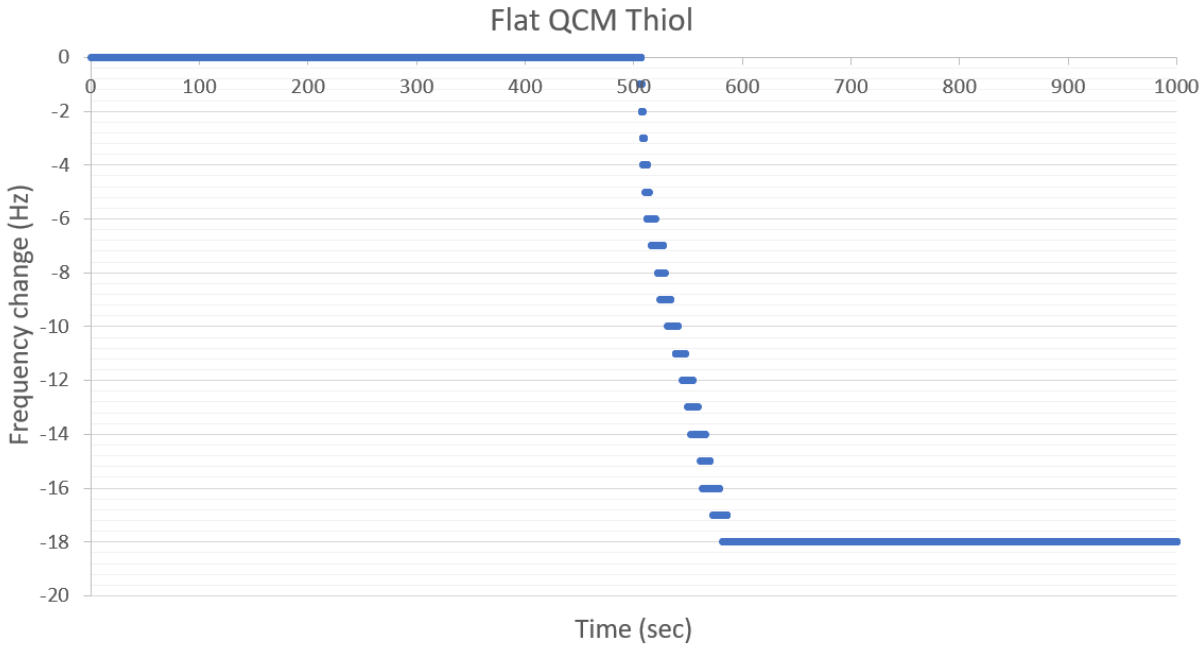

Figure 37: Our results for adding 1-Octadecanethiol to a flat 5 MHz SRS QCM in liquid n-hexane can be seen above. The frequency of the QCM was stable until a 1 mM concentration of the thiol is injected, creating a final concentration of 0.01 mM. After the thiol is added, the frequency quickly drops as the gold surface is coated and a self-assembled monolayer is formed. Within 60 seconds the QCM is fully coated and the frequency again stabilizes. This result correlates to a thiol surface coverage of 320 $\frac{\text{ng}}{\text{cm}^2}$ and agrees well with other known results of 1-Octadecanethiol on a flat gold QCM [30,31,35].

The surface coverage observed of 320 $\frac{ng}{cm^2}$ equates to 6.72 x 10^{18} $\frac{Thiol}{m^2}$ adsorbed onto the flat QCM surface per unit area. Since the flat QCM has an area of 1.27 x 10^{-4} m^2 we obtain 8.5 x 10^{14} thiol adsorbed in total. This value is similar to the calculated value of the number of gold sites on the surface. Using the gold packing area it can be calculated that there are 1.94 x 10^{15} adsorption sites on the flat QCM surface. This means there are approximately 2.3 times more gold sites than the number of thiol molecules adsorbed. This factor of 2.3 is accounted for by Van der Waals interaction between the molecules. The stock solution we inject gives a final concentration of 0.01 mM. With this concentration we are injecting approximately 6.0 x 10^{17} thiol into the clean hexane to coat our gold surface. This leaves an abundance of additional thiol in the solution that do not get adsorbed. The quantity of thiol used in a 0.01 mM experiment would provide enough thiol to coat approximately 700 flat QCM. When we perform experiments with porous gold, much more of this thiol is adsorbed from the solution.

To further confirm adsorption of our thiol coating we perform another contact angle measurement. After a thiol monolayer has formed on the surface of our gold QCM we remove the sensor from the holder. We then rinse the QCM in water to remove any additional hexane from the surface. A drop of water is then placed on the surface of the thiolated gold to measure the contact angle. A gold surface coated with thiol is expected to have a larger contact angle than a clean surface. The results below provide a secondary method to verify our thiol monolayer has successfully formed on the surface of our QCM.

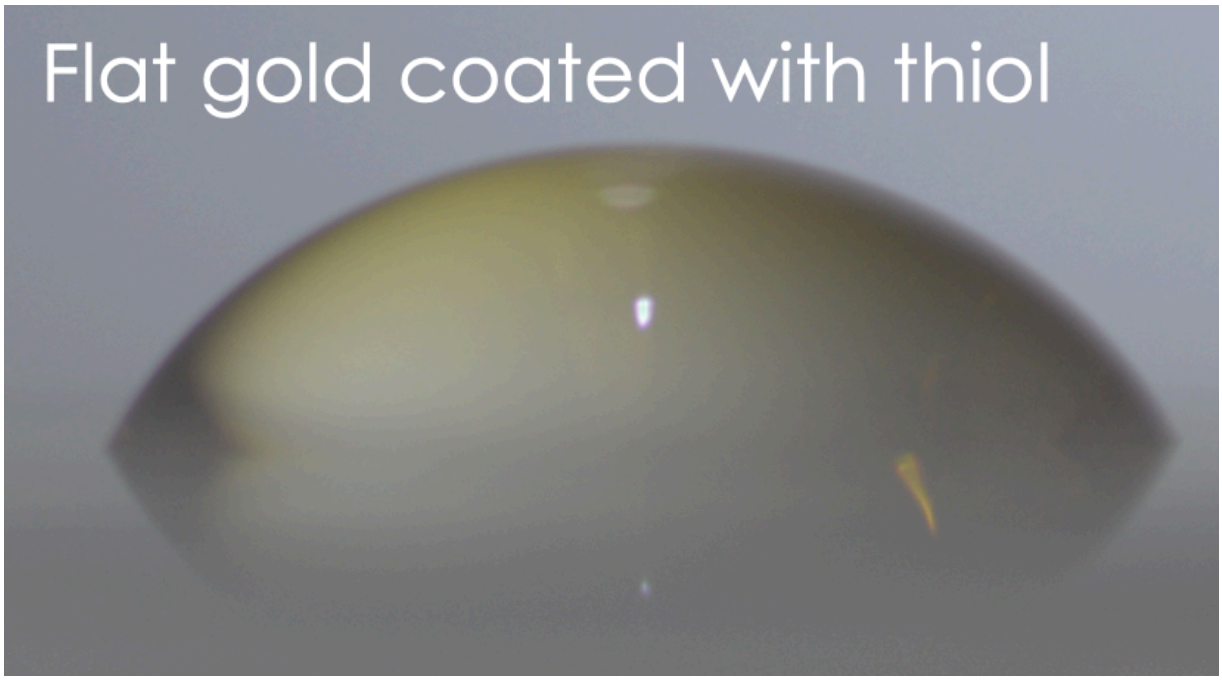

Figure 38: The contact angle of a flat gold surface coated with a monolayer of 1-octadecanethiol can be seen above. The result of 62° is in agreement with the expected result of a much larger contact angle with a thiol SAM. This experiment is a visual demonstration of the thiol binding to the gold surface.

The study of contact angles on various surfaces is a field of study in its own right [43,68]. In recent years particular attention has been paid to contact angles on porous surfaces. Porous surfaces tend to produce much larger contact angles that look more spherical than traditional flat surfaces. Chen et al. for example performed various contact angle experiments and even considered the effect of adding thiol to the porous surface [43]. These results indicated that porous surfaces coated with thiol should have a much larger contact angle than flat thiol coated substrates. To confirm these results, along with confirming the addition of thiol to our porous gold we performed a contact angle experiment as displayed below. We then present a summary of these contact angle measurements in table 3.

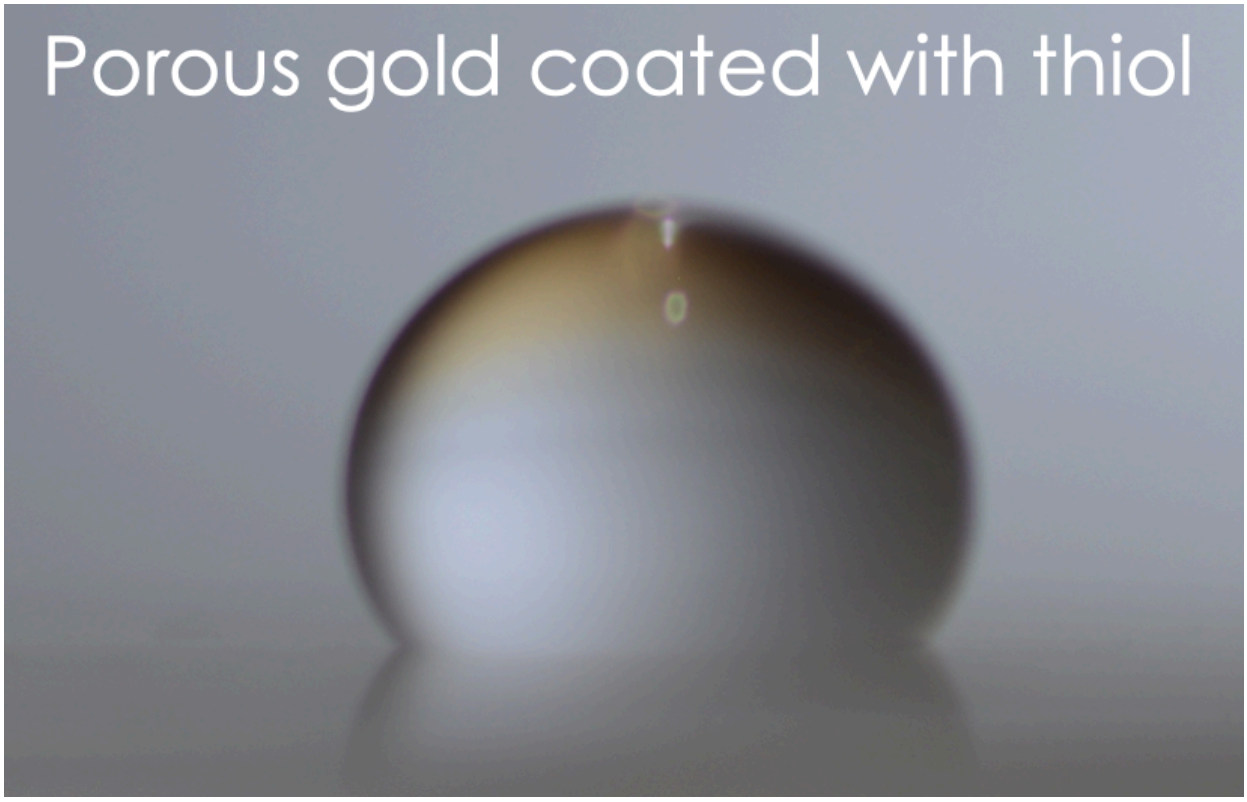

Figure 39: The image above shows our porous gold QCM has a contact angle of 130°. This larger contact angle for a porous sample coated with a thiol is to be expected as found by Chen et al. [43]. This experiment provides visual verification that we have cleaned our QCM effectively, created a porous gold surface, and added thiol to the substrate as well.

Method	Angle (degrees)
Chemical Clean	20
Chemical + Plasma	2
Thiol Coated Flat	62
Thiol Coated Porous	130

Table 3: A summary of the results from our contact angle measurements can be seen above. It demonstrates that our oxygen plasma cleaner produces cleaner gold surfaces than simply cleaning the QCM with soap and solvents. It further shows we have successfully attached thiol to our flat and porous QCM, and have indeed created porous media.

3.5 Porous Gold Fabrication

Porous media more recently has become a popular method to increase surface area of materials in the z-direction. It has found uses in optics [104], contact angle [43,68], and QCM [5–9,40]. Large porous alumina structures with a thickness of 13 μm have been

fabricated on QCM sensors before, allowing for a 120x increase in sensitivity as Taborek et al. indicated [5]. Porous gold on a QCM only has published results to a thickness of 3.3 μm and an increase of sensitivity of 64x for helium isotherms [6]. Porous gold as a use for increasing chemical sensitivity has only seen an 11x increase in thiol adsorption on a 180 nm thick sample [7]. In this study we increase both the thickness and sensitivity of the porous media to achieve a new record of sensitivity for thiols. We further manage to get a larger sensitivity increase on a porous media than ever before published, and do so using a thinner sensing surface.

The premise of forming porous gold has been well studied both experimentally and theoretically [6–8,71,104,105]. It has been created using various methods such as sputtering, evaporation, and electrochemistry [6–8]. To make the material porous an alloy of gold and some other material that can readily be added in an alloy of the correct ratio, and then removed easily is required. While copper could be used in the alloy with gold, due to the difference in mass, sputtering and evaporation using copper would be difficult. Both zinc and lithium have also been used to fabricate porous gold, however suffer the same problem as copper for sputtering [95,106]. Therefore, silver is often the best choice to make an alloy with gold as it has a closer mass to gold. This makes the two metals sputter at a closer rate. Silver further has the benefit of being easily etched away using nitric acid.

To fabricate our porous gold, sputtering was decided as the preferred method over evaporation or electrochemistry. While evaporation is the preferred method to add layers of chromium and gold to the QCM, adding an alloy of gold and silver proves difficult due to the different evaporation rate of both materials. In both sputtering and evaporation, silver

is preferentially deposited due to its lower mass than gold. However, in evaporation this difference is larger than in sputtering, requiring much more gold to be used than with sputtering. In fact, the rate of evaporating silver is roughly 3 orders of magnitude higher than gold. This means evaporation is costlier than sputtering a gold and silver alloy. This further demonstrates why sputtering is preferred when depositing an alloy of two materials with vastly different melting temperatures.

Sputtering is a process that ejects particles from a solid target material by bombardment of energetic ions in a vacuum environment. These energetic ions have much more kinetic energy than in a conventional thermal environment. This process leads to a prolonged period of ion bombardment of the target material, allowing the ejected particles to form thin film depositions. Sputtering allows various materials to be ejected and then form thin films on the desired substrate. In our case, we will use a mixture of silver and gold as our target, and our QCM as the substrate.

Our sputter system was designed as is typical, using an argon gas as our energetic ions, and a Kurt J. Lesker RF 2" magnetron to hold our target. The magnetron is water cooled to prevent overheating of the target. The target itself was made of silver 0.125" thick and 2" in diameter, with small millimeter sized gold pieces placed on top of it. All sputtering materials and gas were at least 99.99% purity. To prepare for sputtering, our QCM was first cleaned via our chemical and plasma cleaning method. This was found necessary as without plasma cleaning the QCM had adhesion issues between the gold surface and our sputtered alloy. The vacuum chamber used for sputtering was then pumped down below 0.4 mTorr to remove all air and any contaminates using a roughing pump and turbo. The chamber was then flushed with 200 mTorr of argon for 5 minutes

before the argon pressure was lowered using a needle valve to our desired sputter pressure. The argon pressure was allowed to stabilize for another 5 minutes to ensure it was constant. The argon is introduced to the chamber underneath the magnetron to avoid pressure fluctuations near the plasma. The sputter process was then started for our desired sputter time.

To power our Lesker magnetron we use an Advanced Energy RFX-600 600 watt RF power supply. This power output is then connected to an Advanced Energy ATX-600 automatic tuning device. The tuning device controls a separate Advanced Energy 5017-014-F that has a large array of variable capacitors along with large inductors. These capacitors and inductors are used to tune the plasma and minimize reflected power. When sputtering a variety of different variables must be tuned to achieve the desired result. The power used, sputtering pressure, throw distance, and amount of gold placed on our silver target had to be tuned for our desired results. It was also determined a constant flow of argon into the system while always pumping on the chamber was required for good results.

To fabricate our porous gold many variables were tuned and adjusted in our sputter system to obtain optimal results. The pressure of argon, power output, and throw distance between the target and substrate were found to be crucial to fabricate our porous gold QCM. While we were capable of making porous gold under a variety of circumstances, the deposition time also played a factor in determining our ideal sputter conditions. For example, sputtering at 200 mTorr argon pressure did produce good porous gold, but the sputter rate was so slow that it would be impossible to produce large micron sized films. By lowering the pressure of argon the sputter rate was substantially increased. By increasing pressure, the mean free path of the particles also changed, allowing more interactions

before striking the QCM substrate. At 200 mTorr nearly 300 interactions take place, whereas at 20 mTorr roughly 30 interactions occur. We found uniform distribution of silver and gold at this lower pressure, and it allowed us to increase our sputter rate by a factor of 10.

The sputtering rate also has a dependence on the throw distance and is proportional to the square of the distance. This means a closer target is coated much faster. However, we found 2.5" was the closest we could make the target to give good results reliably without causing adhesion issues due to too much heat. Changing the power, pressure, or throw distance was also found to change the ratio of silver and gold. Thus for each trial, the ratio had to be adjusted. Due to the dependence of all these variables, an alloy target was purchased, but was found untenable for our purposes. The attempted and optimal sputter conditions for our porous gold substrates is displayed below.

Sputtering	Range Tested	Best Results
Power	30 - 400 Watts	50 Watts
Pressure	3 - 300 mTorr	20 mTorr
Distance	1 - 6"	2.5"

Table 4: The range of variables attempted and our best results for sputtering can be seen above. These conditions allowed for a deposition rate of 1 $\frac{\text{nm}}{\text{s}}$ as measured by QCM.

While a gold and silver alloy target was purchased with a ratio of 70 atomic percent silver and 30 atomic percent gold, it was found not to sputter with the correct ratio. Due to this we opted for a more controllable method as mentioned before. By placing small gold pieces onto a silver target, the ratio of gold and silver could be adjusted. Publications suggest the ideal ratio for porous gold is of 70 atomic percent silver and 30 atomic percent gold [6,8]. We have fabricated porous gold with a ratio up to 50 atomic percent gold, and as little as 10 atomic percent gold. Through our research we have found the ideal ratio of gold

to be slightly higher than 30 atomic percent as will later be shown. We further found that using a few larger pieces of gold on the target can produce the same ratio as a dozen smaller pieces of gold. It was found advantageous to use fewer larger pieces of gold as the sputtering ratio remained constant for a longer period of time. Since the silver target is much more massive than the pieces of gold, the gold is depleted faster than the silver, and thus slowly changes the sputtering ratio with time. This factor is important for our work in increasing the thickness of the porous gold, and thus increasing the sputter time. Our typical sputter rate of our gold and silver alloy is $1\ \frac{\mathrm{nm}}{\mathrm{s}}$ as measured by QCM.

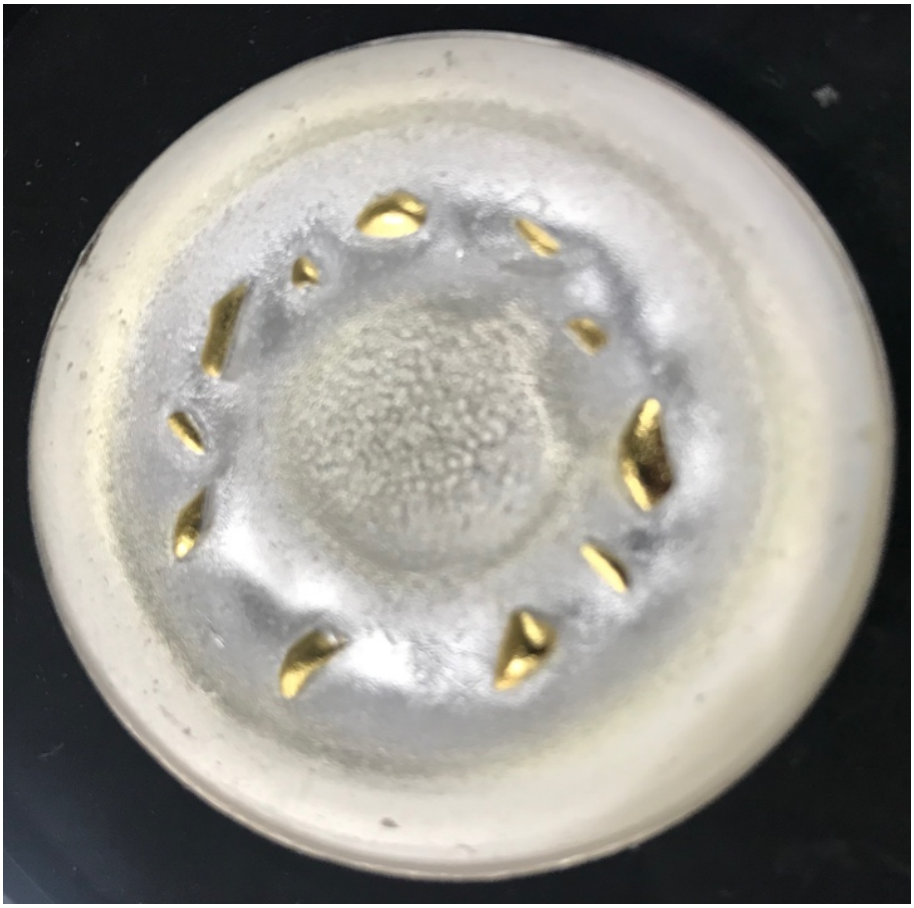

Figure 40: An image of our sputtering target can be seen above. The 2" silver target was purchased from Kurt J. Lesker with a 99.999% purity. The small gold pieces were cut off a 99.999% gold bar to allow the ratio of silver and gold to be adjusted. Using a few larger pieces of gold was found to work better, as it allowed the ratio to remain consistent for longer sputtering intervals.

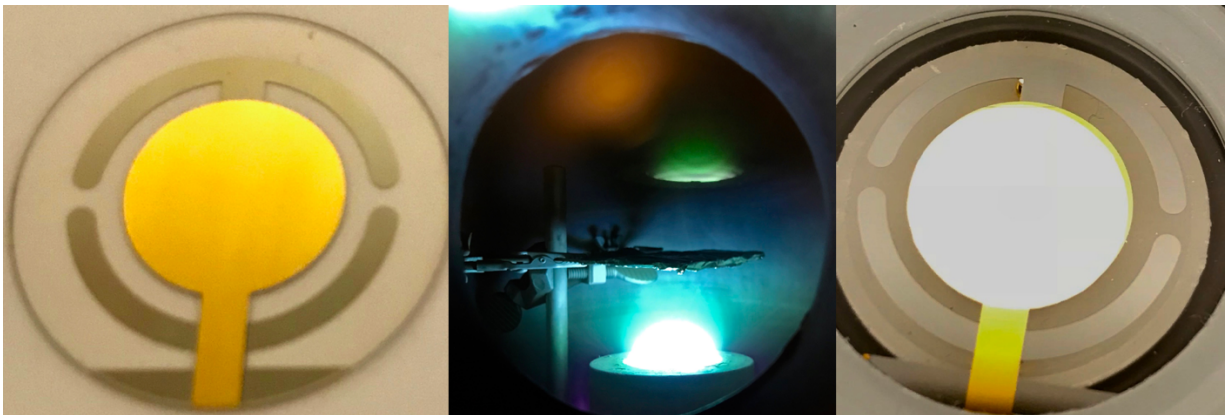

Figure 41: A clean commercially available gold coated QCM placed into our sputter system at a height of 2.5" (left). The sputtering of our gold and silver produces a green-blue plasma, with hints of pink argon near the bottom of our magnetron (middle). A thin aluminum mask is used to hold the QCM in place over the center of the magnetron, and only add the film onto the gold sensing surface. The resulting film is mostly silver colored with a mirror like finish, a hint of gold color can be observed when comparing to a silver mirror seen on the right.

Once a gold and silver alloy has been deposited on the QCM, to create porous gold the silver must now be completely removed. To remove the silver, we use a method found in various other publications, 70% concentrated nitric acid [6,8,70]. The nitric acid etches away the silver while leaving the gold fully intact. Removing silver from an alloy with gold is well studied with etch times ranging from 1 minute to 1 week [70]. We attempted to heat the nitric acid, however found this caused the pores to collapse, and changed the color from black to orange. These orange substrates performed poorly, similar to the 50 atomic percent porous gold we created and later discuss. Our experiments found an etch time of 1 hour at room temperature was adequate for substrates with thickness of order of a few microns. Etching for days caused the chromium adhesion layer to deteriorate and destroy the QCM. While etching for a few minutes did remove most of the silver, it was found that a few percent of silver still remained. The extremely porous nature of our samples was largely due to this near complete depletion of silver from our alloy.

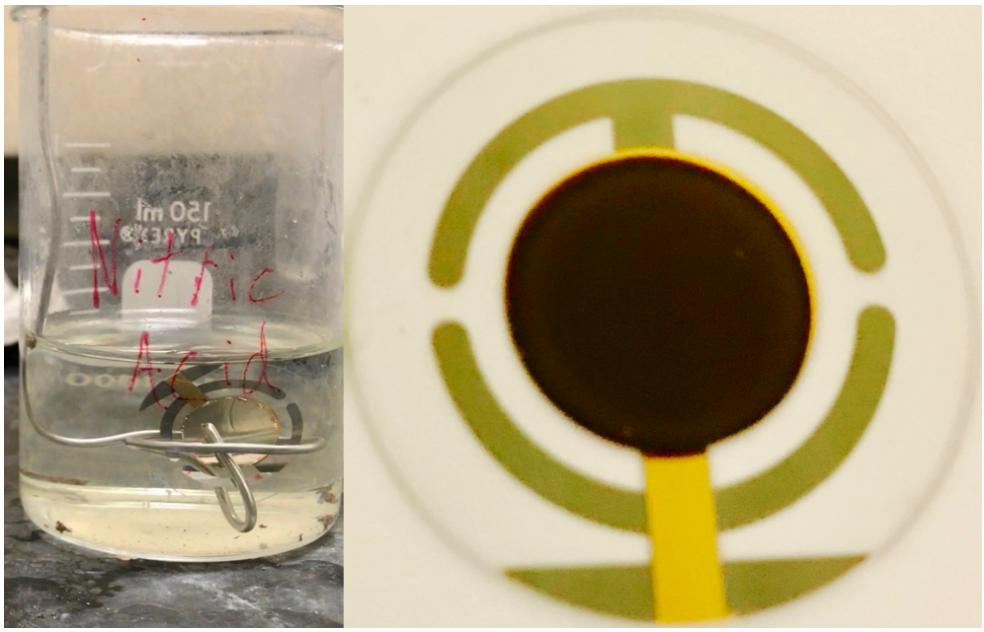

Figure 42: An image of etching our sputtered alloy of gold and silver in a bulk solution of nitric acid can be seen above on the left. After etching for 1 hour, the QCM was removed from the nitric acid and rinsed in water. The resulting product is a black surface made of the remaining 30 atomic percent gold. The black nature of the porous substrate gives diligence to a nicknames for it "black gold".

Masking the QCM during the sputter process was originally performed to contain the sputtered film to the center of the sensor. It was later determined that the thickness of the mask slightly changed the atomic ratio of the film near the edges of the sensor. This slight deviation of atomic ratio near the edges of the film plays little consequence, since the QCM is only sensitive in the central region of the oscillator, as discussed previously. It was nonetheless determined that a mask was not necessary. In the fabrication of the QCM a chromium adhesion layer is used to bind the gold coating with the quartz surface. Without this adhesion layer, the gold can easily be removed. Thus we determined we could sputter the QCM without using a mask, and simply remove the coating on the quartz surface when we etched the substrate in nitric acid. This method of sputtering without a mask proved successful and provided a uniform coat over the entire surface of the QCM. An example of our QCM sputtered without a mask is displayed below.

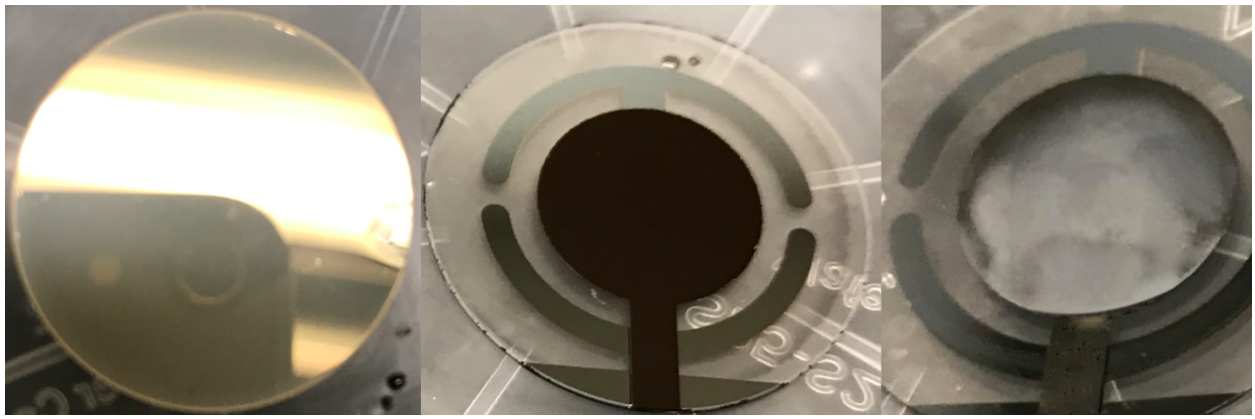

Figure 43: A QCM sputtered without a mask is shown in the image on the left. The silver and gold alloy produce a mirror like surface over the entire QCM. After etching the QCM the surface appears a uniform black color as shown in the middle. After coating with thiol the porous structure appears white-grey in color seen on the right. After being cleaned of thiol, the porous gold returns to its original black color in the middle image.

3.6 Porous Gold Characterization: QCM & EDS

To determine the atomic ratio of gold and silver on our QCM we utilized two reliable methods. The primary method was by using the QCM itself, along with the atomic weights of both silver and gold. The secondary method was using electron diffraction spectroscopy (EDS) to verify these measurements on the FEI Magellan 400 scanning electron microscope (SEM). The SEM features a resolution better than 1nm, and the EDS was calibrated with copper before use. To measure the ratio of gold and silver using the QCM a standard procedure was applied. The QCM was cleaned and the fundamental frequency of the flat QCM was measured. After the QCM was sputtered, it was allowed to cool down, and the frequency of the gold and silver alloy was measured. Finally, after etching the QCM was chemically cleaned and the frequency of the porous gold was measured. By knowing the 3 frequencies, atomic weights, and sensitivity of the QCM, both the height and ratio of the porous gold could be calculated. This calculation is rather trivial, the Sauerbrey equation works exceedingly well at providing the correct solution as confirmed by EDS and SEM.

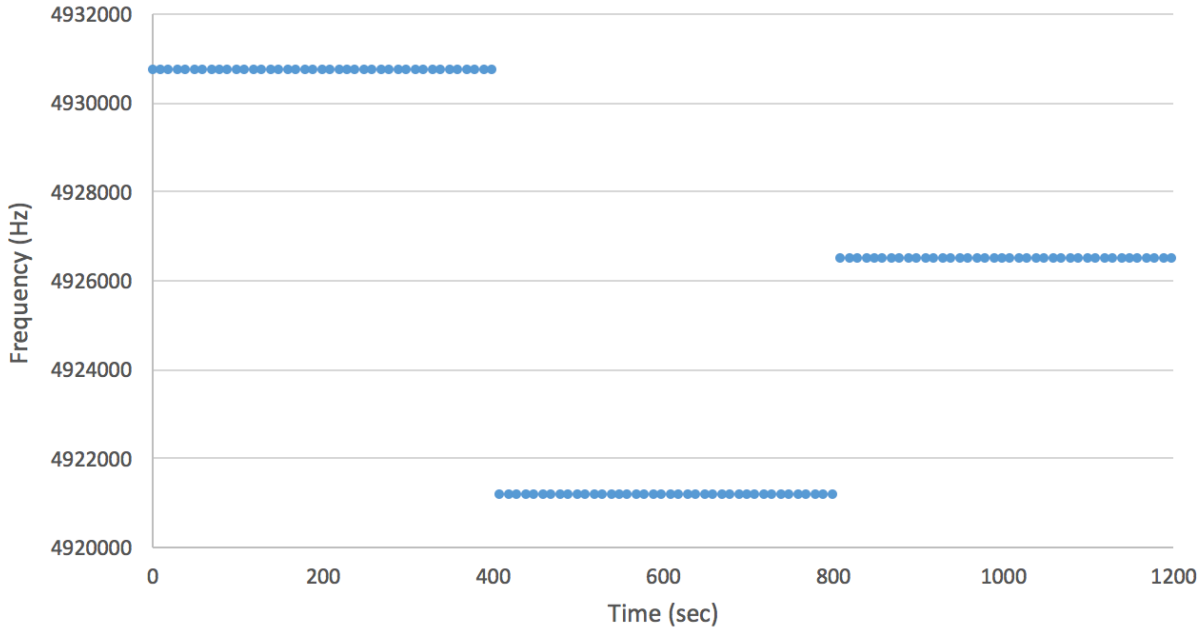

Figure 44: QCM measurements from producing a porous gold substrate can be seen above. A clean QCM is measured for the fundamental frequency. After sputtering a 30 atomic percent gold and 70 atomic percent silver alloy the frequency is again measured. The final result, a porous gold substrate is measured. Since the QCM measures areal mass density, we see 56% of the frequency shift is due to silver, and 44% is due to the gold. Thus 44% of the frequency shift from sputtering the alloy remains on the sensor. This method proves extremely reliable and finds less than 0.5% difference with EDS.

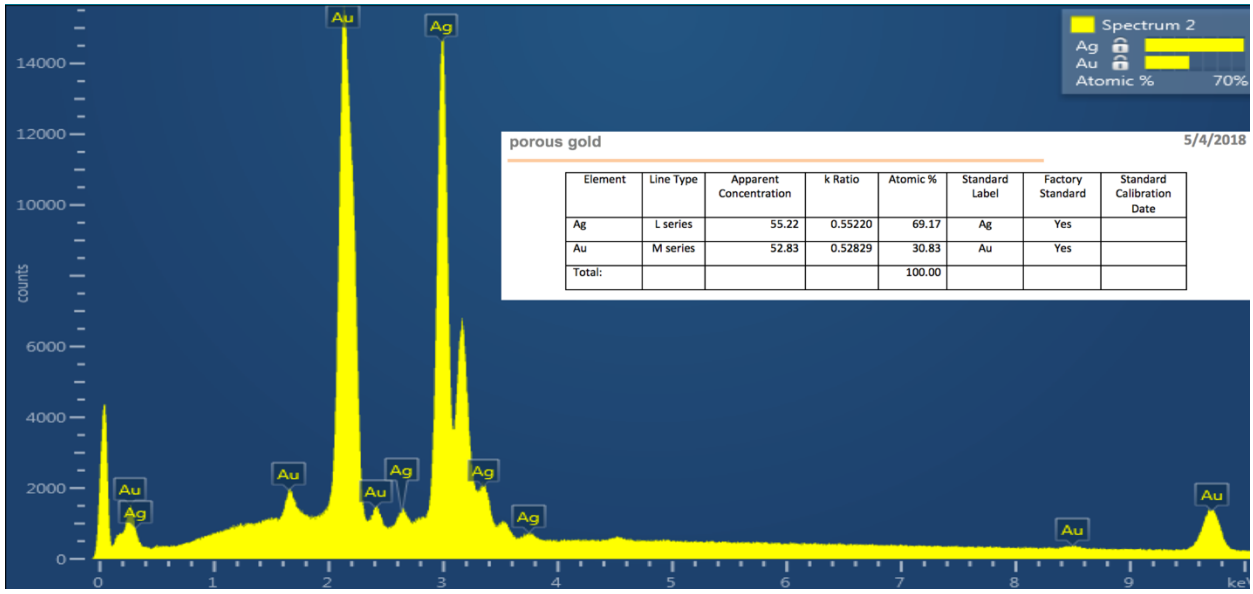

Figure 45: The results of our EDS measurement can be seen above. It demonstrates we find 30 atomic percent gold and 70 atomic percent silver in our sputtered samples. This further verifies our QCM results provide accurate measurements of atomic ratio.

Element	QCM calculated ratio (atomic percent)	EDS measured ratio (atomic percent)
Gold	30.32	30.83
Silver	69.68	69.17

Table 5: To measure the EDS ratio of gold and silver, our QCM must first be destroyed. This means to compare our QCM results to our EDS results, we must perform two identical and sequential results. Since the ratio of silver to gold changes each time the sputter system is used, the results above indicate both the rate of change of the sputter system and the accuracy of our QCM measurement system. In the first run a QCM was sputtered but not etched, and measured on the EDS after being destroyed. On the second run a QCM was sputtered and etched using our QCM ratio measurement method. We found slightly more silver on the second run using our QCM method. This difference may be due to more silver being present on the second run as the gold is slowly depleted. Nonetheless this demonstrates our QCM measurements fall within 0.5% of the EDS results.

As was mentioned, the 30 atomic percent gold ratio has importance to our goal of increasing the sensitivity of the QCM. This ratio largely comes from prior work in theory and experimental research, and has its origins in percolation theory [107,108]. Percolation represents the threshold at which a liquid can pass through a porous media. If there is too much material, the liquid cannot penetrate the media. If there is not enough media, there is less surface area and the structure is less stable. Since we are binding thiol to our porous media in a liquid, it is critical the liquid is able to fully penetrate the substrate. However, because gold is our binding surface, using less gold than the percolation theory predicts provides less possible sites for thiol to bind to. Thus tuning the ratio of gold and silver to be as close to percolation theory as possible provides the most efficient porous structure for adsorbing thiol. As Cortie et al. explain the percolation threshold for silver and gold are rather different. For silver the threshold is 0.5, whereas for gold the value is found to be 0.31 ± 0.03 [108]. This result is shown with theory and validated with experiment [108]. Our results confirm this ratio holds true for attaching thiol to a porous media as well.

3.7 Porous Gold QCM: 50 Atomic Percent

During the route to finding the correct ratio for sputtering, two 50 atomic percent gold porous QCM were created and tested. The results found as expected that the substrate increased the sensitivity beyond that of what a flat surface is capable of, but not as greatly as is possible when using the correct ratio. The SEM and QCM results presented further demonstrate the validity of percolation theory. Various publications have explored the effect of surface roughness on a sensing surface and found a slight increase in sensitivity [1,9]. Our results demonstrate that 50 atomic percent gold compares to these methods, but is not ideal by far.

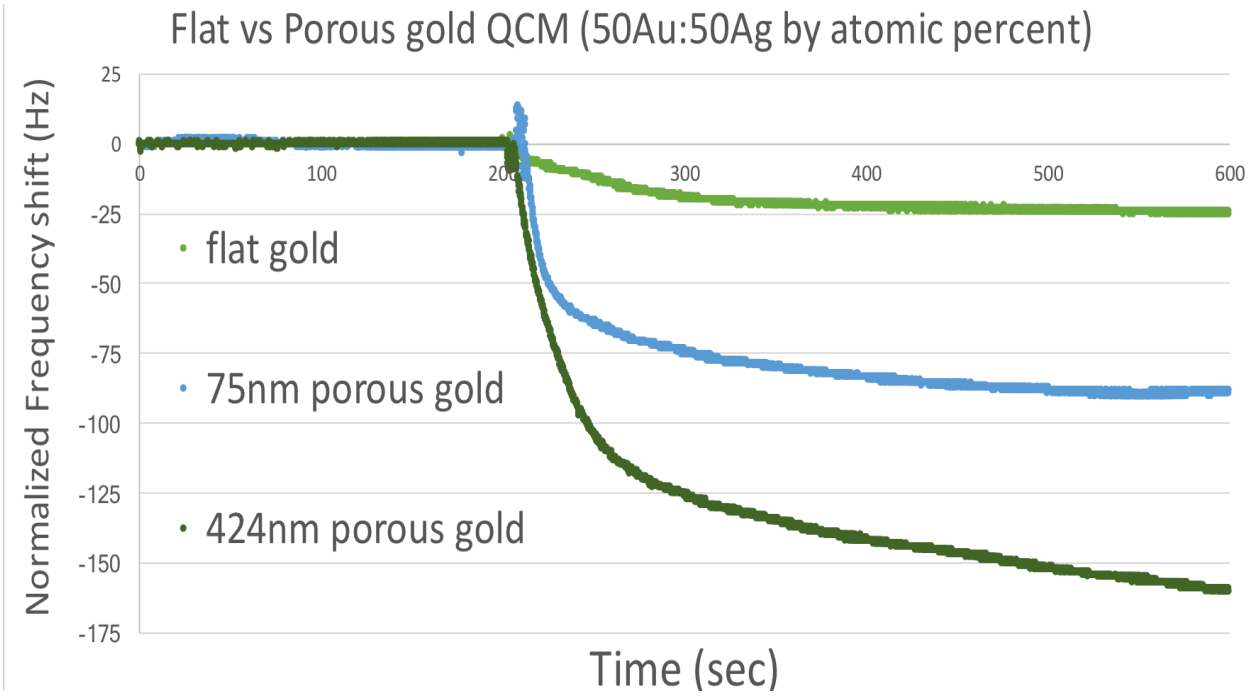

Figure 46: Our results for 50 atomic percent gold can be seen above when attaching a 0.01 mM concentration of 1-octadecanethiol. These results demonstrate 50 atomic percent porous gold does increase the surface area. We also see a larger frequency shift due to thiol adsorption in larger substrates. However, these porous samples do not achieve the potential that is possible as predicted by percolation theory and demonstrated by our results. From this we find a 4x increase of thiol adsorption on a 75 nm thick sample, and 10x increase in a 424 nm thick substrate.

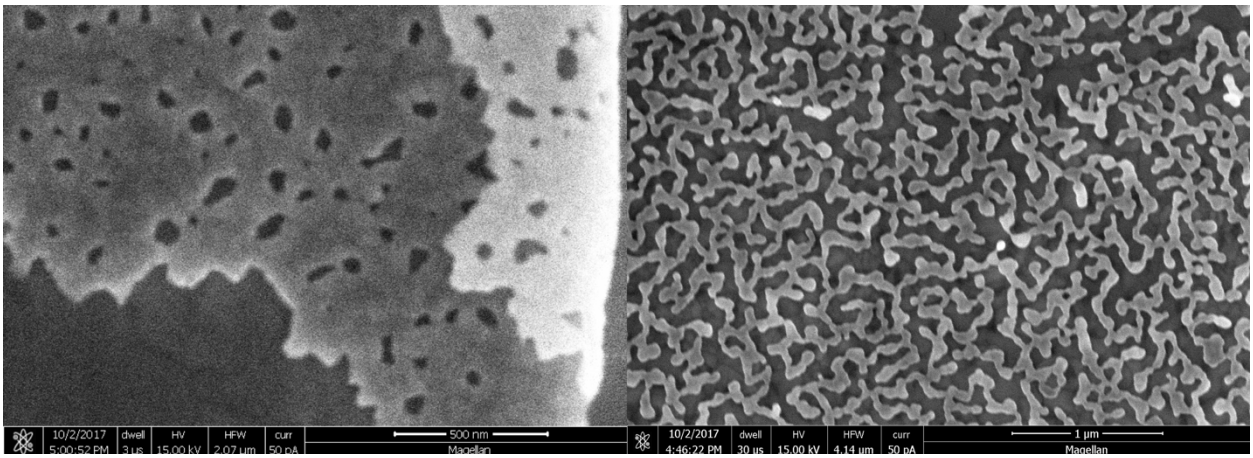

Figure 47: SEM images of 50 atomic percent porous gold can be seen above. On the left we note the nature of the of substrate is largely closed and solid, rather than porous. On the right we note we get a porous primary layer, but can see the layer terminates quickly, and does not penetrate the entire surface. This means the majority of the potential surface area is unused, and a lower ratio of gold will produce a substrate with more surface area.

3.8 Porous Gold QCM: 430 nm 31 Atomic Percent

We created an ideal 430 nm thick porous substrate that is 31 atomic percent gold as confirmed by QCM and EDS. This sample was found to be more sensitive than any other surface modified QCM per height than any other published result [5–9]. To create this porous gold, both ideal sputtering and etching conditions had to be determined as previously discussed. The results indicate these ideal conditions produce an extremely efficient porous structure. The results for this porous gold can be seen below and are compared to a flat gold surface along with a larger porous sample that has too little gold. The larger porous substrate was created using the same technique, but sputtered for a longer time with less gold. The 980 nm porous gold has a ratio of 24 atomic percent gold. Due to having 22% less gold than an ideal porous substrate, this larger sample is not as efficient as the 430 nm sample. Nonetheless due to its increased thickness it still adds more thiol than the thinner ideal porous substrate.

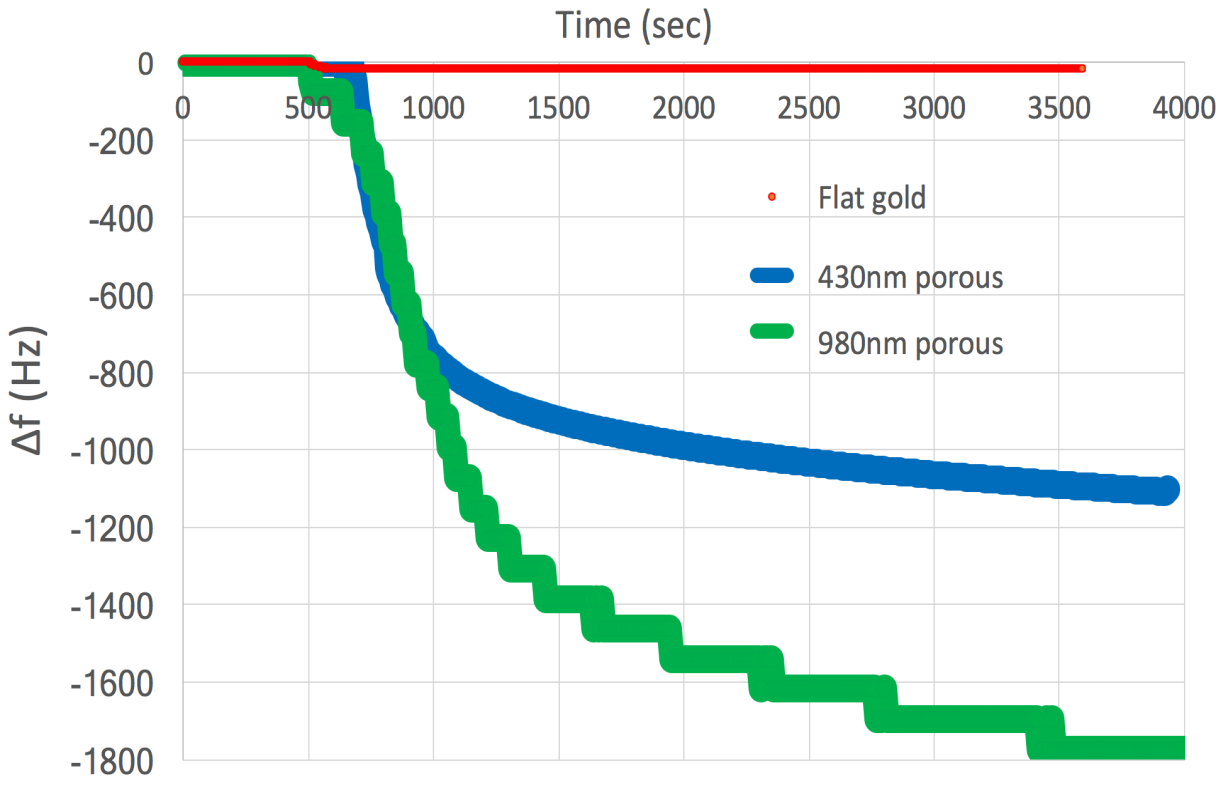

Figure 48: The results from our 31 atomic percent gold 430 nm thick substrate compared to a flat gold QCM can be seen above. The flat gold QCM seen in red changes 18 Hz in the first minute and stabilizes. The 430 nm porous sample in blue rapidly decreases in the first 10 minutes, and then slows down to add more mass for the next hour. The 980 nm 24 atomic percent sample in green follows a similar trend to the 430 nm substrate in blue. All frequencies are normalized so the base frequency in clean n-hexane is set to 0 Hz.

In the above figure a 0.01 mM 1-octadecanethiol solution was added to a solution of n-hexane at 500 seconds. The larger porous sample has more surface area, and thus falls rapidly for longer than the smaller porous sample. The larger sample also takes longer to fully saturate. Since the thicker substrate has less gold than the ideal 31 atomic percent, it is not as efficient at adsorbing thiol as the 430 nm thick sample. Since the 980 nm substrate is 2.3 times thicker than the 430 sample, we would it expect it to add 2500 Hz of mass. However, since the sample has 22% less gold than the ideal sample we would expect 22% less thiol to be adsorbed or 1950 Hz. When the 980 nm substrate fully saturates we

observe a frequency change of 1838 Hz, agreeing reasonably well with the expected frequency change based on its thickness and atomic percent of gold.

While a less efficient porous substrate is not desired for our particular experiment, it may be useful to have less gold, as seen in our 980 nm sample, for experiments detecting larger molecules. Our ideal porous gold with an atomic ratio of 31 percent has a pore size of 10 nm. This pore size works well for our thiol of size ~2nm, however if detecting larger analytes a substrate with larger pores may be useful. For example, the cowpea mosaic virus with a 30 nm diameter would not work well with our 31 atomic percent gold substrates. The virus is too large to permeate into the pores causing our ideal 430 nm thick sample to act more like a rough flat surface. Whereas the 24 atomic percent sample with 100 nm wide channels would work exceedingly well for these larger adsorbates.

We can normalize the results above in figure 48 by comparing them to the adsorption of a flat QCM to obtain the increase in sensitivity factor. To do this we divide the frequency change by 18 Hz, thus giving the flat QCM a baseline sensitivity of 1. This normalization provides an idea of how many times more mass is adsorbed by the porous samples. We present this normalized data by comparing flat gold, the 50 atomic percent sample, along with the two more successful substrates below.

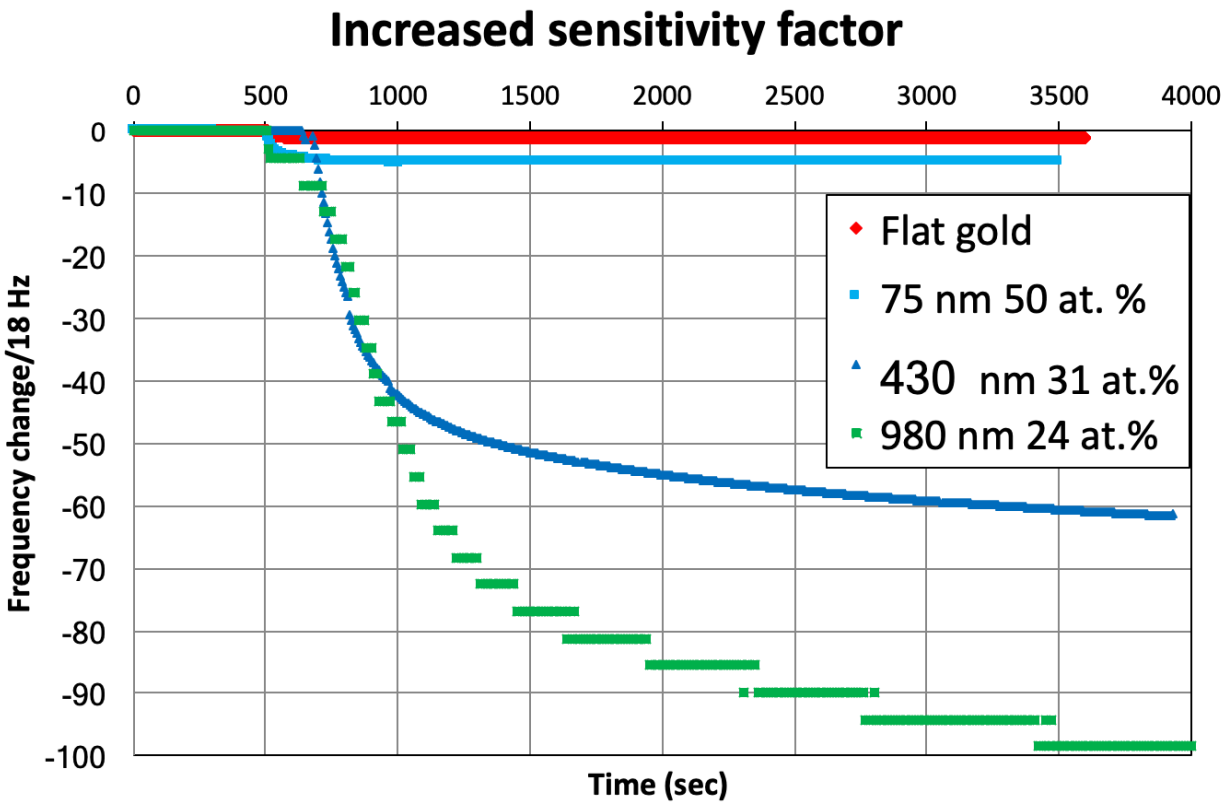

Figure 49: We now divide the frequency shift by 18 Hz to normalize a flat QCM to 1, and see the increased sensitivity of the porous samples. We note the published record for a porous gold QCM used for thiol adsorption is 11x [7]. The record for porous gold sensitivity increase is 64x using a 3.3 μm thick substrate [6]. This means our porous gold has a greater sensitivity increase per height added. The plot above further demonstrates the importance of the ratio of gold used to make the porous sample. Samples with too much gold act similar to a flat QCM with a rough surface. Samples with not enough gold work well, but are not as efficient as they could be.

3.9 Porous Gold QCM: Efficiency & Sensitivity Limit

The sensitivity increase per thickness added is an important aspect to consider. A QCM cannot be created infinitely thick; as more mass is added the frequency decreases, setting an obvious limit on thickness. Most sputter systems that use a QCM recommend replacing the sensor after 10% to 20% of the fundamental frequency shift has occurred. For example, typical 5 MHz QCM used for a commercial sputter system is often replaced after a 4 MHz frequency is reached. Since the base sensitivity scales as $f0^2$ in air or vacuum,

it also means as the fundamental frequency decreases, the sensor becomes less sensitive. In our case a flat 5 MHz QCM decreases frequency by 18 Hz when our thiol monolayer is added, but if it were a 4 MHz QCM we would instead see an 11.5 Hz shift. This demonstrates the importance of creating a porous substrate that adsorbs mass efficiently, as there is a limit on the maximum thickness that comes at the cost of sensitivity.

We exemplify this effect in the plot below where we consider the possible sensitivity increase factor in vacuum compared to the thickness of the porous gold. We take our most efficient 430 nm porous gold that is able to increase the sensitivity over a flat QCM by an additional factor for every 5 nm in thickness. As the thickness increases, the fundamental frequency decreases, as does the sensitivity. Using this method, we find the maximum sensitivity increase possible for porous gold in vacuum is a factor of 7500 times more than a flat sensing surface. While larger porous structures will indeed add increasingly more surface area, the diminishing frequency change from this additional mass causes the sensitivity to level out. As seen below adding additional thickness to a porous structure increases the sensitivity for the first 100 μm. After 100 μm however, adding additional thickness to the substrate gains no further sensitivity increase. Beyond around 200 μm, additional thickness of the porous structure actually decreases the sensitivity of the QCM. This model holds true for use of porous gold in vacuum only. It also assumes no dissipation from the additional mass added via the adsorbate or the porous structure itself. Nonetheless, it demonstrates that the possible gains to sensitivity by using a porous substrate are finite. Even when used in vacuum a maximum sensitivity increase allowed by a porous structure is set to 7500 times. When used in liquids, with dissipation from the

liquid and adsorbate, the actual limit on thickness is found to be closer to 1000 as will be later shown.

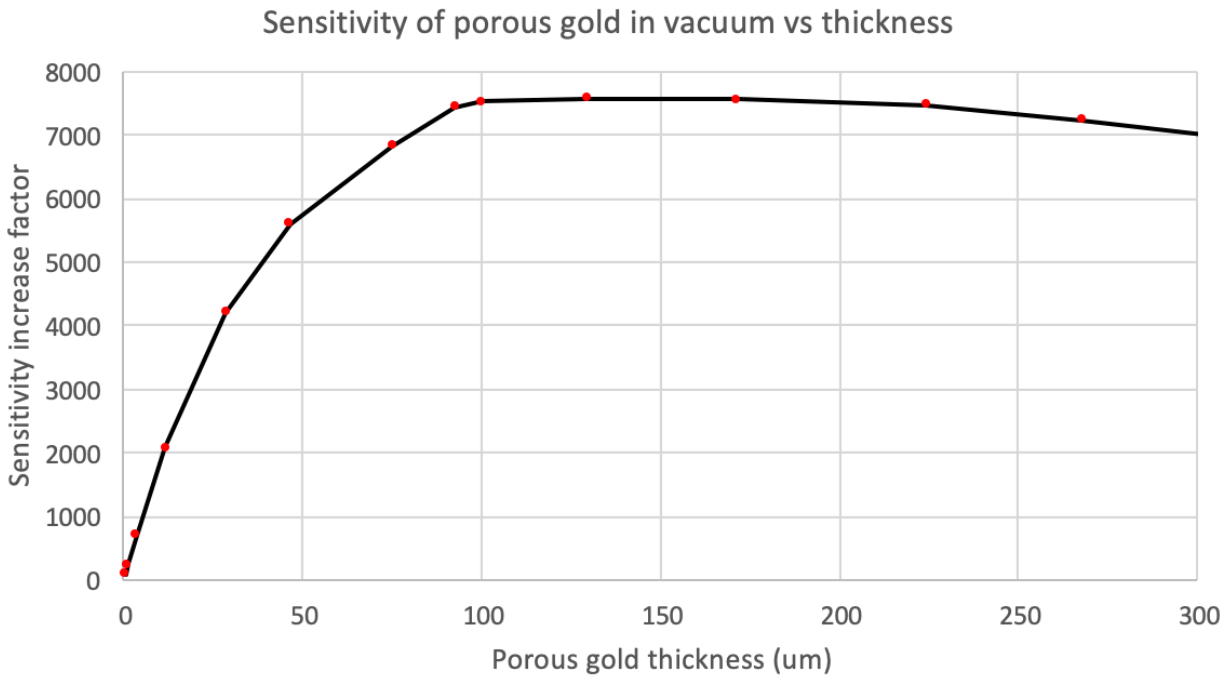

Figure 50: Using our most efficient 430nm porous gold substrate we predict the sensitivity increase possible when used in vacuum vs the thickness of the sample. As the thickness of the sample increases the sensitivity over a flat QCM increases as well up to a thickness of 100 μm. After 100 μm the thickness of the substrate becomes too great to overcome the base sensitivity that scales as $f0^2$. This causes the sensitivity to level out and eventually begin to decrease with additional thickness.

3.10 Surface Modified QCM Literature Comparison

Our results above show we need only 5 nm of thickness to increase the sensitivity one time for our 430 nm thick porous gold. To compare this to other porous gold substrates produced, we find Declerck et al. found 16 nm/sensitivity increase [7]. This means our porous gold is 2.5 more efficient in terms of height at thiol adsorption. The primary difference between these results may be that Declerck used electrochemistry to make the sample, whereas we used sputtering. However, other publications that used sputtering to make porous gold found 40nm and 52nm were required per sensitivity

increase [6,8]. The largest surface modified QCM was made using alumina, at 13 μm thick it found a sensitivity increase for every 110nm of thickness [5]. Thus far we have presented our results for our 430 nm porous sample fabricated with an ideal 31 atomic percent ratio, along with our 980 nm thick substrate with 24 atomic percent gold. Below we summarize these results and compare them with other published results for surface modified QCM. The table below demonstrates that we have already presented results for the most efficient surface modified QCM in terms of thickness needed per sensitivity increase. We can continue this trend to fabricate to most sensitive surface modified QCM by increasing thickness as will be shown.

Author	Year	Description	Method	Sensitivity Increase	Surface Area	Thickness	$\frac{\text{Thickness}}{\text{Sensitivity}}$
Chan [8]	2004	Porous gold	Vapor pressure	40x	38 cm^2	1.6 μm	40 nm
Declerck[7]	2004	Porous gold	1-octadecanethiol	11x	NR	180 nm	16 nm
Taborek[6]	2006	Porous gold	Helium isotherms	64x	52 cm^2	3.3 μm	52 nm
Taborek[5]	2007	Porous alumina	Vapor pressure	120x	75 cm^2	13 μm	108 nm
Bhargava[9]	2016	Sea urchin gold	Mercury vapor	5x	NR		
Milgie Taborek	2018	Porous gold	1-octadecanethiol	106x	140 cm^2	980 nm	10 nm
Milgie Taborek	2018	Porous gold	1-octadecanethiol	85x	119 cm^2	430 nm	5 nm

Table 6: The results of other porous QCM publications can be seen above and compared to ours. The author and reference number is listed along with the year it was published in. The method used to determine the sensitivity increase is also described along with the sensitivity increase, surface area, and thickness. The final column describes the thickness required to increase the sensitivity by a factor of one. We note our porous gold QCM have the largest surface area despite being thinner than most. We also find the greatest sensitivity increase per thickness added. This indicates our porous gold is the most efficient at increasing the sensitivity of the QCM.

3.11 Porous Gold SEM

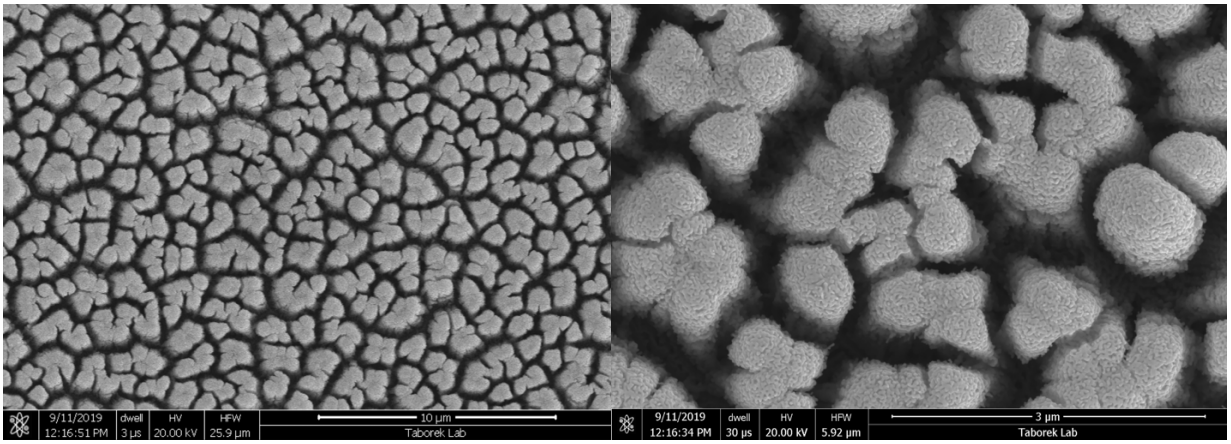

Figure 51: SEM images of our 31 atomic percent porous gold can be seen above. We note there are channels in a random array along with islands of gold. Images were taken on a FEI Magellan 400 SEM.

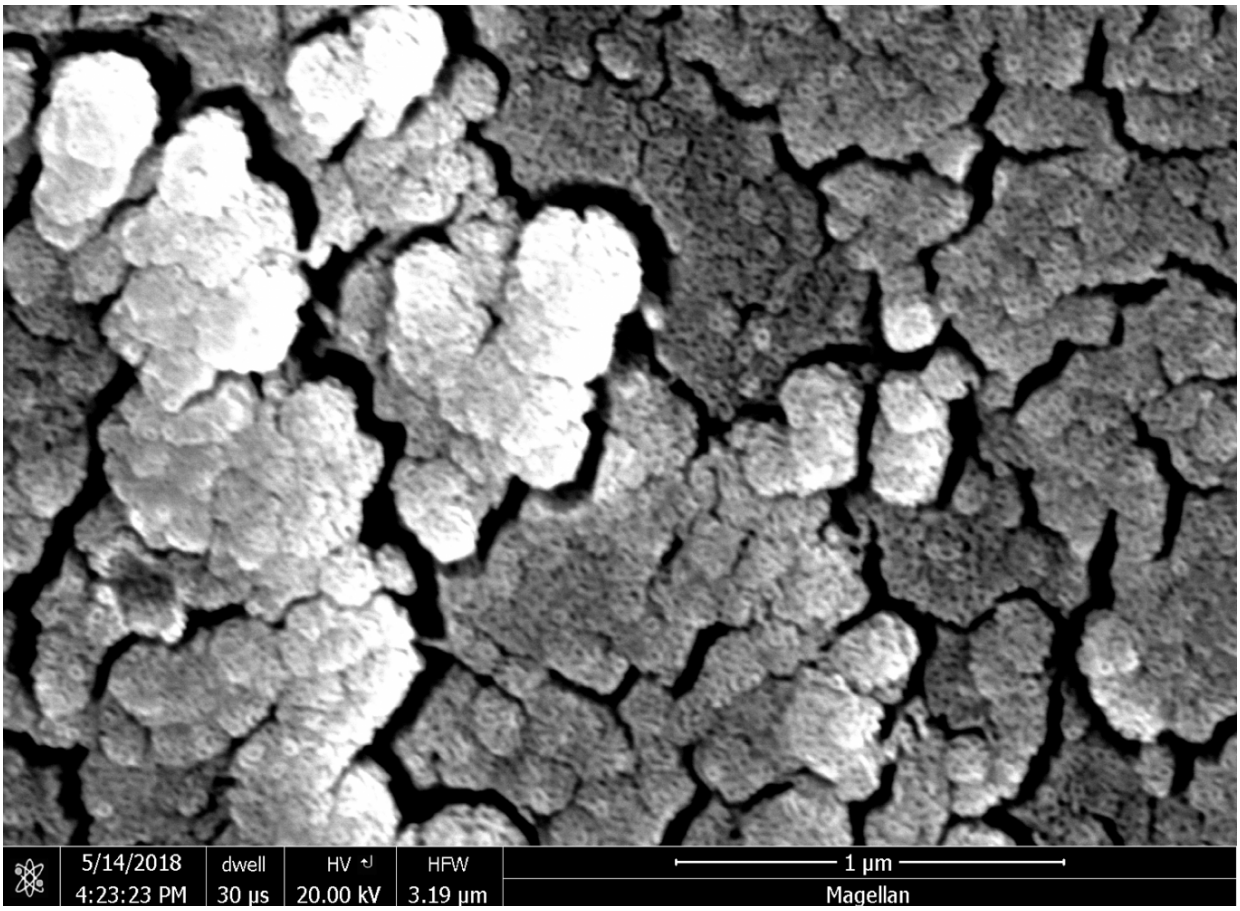

Figure 52: As we zoom in closer we see the channels are 50nm to 100 nm, and the islands look extremely porous.

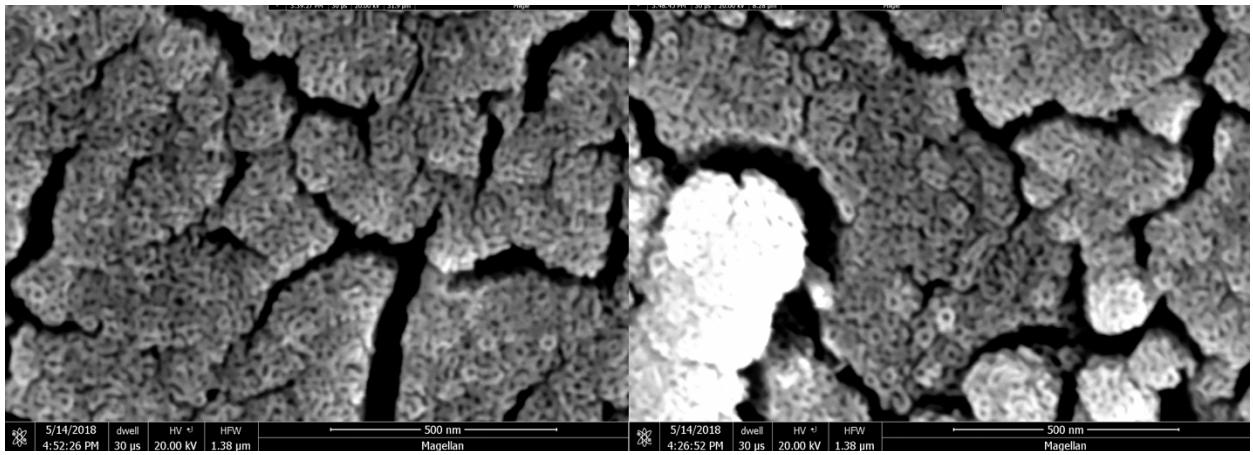

Figure 53: A closer look at the islands of gold show they are filled with tiny 10 nm diameter pores. These nano-pores drastically increase the surface area of the porous structure, and are not apparent on higher or lower concentrations of gold. At higher concentrations of gold these pores are filled in forming a more solid structure seen in Figure 47. At lower concentrations there is not enough material to form the small 10 nm pores.

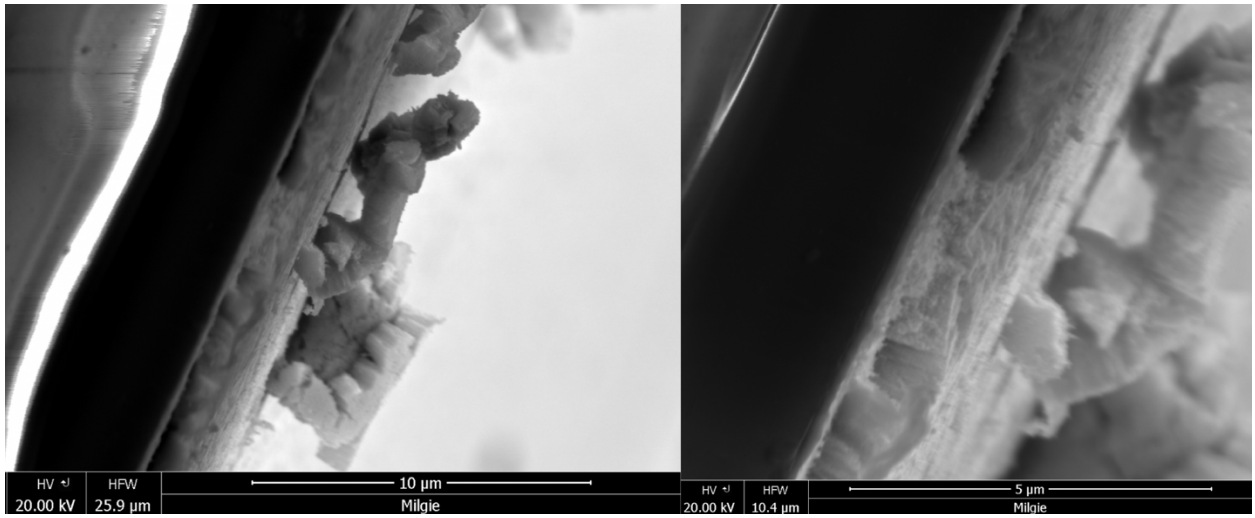

Figure 54: Near the edge of a porous gold QCM sacrificed for SEM imaging we see a profile view of our substrate on the sensor. The black area is the quartz of the QCM, with brighter areas indicating conducting gold. We note near the edge that was broken, part of the porous gold structure has lifted off the QCM and landed on a porous area. The SEM image shows that these porous gold structures of 31 atomic percent gold are rather durable. They remain intact when removed from a solid gold surface, and can be re-attached to the porous surface. This result also verified our QCM calculated thickness measurements showing the 980 nm substrate was indeed 1 µm thick.

3.12 Porous Gold: Ultra-Low Thiol Concentration Detection

Since our 430 nm porous gold had the greatest sensitivity increase per height added we used it to test the dependence on thiol concentration. The results shown below demonstrate the porous QCM can easily differentiate between micromolar and nanomolar concentrations. It further shows that due to the large increase in surface area of the porous QCM, most of the thiol in solution can be adsorbed onto the porous gold structure. When the thiol from the solution reaches an energetic equilibrium between adsorption and desorption, it causes the porous gold QCM to stabilize despite not being fully coated with thiol. This can be seen when the 0.5 μM concentration quickly levels off below.

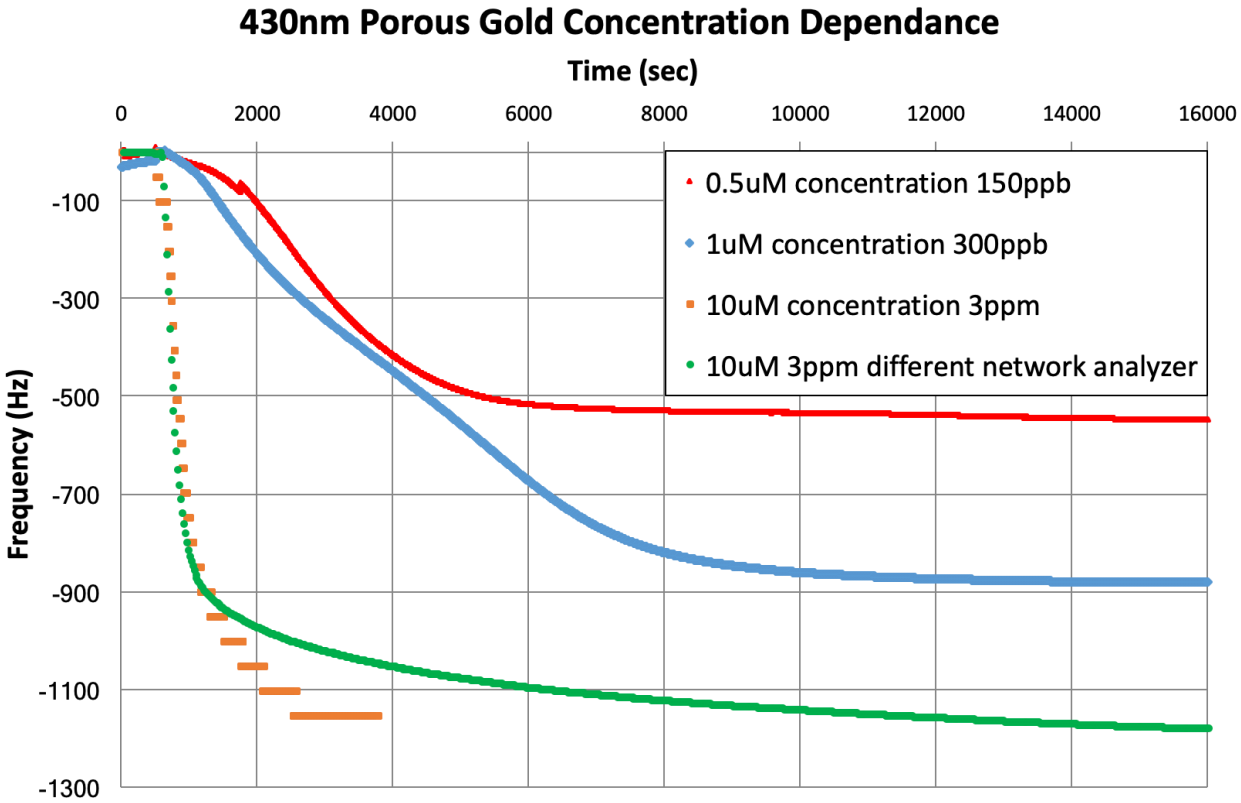

Figure 55: A concentration experiment of 1-octadecanethiol adsorption on our 430 nm porous gold can be seen above. It demonstrates the sensor is easily capable of differentiating between various concentrations of thiol. It further shows for small concentrations the majority of thiol in the solution can be adsorbed. At small concentrations the frequency of the QCM stabilizes despite the porous substrate not being fully saturated.

Since we have demonstrated our porous QCM can detect parts per billion (ppb) concentrations, we now show our experimental results for ultra-low concentrations of 1-octadecanethiol on our 430nm porous gold QCM. We find we can easily detect low concentrations of thiol in the 8 ppb range. We can also differentiate between higher concentrations in the ppb range. With 0.01 mM concentrations of thiol on a flat QCM there is enough thiol to coat a flat QCM 700 times. However, when using nano-molar concentrations it is possible to exhaust the thiol supply as seen below when the QCM frequency stabilizes without being fully coated.

In these low concentration experiments, an equilibrium is reached between adsorption and desorption before the porous structure can be fully coated. In fact, there is not enough thiol in the solution to fully coat the substrate due to its additional surface area. In our 8 ppb or 25 nM trails for example, there is only enough thiol to coat two flat QCMs, or add approximately 36 Hz of mass to the flat sensor. Our results show that each injection of thiol adds 25 Hz of mass to our porous QCM before an equilibrium is reached. When we add a higher concentration of thiol, we observe more mass being added to the sensor. In the experiment below we place our 430nm porous QCM into clean n-hexane and allow the frequency to stabilize. We then inject a small amount of thiol into the solution giving a total concentration of 25 nM. We allow the frequency of the QCM to stabilize with the thiol, and then repeat the experiment to confirm our adsorption. Since not all thiol is adsorbed in the first injection, the second iteration has slightly more thiol in the solution. This causes the rate of adsorption to be slightly faster than the first trial, and allows slightly more mass to be adsorbed before an equilibrium is reached. After this second equilibrium we then add a larger concentration of thiol to solution, this time we use 150 nM or 50 ppb. After this

larger concentration is added we observe the frequency drops faster, and more mass is added than in the first two trails. We display these results in the figures below.

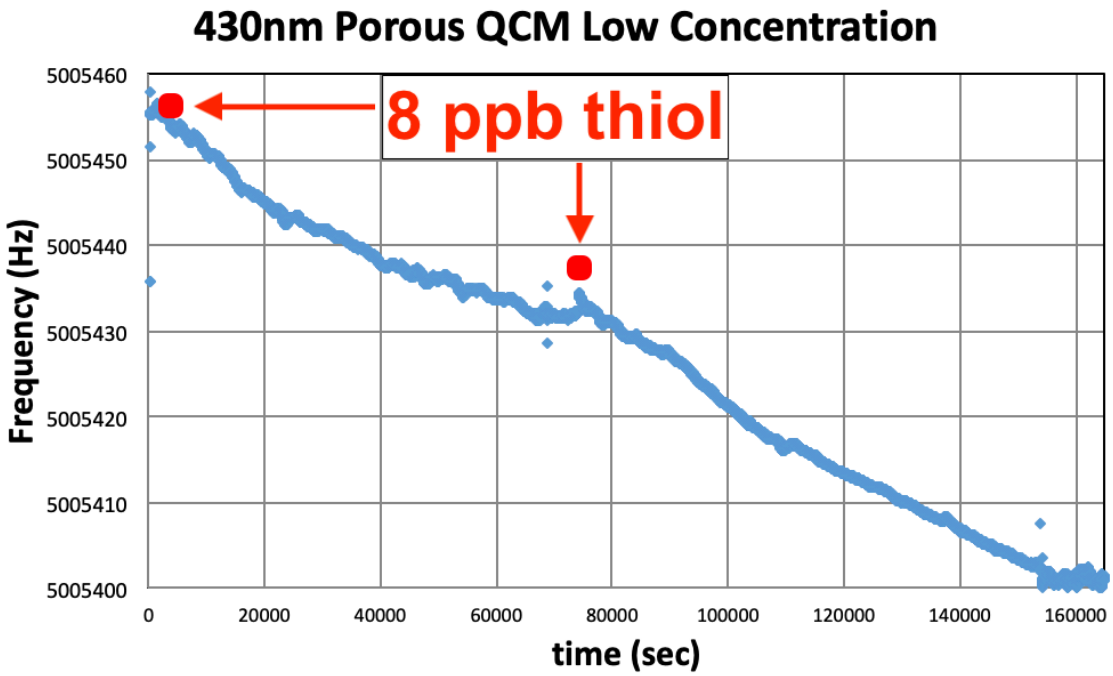

Figure 56: In the above figure we add a 25 nM or 8 ppb thiol concentration to our 430nm porous QCM. The first addition of thiol adds 25 Hz of mass to the sensor before an equilibrium is reached. In the second injection, since more thiol is present in the solution, 32 Hz of thiol is adsorbed to the QCM before an equilibrium between adsorption and desorption is found and the frequency stabilizes. The second addition of thiol also has a slightly faster rate of adsorption due to the additional thiol present from the thiol not adsorbed in the first addition.

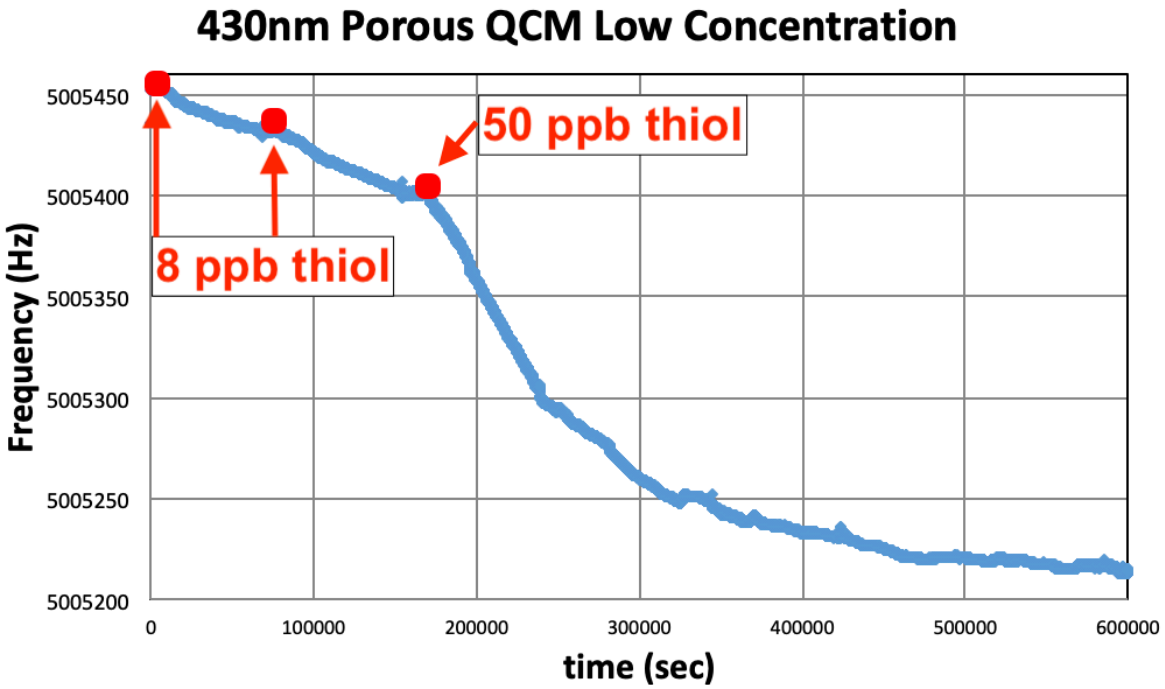

Figure 57: After adding an 8ppb concentration of thiol to our porous QCM twice, we then add a 150 nM or 50 ppb concentration. This higher concentration adds 190 Hz of mass to the QCM before the frequency equalizes.

3.13 Flat vs 430 nm QCM Liquid Loading & Summary

Now that we have described our 430 nm thick ideal 31 atomic percent porous gold QCM and demonstrated its sensitivity and efficiency we compare the substrate to flat gold. Here we are interested in the amplitude plots of a flat QCM and the porous QCM in liquids. In the theory section we demonstrated that adding thiol to a flat QCM adds a barely detectable dissipation, whereas thiol on a porous sample adds a larger dissipation. We now demonstrate the dissipation and frequency change caused by liquids in our 430 nm thick substrate. We first present typical results for a flat QCM in air, hexane and water. We then present our results for our 430 nm sample using the same method. Finally, we compare the two to determine the difference a porous substrate creates in liquids.

From the theory section we expect a larger frequency change from the 430 nm sample in liquids compared to a flat QCM. This larger frequency change arises from the additional liquid trapped in the pores of the substrate. However, for dissipation, we expect there to be no notable difference between the porous and flat sample. Dissipation in liquids arises from the penetration depth. Since the QCM is forced to drag a thick layer of liquid due to the non-slip boundary condition, the resonance is noticeably damped. However, when liquid is inside the small 10 nm pores of the substrate, it is not dragged to the penetration depth. Due to the non-slip condition at the surface, the liquid acts very much like solid mass loading. Thus we expect the dissipation for a liquid in a porous sample to act exactly like a flat QCM. We present these results below for our flat and 430 nm thick porous QCM.

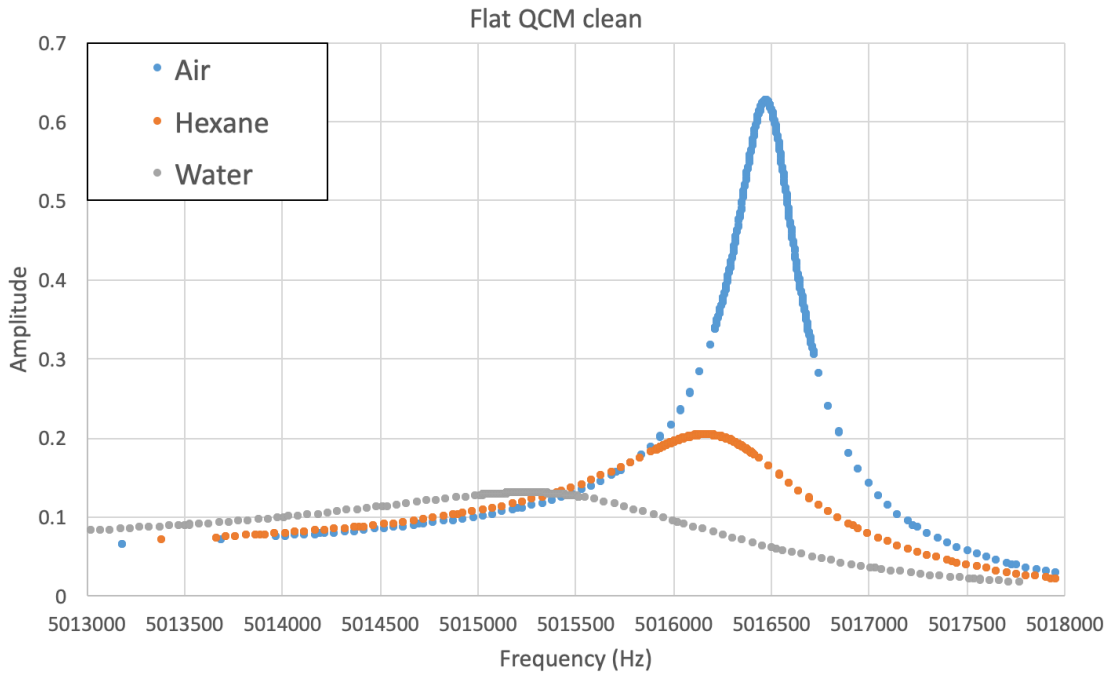

Figure 58: The amplitude plot of a flat QCM in air, n-hexane, and water is displayed above. The liquid loading decreases the resonant frequency and the amplitude of resonance. This decrease in both frequency and amplitude is dependent on the density and viscosity of the fluid. Since water has both a higher density and viscosity than n-hexane the decrease in frequency and amplitude is greater for water.

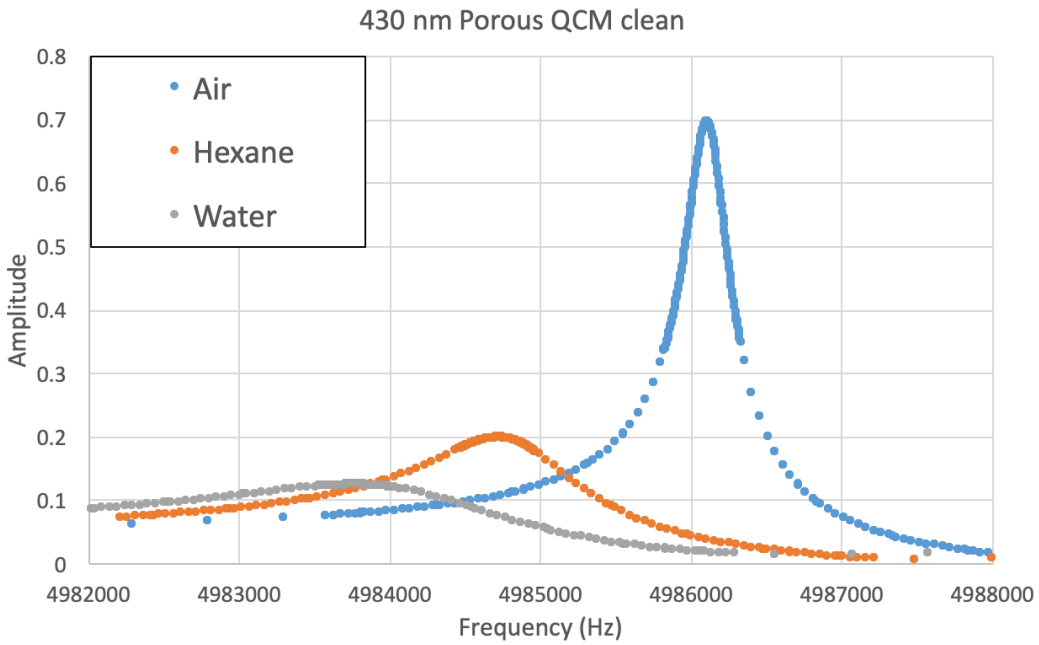

Figure 59: The amplitude plot of a 430nm porous QCM in air, n-hexane, and water is displayed above. We observe a similar trend in amplitude change compared to the flat QCM, but larger frequency shift due to the porous substrate.

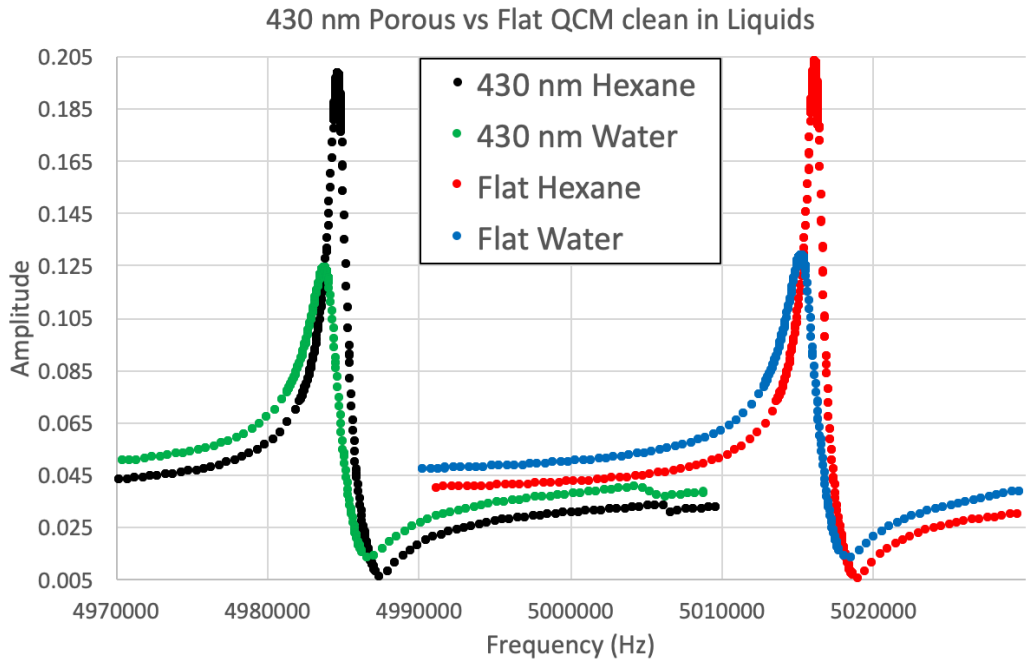

Figure 60: We now compare the 430 porous QCM with a flat QCM in liquids. The frequency shift is clearly larger due to the solid-like liquid loading in the 10nm pores of the porous QCM. We observe a slightly larger decrease in amplitude in the porous QCM. The Flat QCM has a peak amplitude of 0.203, whereas the 430nm substrate has a max amplitude of 0.198 in n-hexane. In water we observe the flat QCM has a peak amplitude of 0.129, whereas the porous substrate max amplitude is 0.124. In both examples we see a change of amplitude due to liquid loading of approximately 0.005.

The results above demonstrate our porous QCM agrees well with the theory for its use in liquids. We observe a greater change in frequency due to the additional liquid trapped in the pores of the QCM. However, this additional liquid has very little influence on the dissipation of the porous QCM. The liquid inside the small 10 nm pores and channels act like a rigid and solid mass. These results indicate liquid loading does not impose a limitation on the porous QCM sensitivity or height compared to a flat QCM. Thus far the most serious limitations for increasing the sensitivity of the porous QCM is the resistance added to the QCM from a thiol coating, and the intrinsic scaling law of the base sensitivity of the QCM being proportional to $f0^2$ described in figure 5yep0. Our 430 nm porous gold QCM was capable of adding 85 times more thiol than a flat QCM using a 0.01 mM concentration of thiol. We now turn our attention to larger porous gold substrates that allow us to increase the sensitivity 1000 times beyond that of a flat QCM.

3.14 Larger Porous Gold Substrates

We have now thoroughly explored the properties of our 430 nm porous gold; going through fabrication, characterization, baseline thiol measurements compared to other publications, ultra-low 8 ppb concentration trials, and confirmed our results are consistent with our model of the QCM. Our results demonstrate we have found an 85x sensitivity increase in our 430 nm porous sample, meaning every 50 nm of thickness we increase the sensitivity of the QCM by a factor of 10. They further demonstrate we have fabricated the most efficient surface modified QCM ever fabricated in terms of sensitivity increase per unit thickness [5]. These findings indicate it is possible to continue to increase the sensitivity of the porous gold QCM by increasing the thickness of the substrate. We now present our results with producing larger porous gold substrates.

To produce thicker substrates, the same fabrication method described above was used. The cathode of the sputter system is water cooled, but the entire system nonetheless heats up throughout the sputtering process. When the substrate becomes too hot, there are adhesion issues between the flat gold surface and sputtered alloy. To account for the additional heat build-up from longer sputter times, the target is placed slightly further away from the cathode. An additional distance of 0.5" away, for a total throw distance of 3" was found to be suitable for sputter times up to around 1 hour. The additional distance between the cathode and substrate produced a typical sputter rate of 0.8 $\frac{\text{nm}}{\text{s}}$.

Since silver is the primary sputter target with gold pieces added to it, over the course of an hour long sputter, the gold is depleted at a faster rate. This causes the ratio of gold and silver to slightly change over the course of sputtering. Therefore, the first layers added during sputtering have a slightly higher concentration of gold than the final layers sputtered. Over an hour long sputter we find the change in atomic ratio is roughly 0.3 atomic percent. For example, a QCM sputtered with a 30 atomic percent gold ratio actually has 30.15 atomic percent gold at the bottom surface, and 29.85 atomic percent at the top surface. This property may actually be beneficial to the durability of the porous substrate by having a stronger pore structure where it binds to the solid gold surface.

Of the many porous substrates we fabricated we now bring our attention to two in particular. The first of which is a 2.56 μm thick porous substrate with a ratio of 29.7 atomic percent gold. This substrate has 6 percent less gold than our 430 nm sample, so we expect it to be less efficient. Nonetheless, due to having nearly 6 times the thickness, it adsorbs much more thiol than the thinner porous sample. We compare the results of our prior 75 nm, 430 nm, and 980 nm thick substrates to this larger sample. Since we have already

investigated the effects of ultra-low concentration of thiol on our 430 nm sensor, we instead test higher concentrations with this thicker substrate. We later use this 2.56 μm substrate for desorption and kinetics experiments.

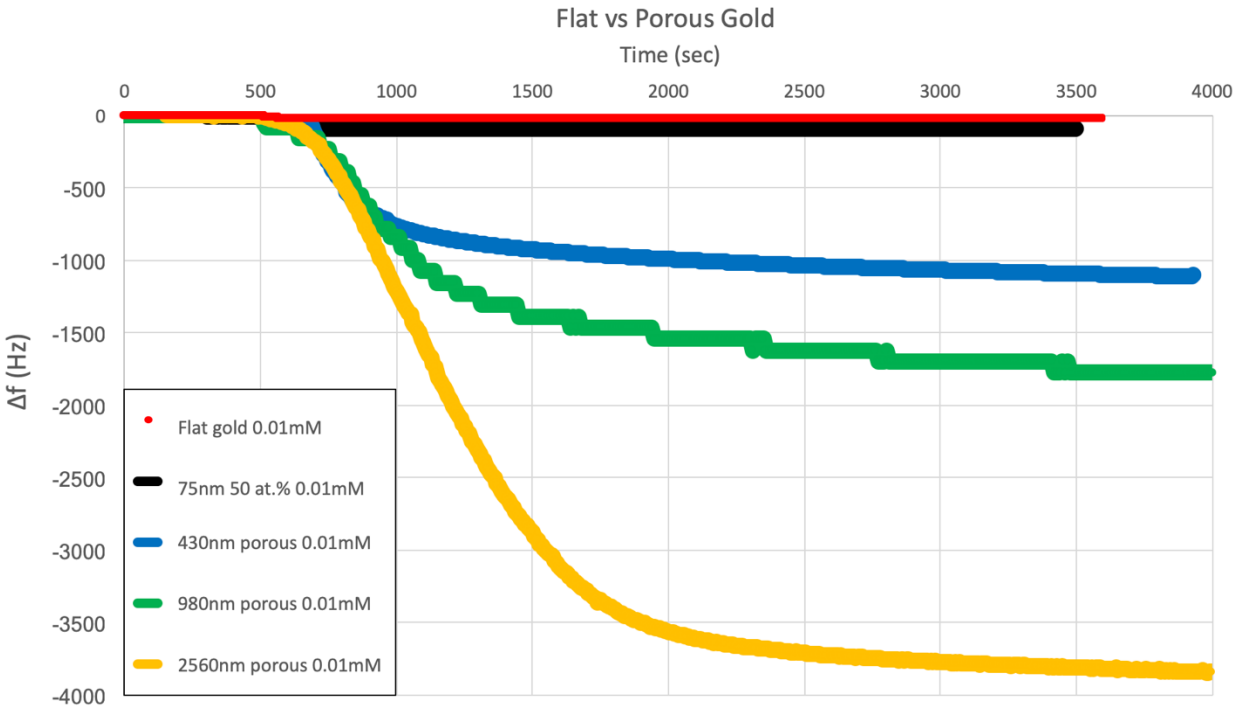

Figure 61: We present the results of our 2.56 μm 29.7 atomic percent gold porous substrate above in yellow, and compare it to our prior results. The frequency is stable until at 500 seconds thiol is added to the solution. A final concentration of 0.01 mM of thiol in n-hexane is used for all samples. We observe all the porous samples have a similar binding rate of thiol for the first 500 seconds. As the 430 nm and 980 nm substrates come to equilibrium the adsorption of thiol slows down and the frequency change flattens out.

The above results demonstrate that our thicker porous QCM is capable of adsorbing more thiol than our 430 nm substrate by a factor of 2.7. Using a concentration of 0.01 mM it is found to adsorb 226 times more thiol than a flat QCM before forming an equilibrium. The quantity of thiol used in the experiment is enough to coat a flat QCM 700 times. Below we present results for adding higher concentrations of thiol using the same experimental method.

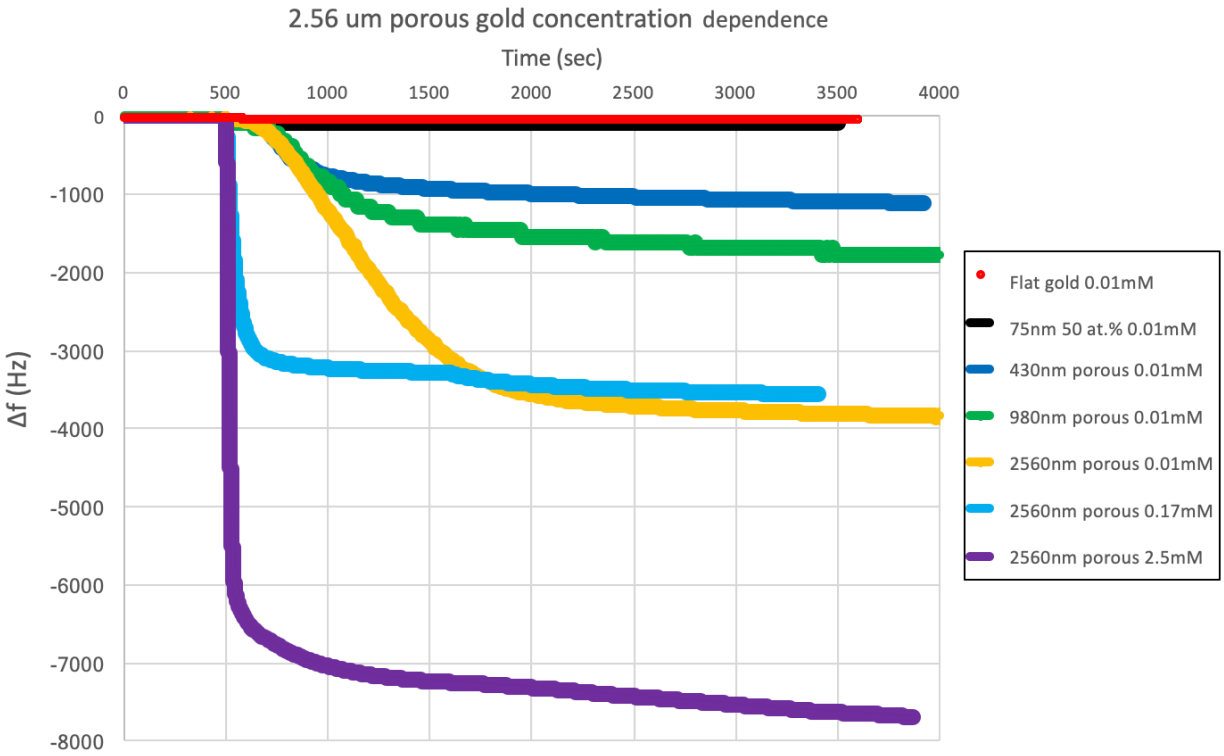

Figure 62: In the above plot we include our results with higher concentrations of thiol used on our 2.56 μm porous substrate. We find the 0.01 mM concentration of thiol is not fully saturating the porous sample. When comparing 0.01 mM and 0.17 mM concentrations we observe the thiol is coated at a much faster. For the 0.17 mM concentration the QCM is nearly fully coated in less than 1 minute, whereas the 0.01 mM concentration takes nearly 15 times longer to coat. When we compare these results to the 2.5 mM concentration, we find the QCM adsorbs nearly twice as much thiol as the lower concentration trials. We compare these 2.56 μm results with our previous results of with various substrates for reference.

The above and prior results demonstrate a clear feature of the porous QCM adsorption. There is first a fast adsorption period, where the porous QCM is rapidly coated with thiol. There is then a secondary period where the thiol is added at a much slower rate. This effect is known for thiols and was previously described by Schlenoff et. al. [42]. In the first stage the thiol binds rapidly to the gold surface without much order. In the second stage the thiol is rearranged more efficiently, through the process of self-exchange and desorption to fully coat the substrate. The full effects of this self-exchange are displayed below in a 3-day adsorption of thiol onto the 2.56 μm QCM at high concentration.

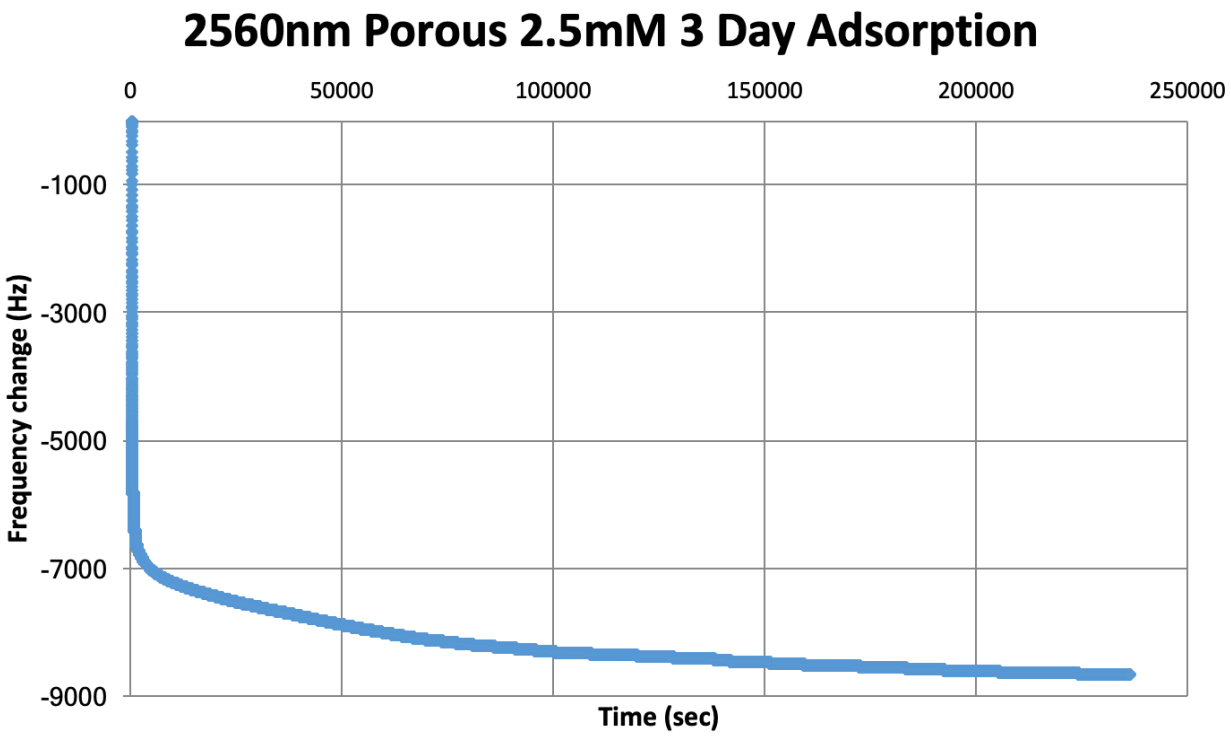

Figure 63: The long term self-exchange and adsorption of thiol onto the 2.56 μm porous QCM is displayed above. We see a rapid adsorption of thiol in the first hour, followed by a slow process of self-exchange and adsorption to fully coat the porous media over the course of a few days.

Thus far on the 430 nm thick substrate we observed a clear dependence of concentration for low and ultra-low concentrations of thiol down to 25 nM or 8ppb. For the 2.56 μm substrate we demonstrated a clear concentration dependence for higher concentrations up to 2.5 mM. This concentration dependence effects both the rate of adsorption, as well as the quantity of mass added to the sensor. The range of these concentrations is huge, the 2.5 mM concentration has 100,000 times more thiol than the 25 nM concentration. The frequency change from the low concentration trial was 25 Hz, similar to the frequency change of a flat QCM in a 0.01 mM solution, however the mass took much longer to adsorb. The 0.01 mM concentration is interesting to consider when comparing the quantity of thiol and the number of adsorption sites available on porous

substrates. Using the 2.5 mM concentration the 2.56 μm substrate adsorbed nearly 450 times more thiol than a flat QCM can adsorb. The thiol solution with 0.01 mM concentration has enough thiol to coat a flat QCM 700 times. This means the quantity of thiol in the solution is similar to the number of adsorption sites on the porous substrate. We now present results of our largest QCM used for thiol adsorption.

The second large porous substrate we fabricated has a thickness of 3.0 μm and an atomic ratio of 32.7 percent gold. This substrate has slightly more gold than the ideal 31 atomic percent 430 nm substrate previously described. However, it provides a good opportunity to determine the efficiency of porous gold with slightly more gold than the ideal 31 atomic percent. This can also be compared to the 2.56 μm 29.7 atomic percent gold substrate that has slightly less gold than the ideal 31 atomic percent. We present these results in a similar fashion, by comparing them to earlier described substrates and using varying concentrations. The 3.0 μm porous substrate is the most sensitive of all the porous QCM we have fabricated, adsorbing 1000 times more thiol than a flat QCM. As will be shown, we further argue that this 1000 times more sensitive substrate is the maximum sensitivity increase allowable on a surface modified QCM.

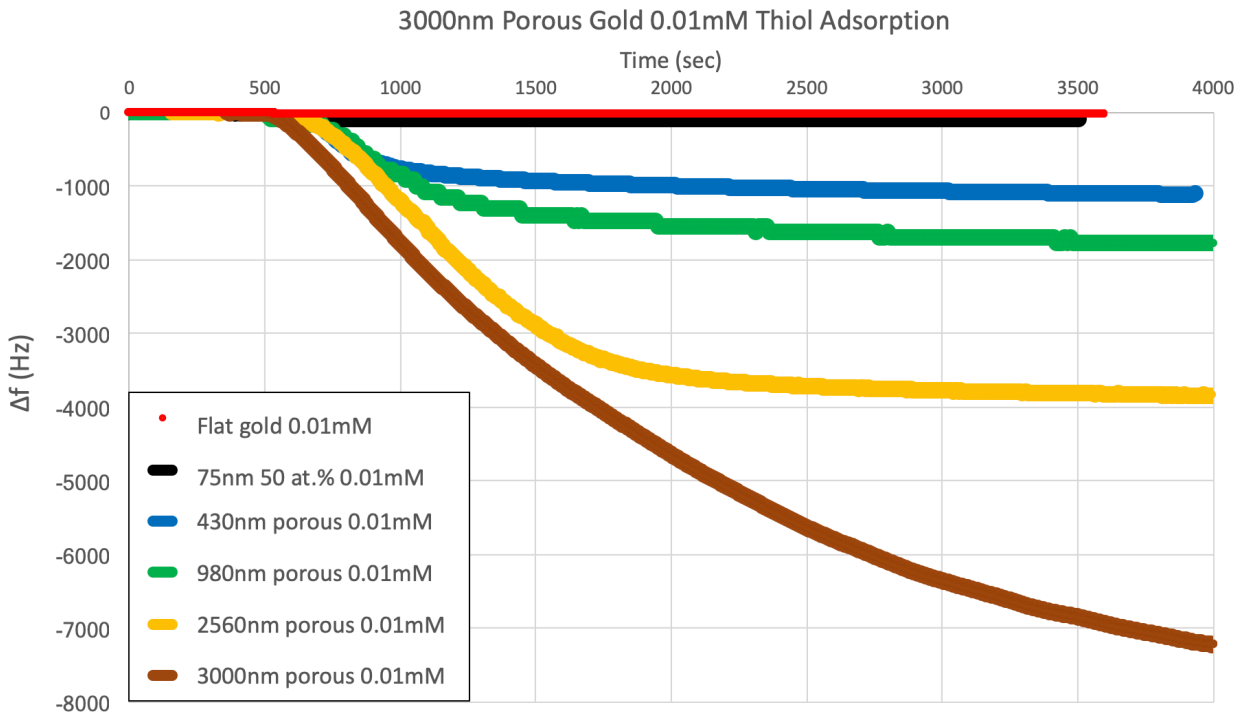

Figure 64: The adsorption results for our 3000 nm 32.7 atomic percent porous gold QCM are displayed above in brown and compared with flat and our other porous samples. For all trials above a thiol concentration of 0.01 mM was used. The initial rate of thiol adsorption for all four porous substrates is similar.

The 3000 nm substrate is 7 times thicker than the 430 nm sample, and adds 5 times more thiol than the 430 nm substrate. The additional gold causes the larger porous sample to be less efficient than the ideal 31 atomic percent gold. In the 0.01 mM thiol experiment the 3000 nm substrate adsorbs 431 times the amount of thiol a flat QCM could adsorb. In the 0.01 mM solution there exists enough thiol to coat a flat QCM 700 times. This means the 3000 nm porous substrate adsorbs 62% of the thiol contained in the solution before forming an equilibrium between adsorption, desorption, and self-exchange. In most QCM experiments there typically exists thousands of times more thiol in the solution than will be adsorbed onto the QCM surface. We tested higher concentrations on the 3000 nm substrate to determine if the sample was fully saturated at 8000 Hz of thiol, or still had available

binding sites. The results below further demonstrate the concentration dependence on both the rate of adsorption and the total amount of thiol adsorbed.

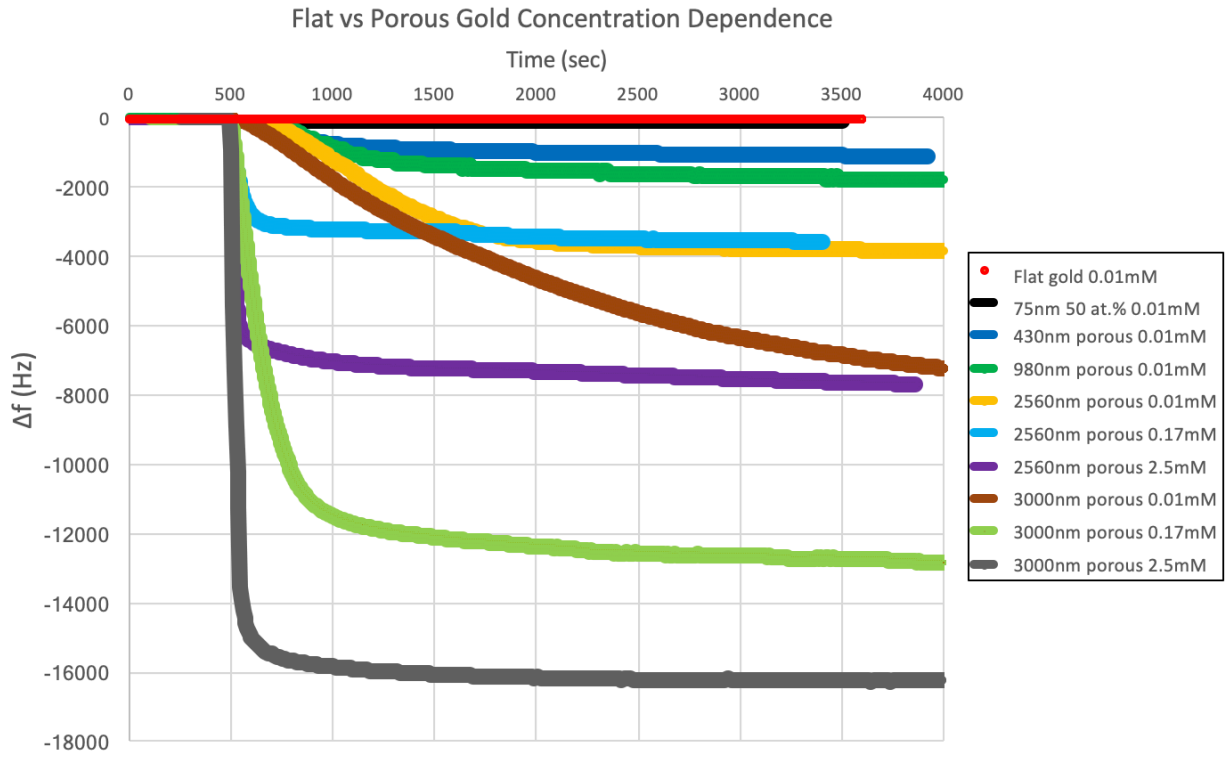

Figure 65: Thiol adsorption onto our porous gold QCM of varying thickness is displayed above. Thiol concentration ranges from 0.01 mM to 2.5 mM. We note clear dependence of adsorption rate and frequency change based on thiol concentration. Thicker porous samples adsorb more thiol than thinner substrates, and higher concentration of thiol adsorb much more rapidly.

We tested higher concentrations of thiol adsorption onto our 3000 nm porous QCM but found increasing the concentration 100 times beyond the plot above to 0.25 M provided no additional adsorption. Thus our 3000 nm porous substrate can be fully coated with thiol at 2.5 mM concentrations of thiol. The 2.5 mM solution contains enough thiol to coat a flat QCM 175,000 times. We find our 3000 nm sample can adsorb 1044 times more thiol than a flat QCM with a 2.5 mM thiol concentration. It is interesting to note from the above plot that the 0.17 mM thiol concentration, containing enough thiol to coat 12,000 flat QCM is unable to fully saturate the 3000 nm porous sample. This means having 12 times

more thiol in solution than is capable of being adsorbed will not bind thiol to all available sites. However, adding 170 times more thiol than adsorption sites allows for full saturation of the substrate. We compare the concentration dependence of a flat QCM below.

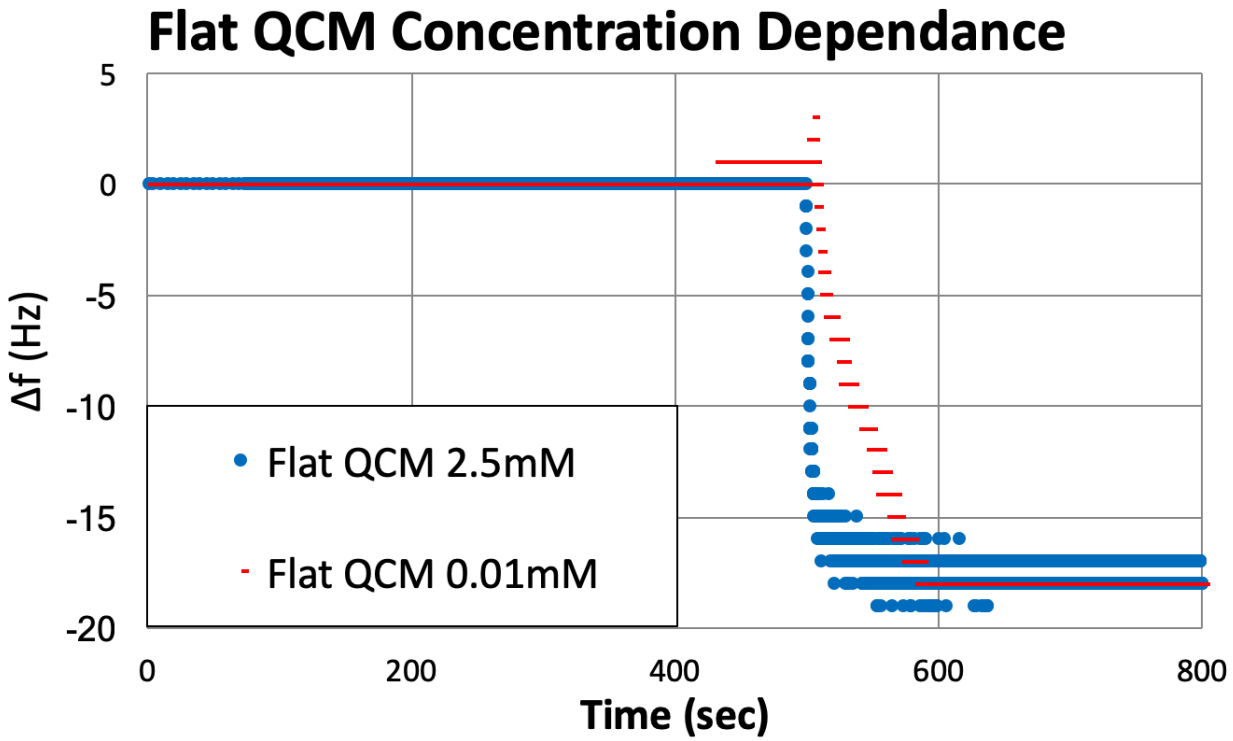

Figure 66: The concentration dependence of a flat QCM is displayed above. We find a flat QCM adsorbs the same amount of thiol for both 0.01 mM and 2.5 mM concentrations. There is a concentration dependence on the rate of adsorption as expected.

A flat QCM shows no concentration dependence for the surface coverage of thiol. Both 0.01 mM and 2.5 mM concentrations produce a surface coverage of 320 $\frac{\text{ng}}{cm2}$. The higher concentration of thiol does change the adsorption kinetics, causing the QCM to form a monolayer faster than the lower concentration. The above results demonstrate we have fabricated a porous gold QCM that can adsorb more than 1000 times the thiol than a flat QCM. To achieve 1000 times adsorption required a porous gold substrate with a thickness of 3000 nm. To perform the experiment a concentration of 2.5 mM is needed, as lower concentrations such as 0.01 mM do not contain enough thiol to fully coat the QCM. We will

now present the amplitude plots of the 3000 nm porous QCM clean in hexane verses the amplitude of it coated with various amounts of thiol. These results will demonstrate the limit of thiol adsorption on a surface modified QCM is a factor of 1000.

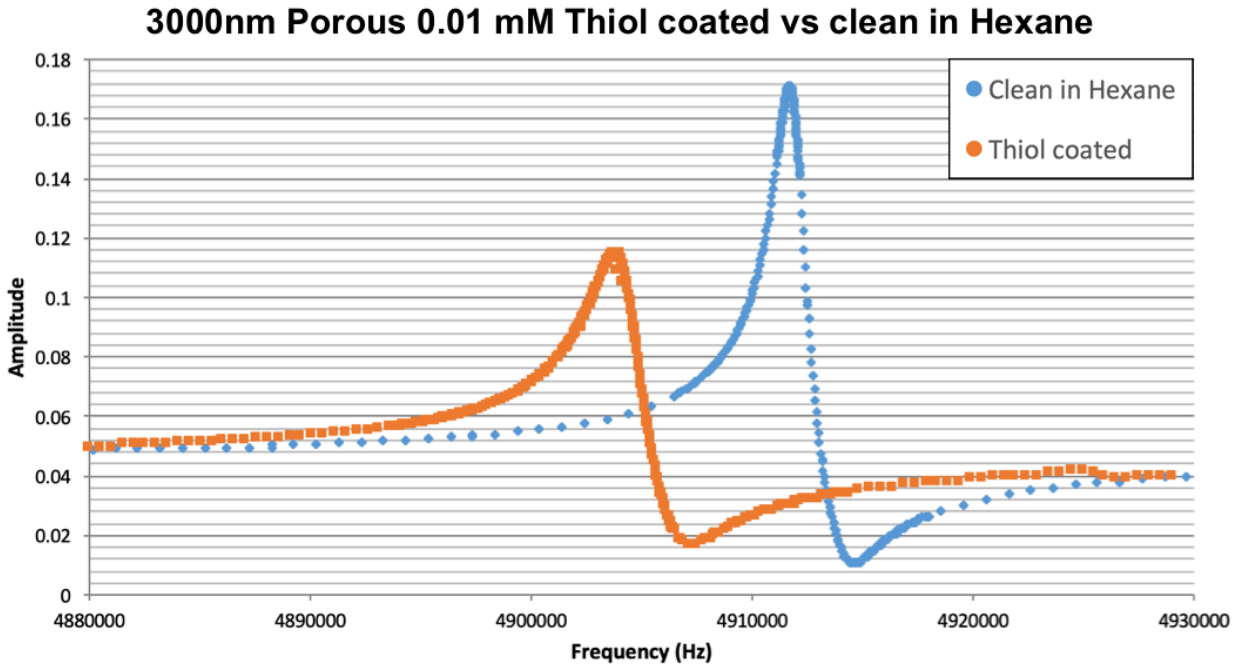

Figure 67: An amplitude plot of the 3000 nm porous gold QCM clean in hexane and coated with thiol using a 0.01 mM concentration is displayed above. During the experiment the QCM frequency decreases 7800 Hz after being coated with thiol and stabilizes. This frequency change is the equivalent of coating a flat QCM with thiol 440 times. With this loading and concentration there is a noticeable change in amplitude due to thiol loading. The change in amplitude due to thiol adsorption is 0.06 or a 35% decrease in peak amplitude from its clean state.

The 1 μm porous QCM previously discussed had a decrease in amplitude of 12% due to thiol coating when compared to the clean state in hexane. This larger 3 μm porous QCM demonstrates as additional thiol is added, we observe a larger decrease in amplitude. Since the 3 μm substrate observed a 35% decrease in amplitude, a linear relationship between dissipation due to thiol loading and thickness of the substrate is apparent. When we use a higher concentration of thiol, as is displayed below, we achieve much more mass loading. This additional thiol loading greatly increases dissipation. The 0.01 mM solution added

7800 Hz of thiol, whereas the 2.5 mM solution below adds more than 18,000 Hz of thiol. The additional thiol increases dissipation from 35% at 0.01 mM concentrations, to 70% at 2.5 mM when the 3000 nm substrate is fully loaded with thiol as seen below.

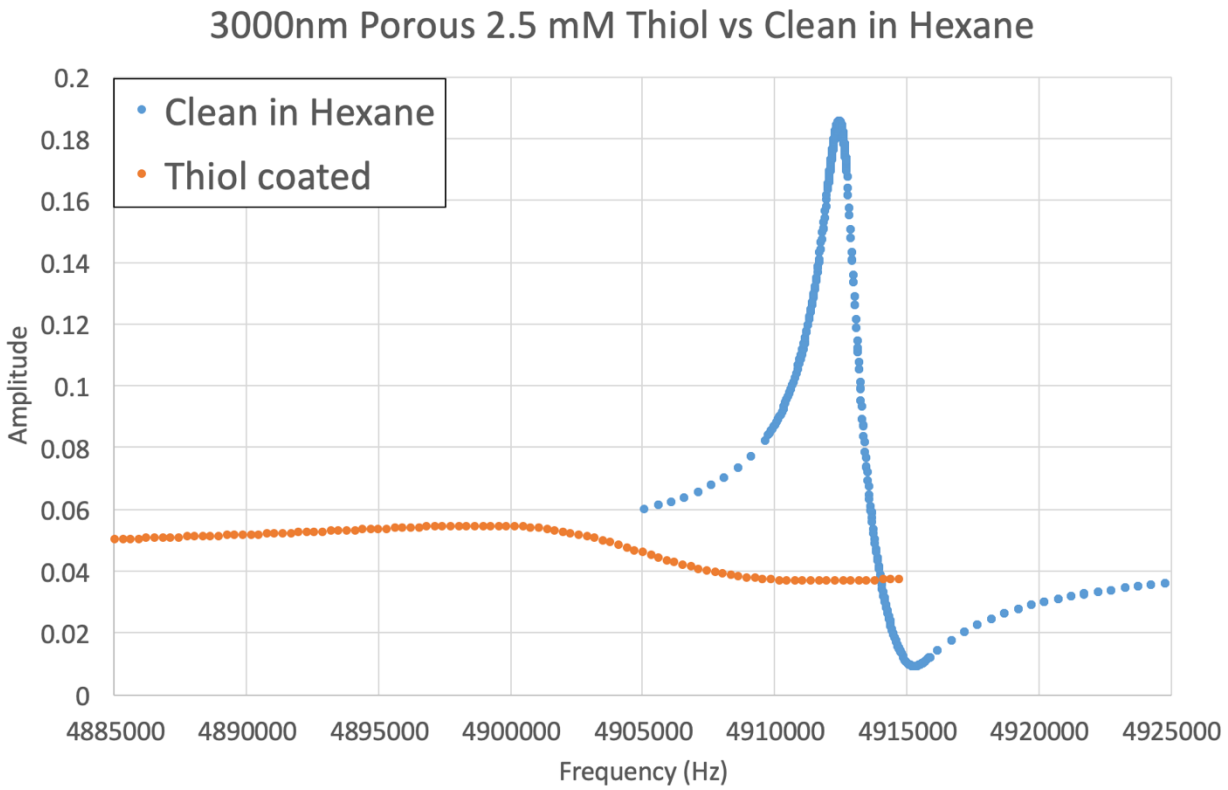

Figure 68: An amplitude plot of the 3000 nm porous QCM in clean hexane and fully coated with thiol in 2.5mM solution is displayed above. The amplitude of resonance is greatly damped after adsorbing 18,000 Hz of thiol to the gold surface. We observe a 70% decrease in amplitude due to thiol loading when compared to the clean surface in hexane.

The drastic change in amplitude displayed above does not happen instantaneously, but rather the amplitude decreases as the porous structure is binding with thiol. The change in amplitude is directly related to the change in frequency. We observe the amplitude rapidly decreases at first, and then slowly decreases as additional thiol is added the to the substrate. In the plots below we display the evolution of the amplitude in time. The plots begin with the clean 3000 nm QCM in hexane, and then demonstrate the change in amplitude as it is coated with thiol.

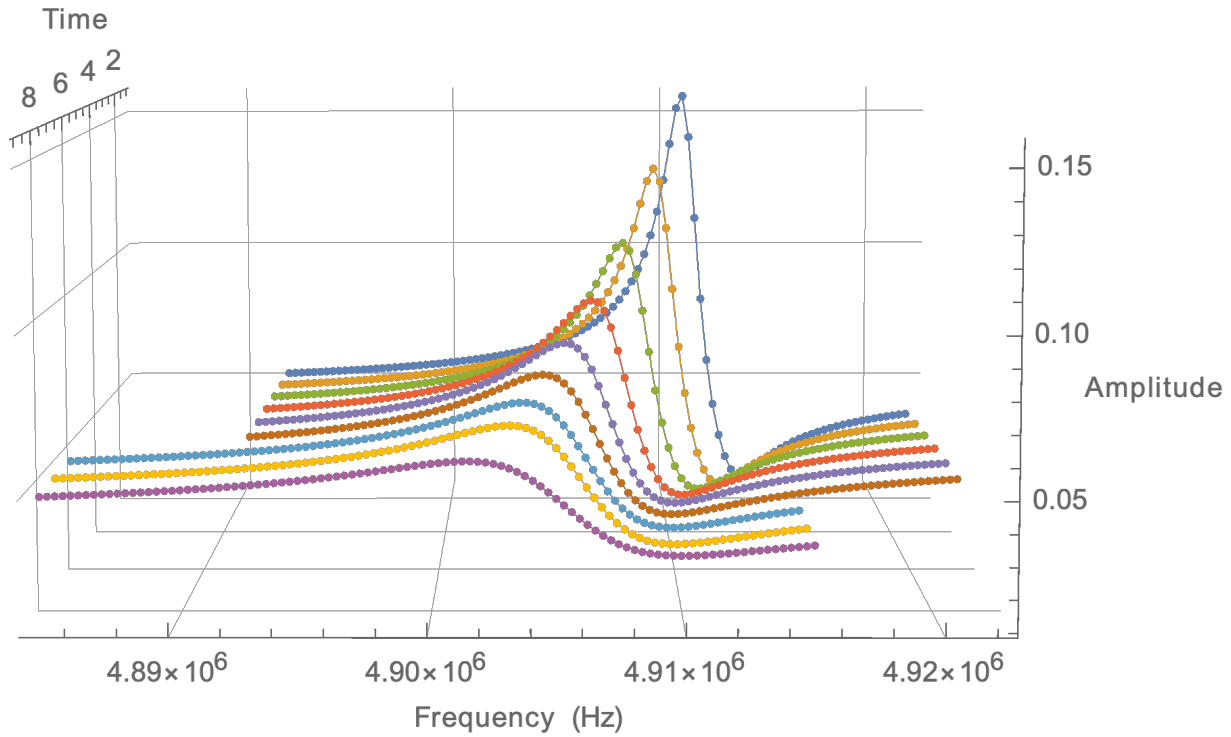

Figure 69: A 3D amplitude plot of the 3000 nm QCM being coated with thiol is displayed above. The first amplitude in blue is the QCM clean in hexane. After a 2.5 mM concentration of thiol is added to the solution, the amplitude decreases with time.

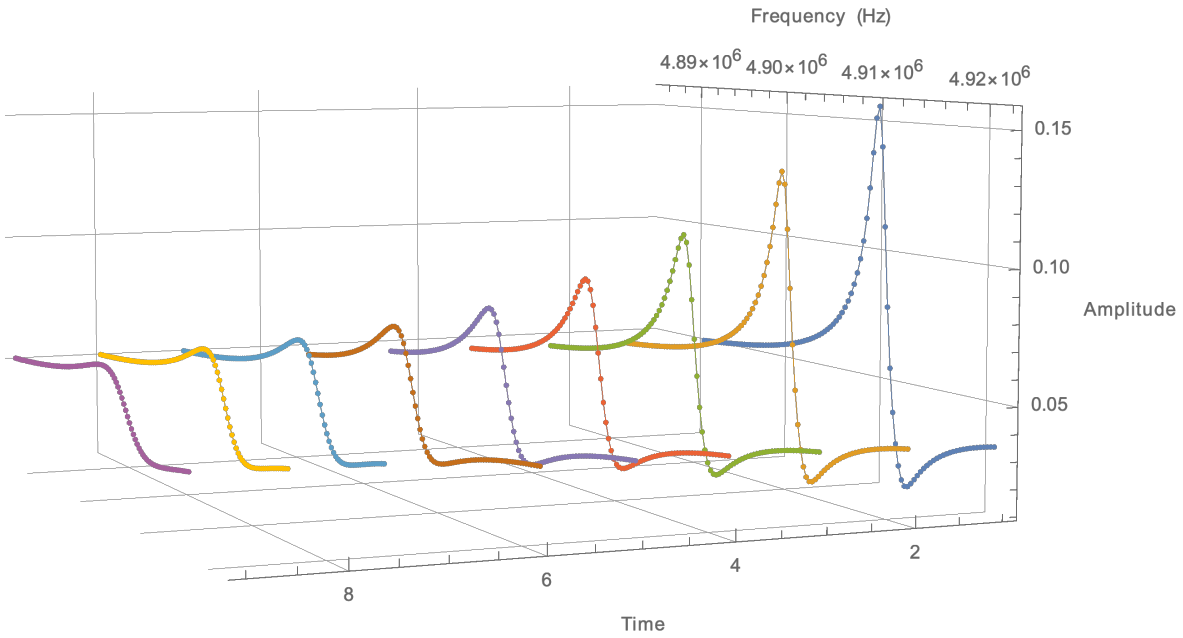

Figure 70: An alternate view of the evolution of the amplitude plot in time with thiol adsorption is displayed above. The amplitude rapidly decreases at first, and then slowly decreases as the porous QCM fully saturates with thiol.

The massive dissipation caused by adsorbing so much thiol onto the 3000 nm substrate is a major limitation to surface modified QCM. The dissipation due to the solid porous gold structure is minimal. However, the dissipation of thiol does create a limit to the possible sensitivity increase available to QCM used in liquids. We have fabricated larger porous substrates however the dissipation caused by thiol loading beyond a factor of 1000 creates a very poor amplitude. These results are exemplified in measuring the amplitude plot of the 3000 nm porous QCM in air, n-hexane, and water. We finalize the characterization of our 3000 nm porous gold QCM by performing the water-glycerol experiment previously described and displayed in figures 14 and 15.

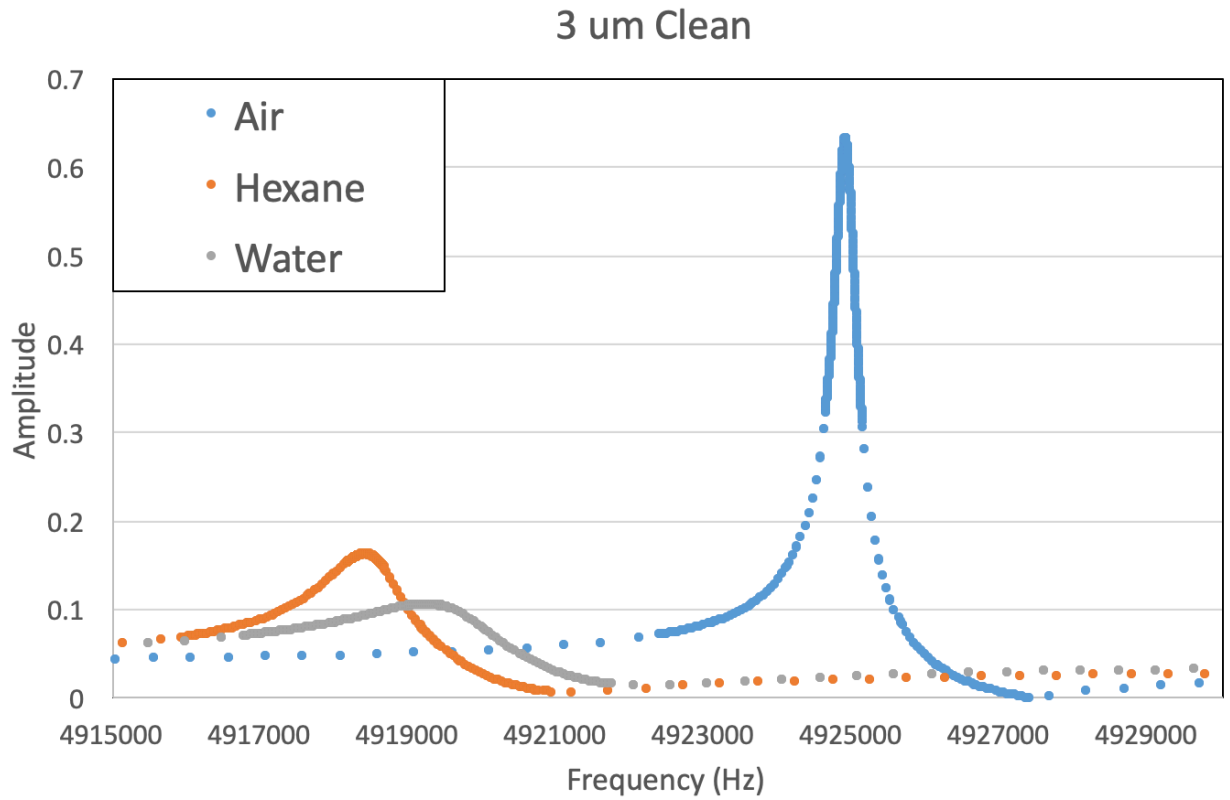

Figure 71: An amplitude plot of the 3000 nm porous gold QCM in air, n-hexane, and water is displayed above. Unlike the flat and former 430 nm porous QCM amplitude plots, water has a greater dissipation, yet smaller frequency change compared to n-hexane. This indicates we have reached the limit of resistive loading on the QCM, and the frequency response of the QCM can no longer respond accurately to the additional mass added.

The dissipation of the QCM due to the density and viscosity of a liquid is well described by the modified Butterworth-Van-Dyke equation previously described in equation 14. It shows the change in resistance is proportional to the viscoelastic properties of the liquid as $\Delta R \sim \sqrt{\eta_L \rho_L}$. To perform this experiment, we placed a clean flat and the 3000 nm porous QCM into water and measured the frequency and resistance of the oscillator. We then added various amounts of glycerol into the water while stirred to change the density and viscosity of the fluid. As is shown in the figure below, we find both the flat and 3000 nm QCM both follow the theory of this equation exceedingly well. The 3000 nm porous QCM has on average a 13% increase in dissipation compared to the flat QCM. This additional dissipation is due to the additional mass from the porous structure and the additional liquid inside the substrate.

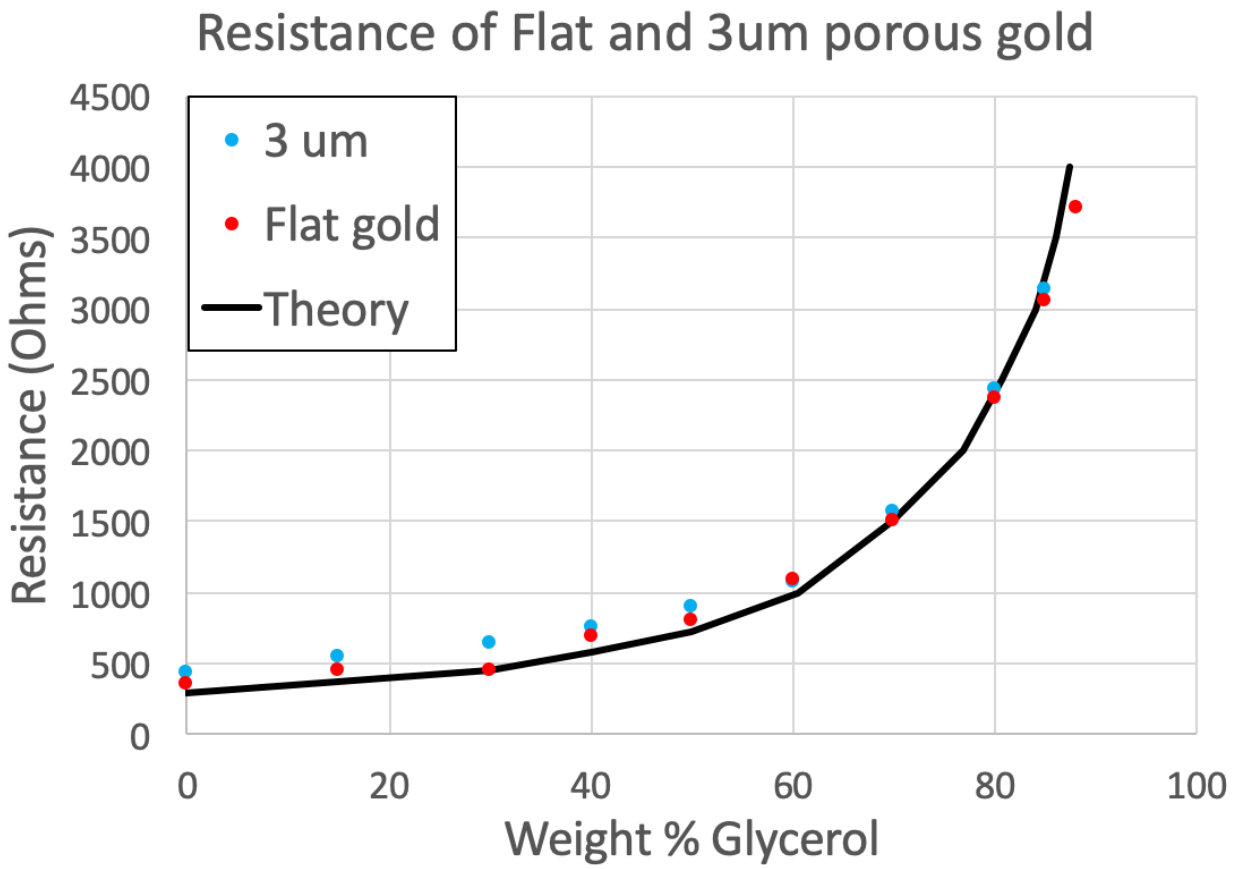

Figure 72: The resistance of the 3000 nm porous substrate and a flat QCM are compared above to the modified Butterworth-Van-Dyke equation as described in equation 14. We test the dependence of the resistance on the density and viscosity of the fluid it is immersed in. The change in resistance is proportional to the square root of the density and viscosity of the liquid. Both the flat and porous QCM agree remarkably well with theory. The porous QCM has an average of 13% additional dissipation over the entire curve and does not diverge from the flat data.

The change in frequency due to liquid loading is well described by the Kanazawa and Gordon equation as described in equation 11. This equation describes the frequency change due to liquid loading is dependent on the viscoelastic properties of the liquid as $\Delta f \sim \sqrt{\eta_L \rho_L}$. We have already discussed that adding solid mass to the QCM decreases the frequency without increasing the resistance. Whereas liquid loading decreases the frequency while increasing the resistance. The liquid loading for a flat QCM is dependent on the viscoelastic properties of the liquid causing the QCM to sheer a finite volume of liquid

with its motion to the penetration depth. With a porous QCM, this same effect occurs, but there is an added frequency shift due to the additional liquid trapped in the pores. Since the penetration depth is much larger than the size of the pores, the trapped liquid acts like a solid mass. Due to this effect, the porous QCM has a larger frequency change due to liquid loading, but a similar dissipation as shown in the figure above.

As the density and viscosity of the fluid increases, the frequency change of the porous QCM acts like a flat QCM with the additional effect of a fluid in the pores with a greater density. This effect is observed below, as the density and viscosity of the solution becomes greater, the porous QCM begins to diverge more and more from the flat QCM data. We first measure the frequency of a QCM and the porous 3000 nm QCM in air. We then place them both into pure water and measure the frequency. The flat QCM observes a frequency shift of 700 Hz, whereas the porous QCM shifts 6400 Hz. This additional frequency change in the porous sample is due to liquid trapped in the pores. As we increase the density and viscosity we observe both substrates decrease in frequency. When we normalize the initial frequency shift of the porous QCM to the flat QCM by subtracting 5700 Hz from all of the data points, we see the effect of the denser fluid inside the pores. Since the data is normalized, the first data point in pure water shows both have a frequency change of 700 Hz. As the density and viscosity of the solution increases, we observe that the flat QCM and normalized porous QCM frequency begin to diverge. In an 85 weight percent glycerol solution the 3000 nm porous QCM diverges from the flat QCM by an additional 1400 Hz due to the increased density and viscosity of fluid in the pores. This effect is apparent in the figure below.

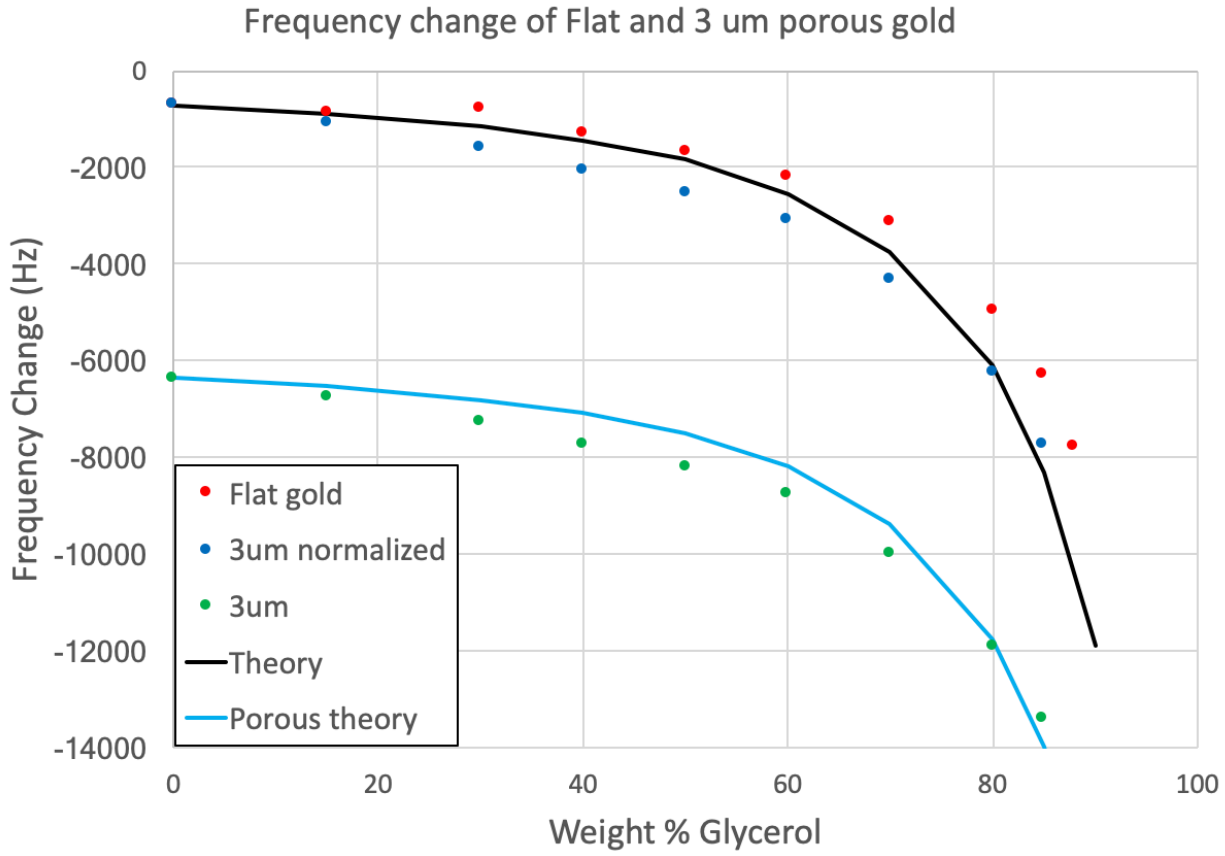

Figure 73: The dependence of the frequency change of a flat QCM and 3000 nm porous QCM on the viscoelastic properties of the liquid is displayed above. The data is fit to the Kanazawa and Gordon equation. The initial frequency is measured in air before the substrates are placed into pure water. This porous substrate has a larger initial frequency change than the flat QCM due to additional liquid trapped in the pores. The porous theory fit applies the Kanazawa and Gordon equation with the subtraction of the base frequency change from air to water for the 3000 nm substrate. The 3 μm normalized data is displayed to better compare the relation between the flat and porous QCM. The initial data point in pure water is normalized for the flat and porous samples. It is observed that as the density and viscosity of the fluid increases, the frequency change of the porous sample diverges from the flat sample. This divergence is caused by the additional density of the fluid trapped in the porous QCM.

The above water glycerol experiment demonstrates our flat QCM measurements and model of our porous QCM in liquids agree well with theory. The liquid inside the pores acts closely like a solid and rigid mass. This effect is noticeable from the lack of additional dissipation of the porous QCM compared to the flat QCM. The liquid inside the pores does cause a larger frequency shift, due to the increased mass. This frequency shift is dependent

on the fluid density and viscosity as is expected. The penetration depth for liquids is hundreds of nanometers, or even microns in the case of glycerol. This depth is huge in comparison to the small 10 nm pores of the porous QCM. Due to the no-slip boundary condition, the liquid acts like a solid in these small pores as is shown by the dissipation and frequency change plots above.

There are two primary advantages to our method of increasing sensitivity. The first is that this method can be applied to a QCM of any fundamental frequency. We chose 5 MHz QCM because they are an industry standard and easy to work with due to their size and thickness. However, this surface modification method can be used to increase the sensitivity of any flat QCM as we show in our 27 MHz QCM results shortly. The second advantage is the ability to adsorb much more analyte than on a flat QCM. A flat QCM can adsorb 0.4 μg of our thiol before being fully saturated. In comparison our 3 μm porous QCM can adsorb 0.4 mg before being fully coated. In terms of surface area, our flat QCM is 1.27 cm^2, whereas our 3 μm substrate is 0.133 m^2. This extra surface area allows the QCM to be used for much longer time periods than a flat QCM when in the same concentration.

3.15 Porous Gold at 27 MHz

A 27 MHz flat QCM as discussed before is theoretically 29x more sensitive than a 5 MHz QCM in vacuum. In liquids however, due to the increased noise and bandwidth caused by the higher fundamental frequency sensor, the limit of detection of a 27 MHz QCM is actually 2.3 times lower than a 5 MHz oscillator. Nonetheless, we wanted to add a porous substrate to this higher frequency QCM for use in bio-detection. A 1 μm thick porous gold sample was fabricated on a 27 MHz oscillator and tested as shown below. For this experiment we placed a flat and porous 27 MHz QCM in water and added 3,3'-

dithiodiprpionic acid as the thiol. An Affinix Q4 from Initium Inc. was used to measure the QCM frequency along with stirring the water and thiol solution. The oscillator was gold coated and purchased from Initium Inc. built into a plastic holder. The QCM were cleaned with piranha solution and thus could only be used for a few iterations. The thiol was mixed into an ethanol solution and injected into the water after a stable baseline was determined. The results below confirm adding porous gold to the 27 MHz QCM was successful and is comparable to our results with the 5 MHz QCM.

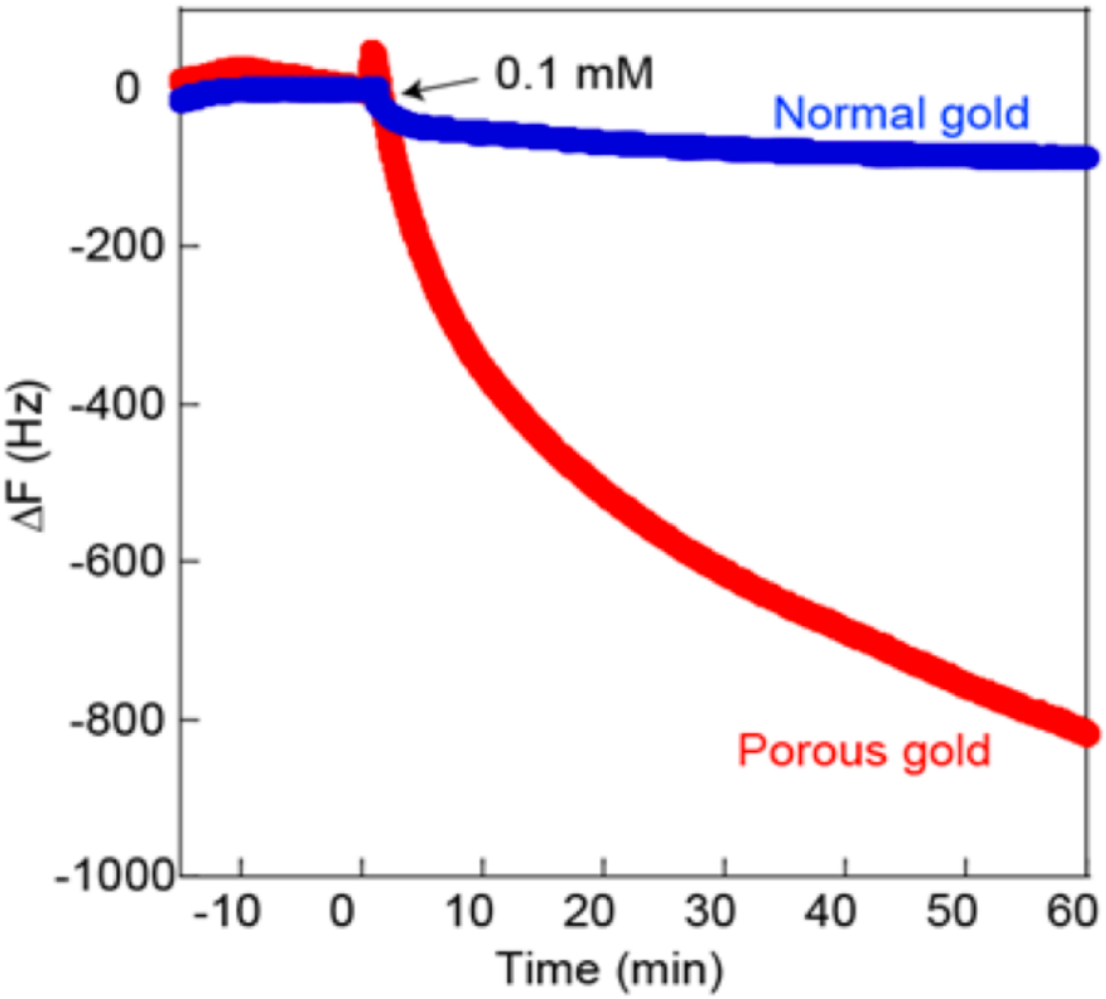

Figure 74: Above we see the result of adding a 0.1 mM concentration of 3,3'-dithiodiprpionic acid to a 27 MHz QCM in water. The results show our 1 µm sample greatly increases the sensitivity over a flat 27 MHz QCM. The flat QCM attaches 90 Hz of thiol and quickly flattens out. In the first hour the porous QCM attaches 816 Hz of thiol and continues to add mass for more than 24 hours.

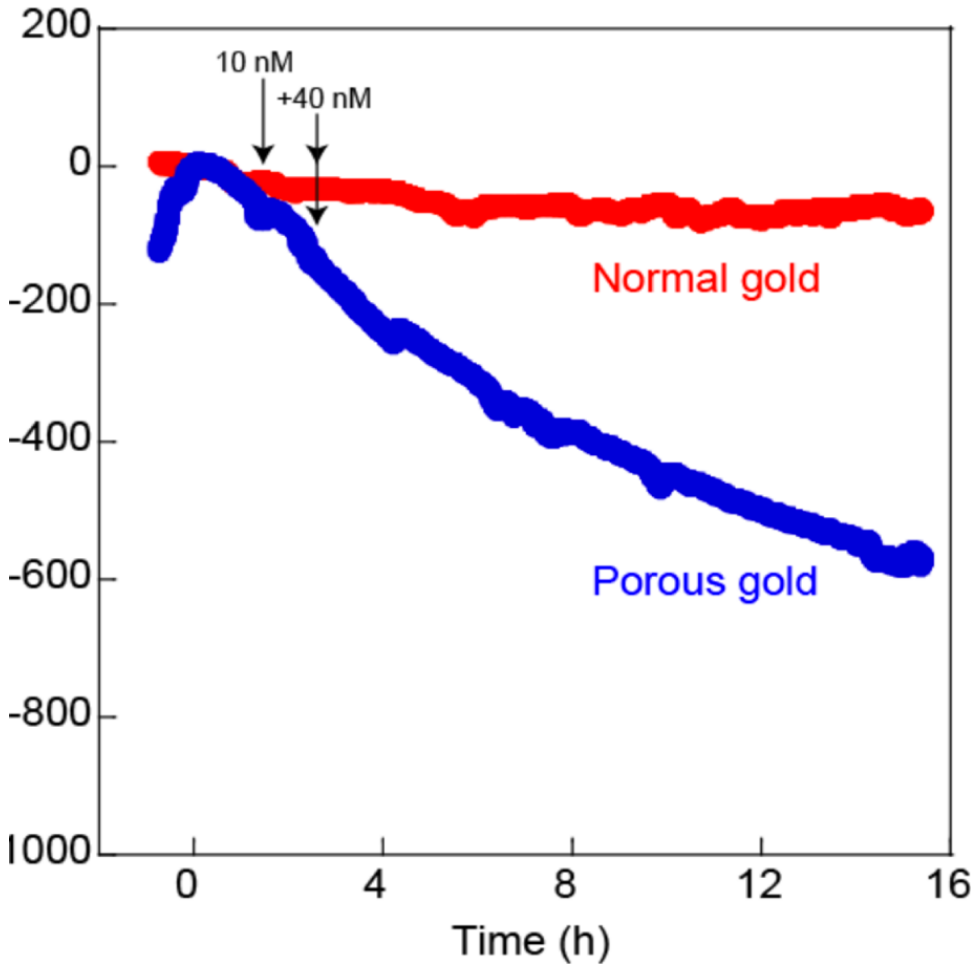

Figure 75: We now test a lower concentration of thiol to confirm the rate of adsorption is slower compared to the higher concentration results in figure 74. From the 0.1 mM trial we find it takes 27 minutes to add 600 Hz of mass to the porous QCM. In the 50 nM trial seen above we see it takes 15 hours to add the same 600 Hz of mass. That means despite it being 2000x less thiol it only takes 33x longer to attach the same amount. We again see the porous gold is much more sensitive than the flat QCM.

The results above demonstrate our porous QCM fabrication technique can be applied to QCM of various fundamental frequencies. It further shows the capability of porous gold to bind with a variety of analytes, including 3,3'-dithiodiprpionic acid. The nanomolar concentrations used in the above figure depict the advantage of using a porous QCM. With the flat QCM a low concentration of thiol is difficult to distinguish from the background noise, whereas with a porous QCM the response to low concentrations of analyte is clear.

3.16 Thiol Adsorption Kinetics

The kinetics for the adsorption of thiols onto gold surfaces to form a self-assembled monolayer is a field of study with some controversy [31,32,35,44,96,99,100,109,110]. As we described in the theory section, the accepted model for adsorption is that of a Langmuir isotherm. We previously demonstrated a diffusion model did not fit the adsorption of our QCM data. One of the first authors to suggest the Langmuir adsorption model was Blanchard et. al.. This model was described by equation 40 and we use this to fit the following adsorption results of our flat and porous QCM. The controversy for adsorption comes in a few flavors. The primary areas of concern are adsorption rate (k_{as}), the two stages of adsorption, and the frequency dependence on the concentration of thiol used.

The adsorption rate found by Blanchard et. al. is extremely fast, the group reports using a 0.01 mM solution of thiol they find $k_{as} = 0.24$ [31]. They observe their QCM fully form a monolayer within 8 seconds of injection of thiol using this concentration. They note there is a concentration dependence on the adsorption constant as our results above have also suggested. The report no two stage adsorption process. Other groups have suggested adsorption is a two stage process, where first the thiol rapidly binds to the surface in a disordered manner, and over a longer period of time, the thiol self-exchanges and forms an ordered monolayer [44,99,109]. Lastly, Blanchard finds thiol on the gold surface forms a single monolayer. This surface coverage of thiol on gold is independent of the concertation of the solution used. We include the key results from the Blanchard et. al. study below for reference [31].

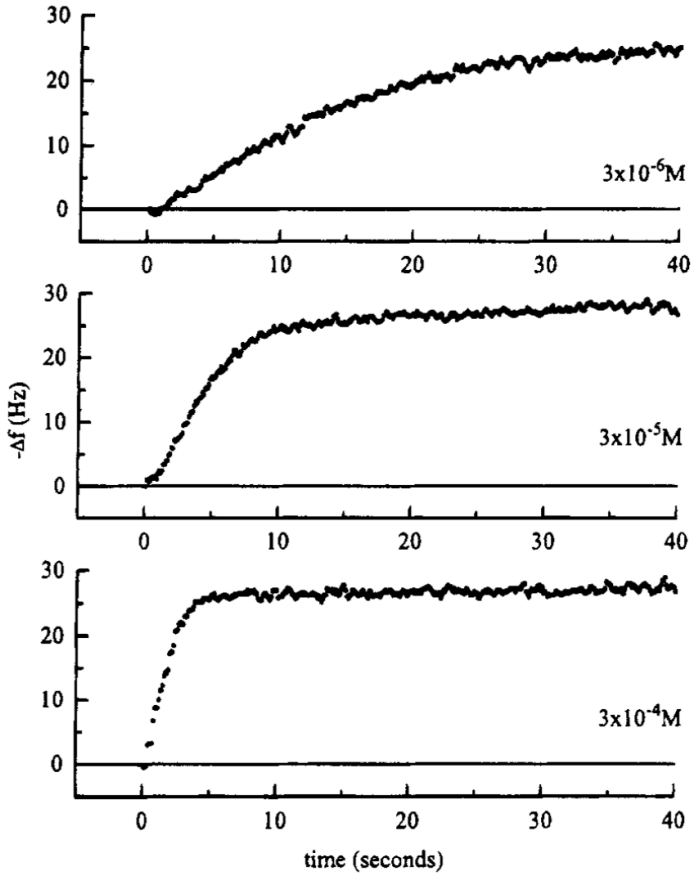

Figure 76: The concentration dependence reported by Blanchard et. al. is displayed above for reference. The group find a concentration dependence on adsorption rate for 1-octadecanethiol onto a gold surface in n-hexane. The adsorption time is much shorter than the rate found by other groups. All concentrations are shown to produce a monolayer of thiol [31].

Thiol Concentration	k_{as} (s^{-2})
1 μM	0.06
0.01 mM	0.24
0.1 mM	0.44

Table 7: The Blanchard results for the concentration dependence of the adsorption constant are displayed above for reference [31]. There is controversy on the fast adsorption observed by Blanchard et. al. as other groups find a rate that is one or two orders of magnitude slower than the above results [44,109].

The results above from Blanchard fit the Langmuir isotherm model exceedingly well. However, other groups studying the formation rates of thiol monolayers on gold surfaces report adsorption rates one to two orders of magnitude slower than the above

results [44,109]. We will briefly present the strikingly different results from a separate group before we introduce the results from our experiments. Seven years after Blanchard's results, a collaboration from Korea and Japan produced a publication finding adsorption times two orders of magnitude slower than the aforementioned results. In this study, Lee et. al. studied octadecanethiol adsorption in n-hexane onto a flat gold QCM just as Blanchard had performed. The group found the adsorption time for a 0.01 mM concentration of thiol was on the order of 800 seconds [44]. Nearly two orders of magnitude slower than Blanchard's results. Further they find there is a concentration dependence both on the rate of adsorption, and the frequency change. Lee et. al. argue they observe multilayer adsorption of thiol onto gold, which other publications confirm or refute [31,33,42,44]. We present the results from Lee et. al. below for comparison [44].

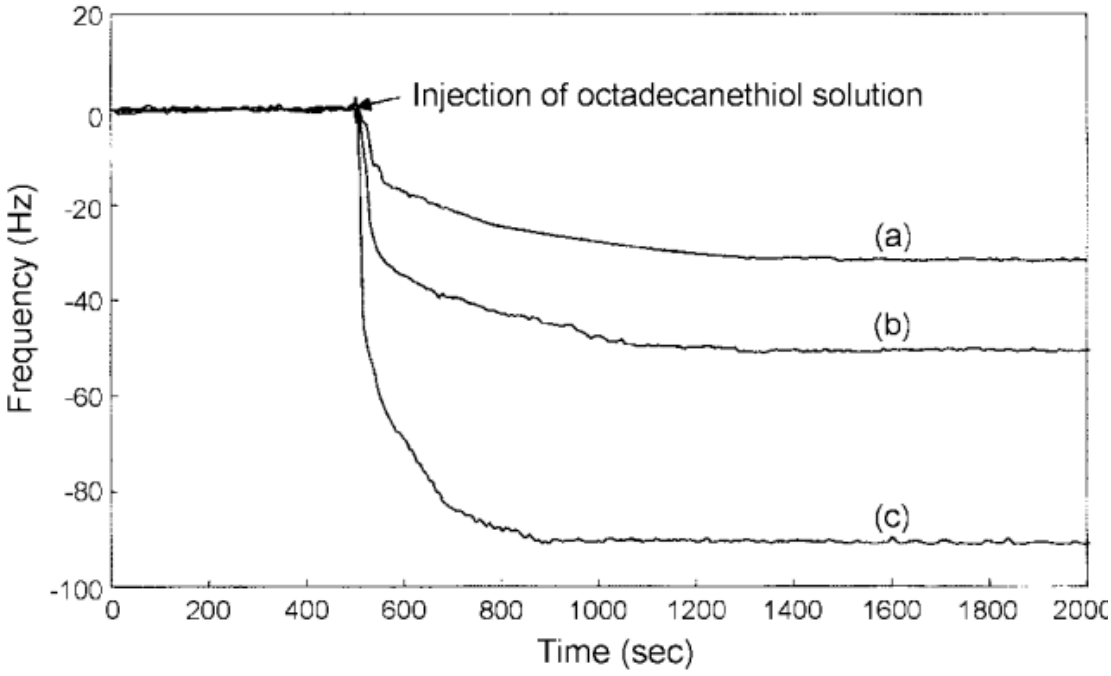

Figure 77: The kinetics results for octadecanethiol adsorption onto a flat gold QCM in n-hexane is displayed above. Lee et. al. found a concentration dependence on both rate and frequency change of the QCM. These results suggest sub-monolayer coverage for lower concentrations, and multi-layer formation for higher concentrations. In this figure the concentrations are (a) 0.1 mM, (b) 1mM, and (c) 10 mM [44].

The results from our thiol experiments on both flat and porous QCM have ranged over a wide variety of concentrations. Our results indicate that flat QCM form a single monolayer with a surface coverage of 320 $\frac{ng}{cm^2}$. We observe the same coverage of the flat QCM for concentrations ranging from 0.01 mM to 2.5 mM. For flat QCM we observe concentration does change the rate of adsorption but not the total frequency change of the sensor. However, for porous QCM we observe the concentration has an effect on both the rate of adsorption and the frequency change of the sample. The kinetic results for the adsorption of our QCM fall in-between the reported results by Blanchard et. al. and Lee et. al.. We further note we find the kinetics are dependent on the stir speed of the solution. We present our results for the kinetics of flat and porous QCM below.

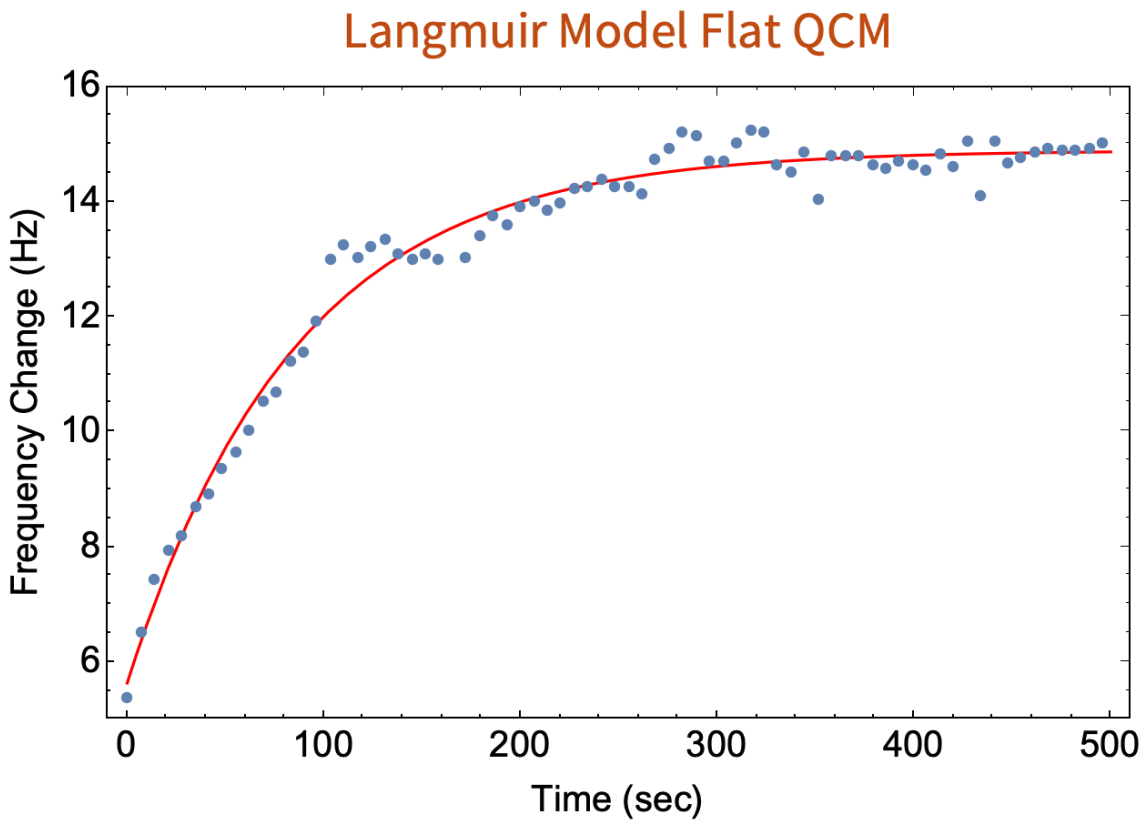

Figure 78: The Langmuir isotherm model in red described by equation 39 is fit to our data for a flat QCM adsorbing a 0.01 mM concentration of thiol in n-hexane shown above. The above fit finds $k_{as} = 0.012$.

The results above for a flat QCM found an adsorption rate k_{as} 20 times slower than the results by Blanchard using the same thiol and solvent. Compared to the results by Lee however, the results are much faster. To investigate this, we tested the dependence of stirring the solution vs allowing the thiol to diffuse. We also tested the dependence of the stir rate on adsorption rate. We found stirring the solution increased the adsorption rate greatly over allowing the thiol to diffuse in the short term adsorption. We tested the dependence of stir rate by stirring at a slow speed of 150 RPM and comparing adsorption to a high stir speed of 2500 RPM. We found the kinetics of thiol adsorption are dependent on the stir rate of the solution as is shown below.

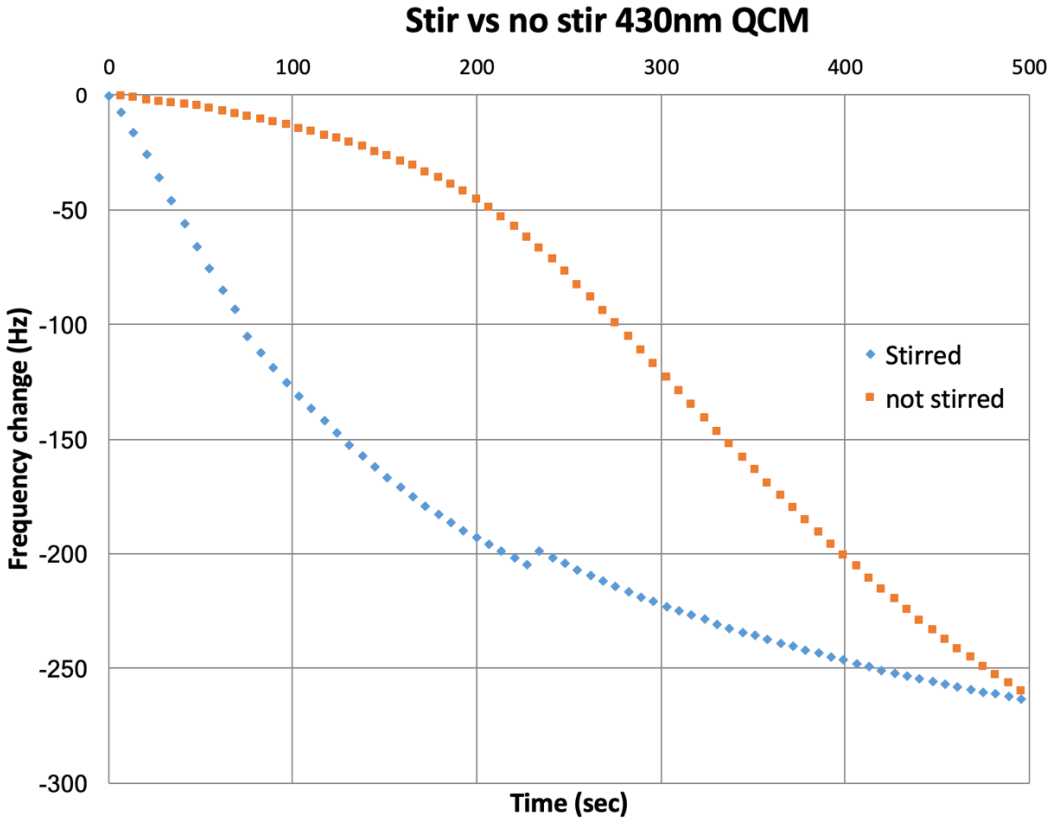

Figure 79: We find the adsorption rate is dependent on stirring the solution when compared to simply allowing the thiol to diffuse. Without stirring the thiol takes a finite time to fully propagate through the solution. Stirring also forces thiol to approach the surface of the QCM more frequently.

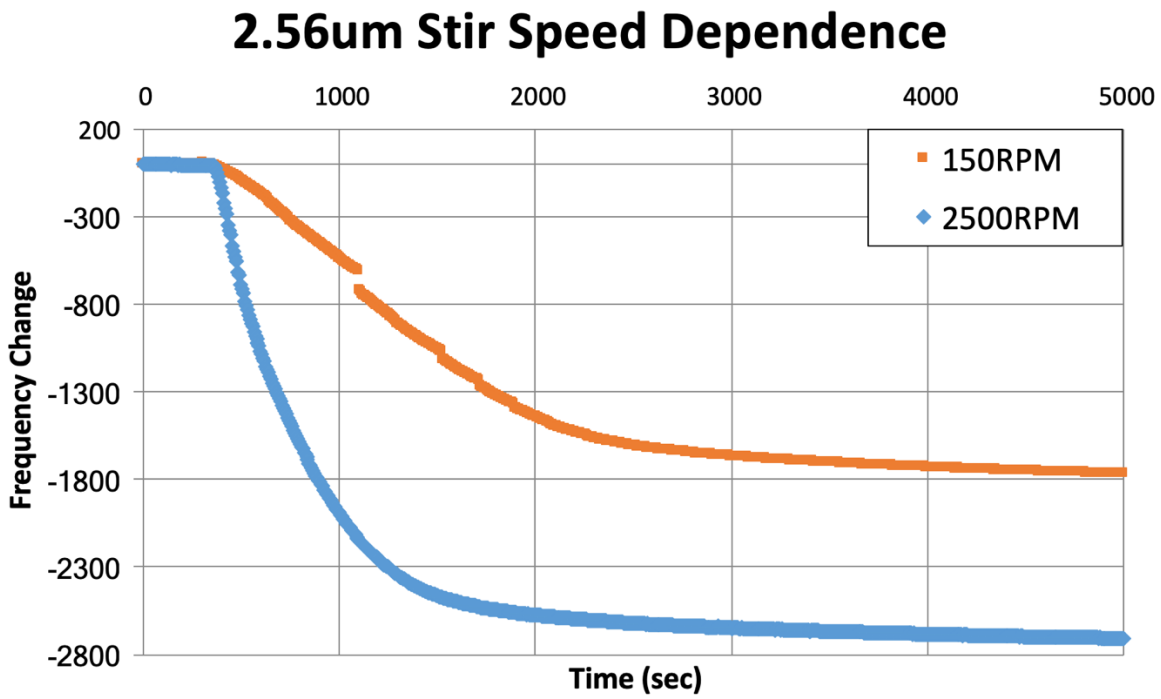

Figure 80: We test the stir speed dependence on adsorption rate as displayed above with our 2.56 μm porous QCM. We find both the adsorption rate, and the total amount of mass adsorbed are both dependent on stir speed of the solution. The faster stir speed did not increase noise in the measurements.

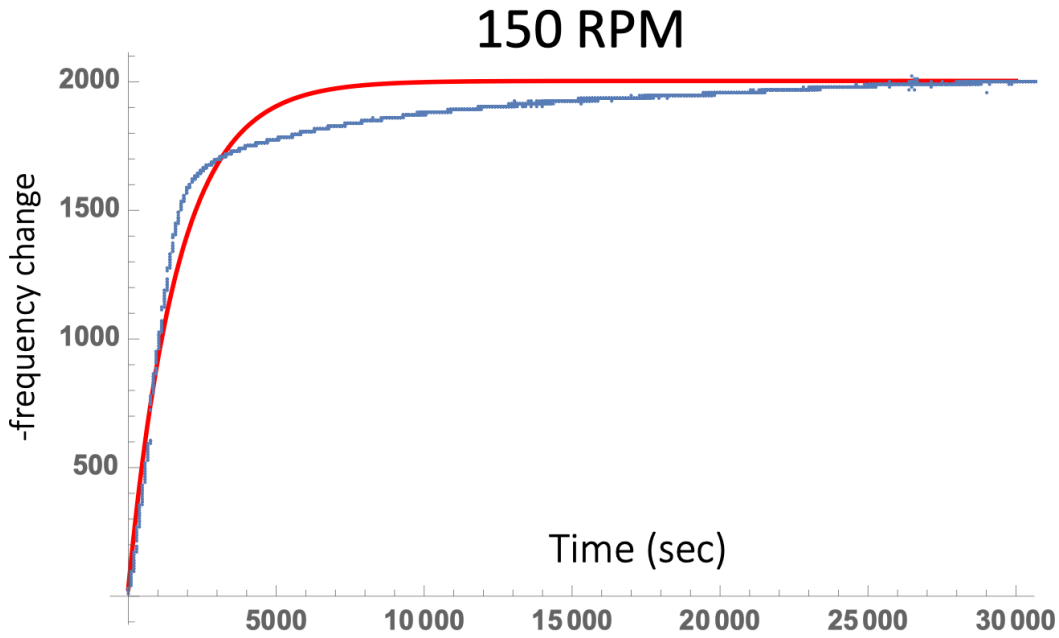

Figure 81: A fit of the Langmuir isotherm in red to the above 150 RPM stir speed results demonstrates the Langmuir model does not fit very well. The adsorption process for this slower stir speed is clearly a two-step process. First the thiol rapidly adsorbs and then the thiol slowly re-arranges adsorbing more mass on the surface.

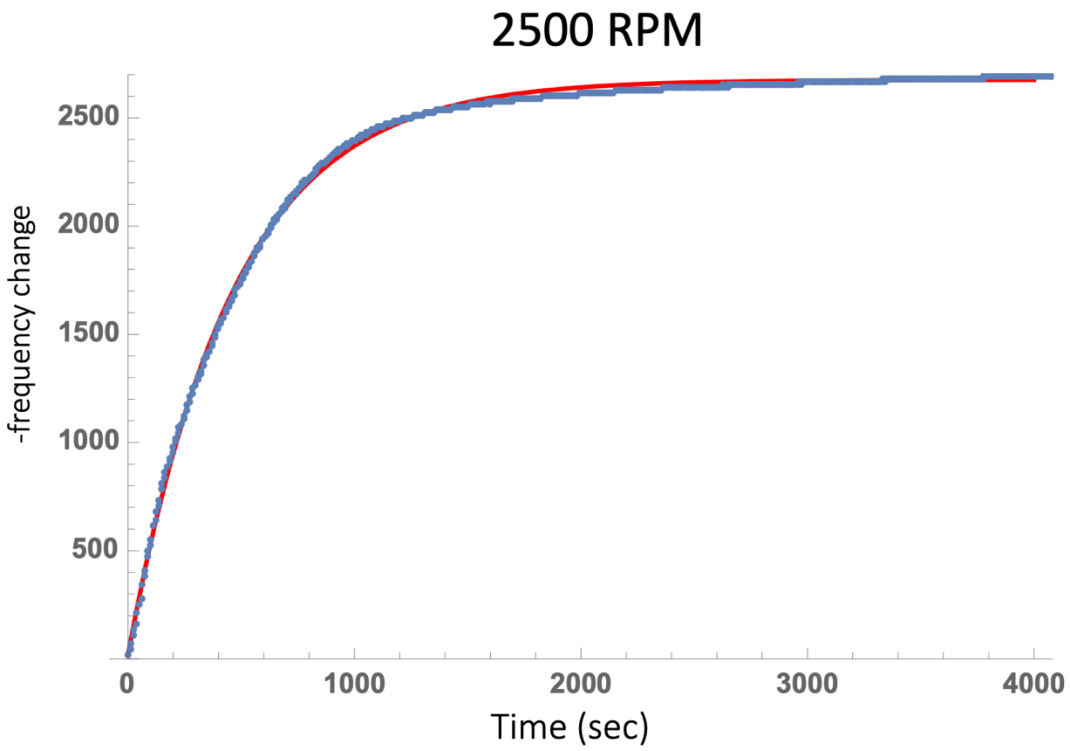

Figure 82: We compare the Langmuir isotherm model fit in red to the adsorption data from our high speed stir test shown in figure 80. We find the Langmuir model fits the high speed adsorption test much better than the slow speed trial.

From the above results we have demonstrated that the stir speed of the solution does indeed have a strong influence on the speed of adsorption. This dependence may explain some of the discrepancy between Blanchard and Lee's results. In Blanchard's study the authors indicate the solution was stirred as fast as possible without introducing noise to the QCM. Whereas other groups do not indicate the speed at which the solution is stirred. Blanchard also used a 2 sided QCM whereas our results and others typically use a QCM with one side exposed to the liquid. The Langmuir model fits QCM experiments well when the QCM rapidly adsorbs thiol and no distinct long term thiol adsorption process is observed. However, when a two-step adsorption process occurs, the Langmuir model is not as accurate. The Langmuir isotherm works reasonably well with low concentrations of thiol as will be shown.

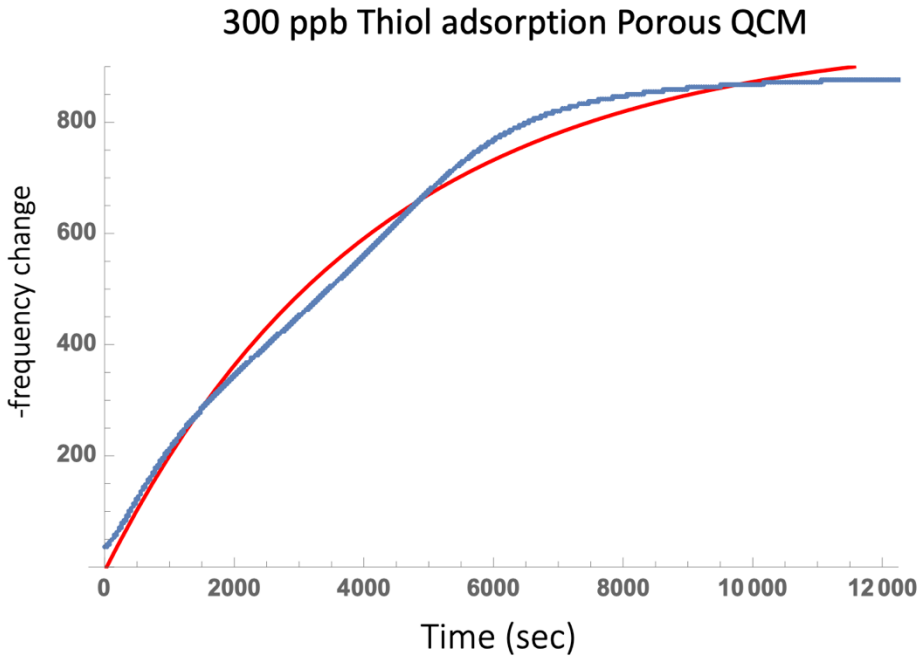

Figure 83: The adsorption process onto a porous QCM using a 1 μM concentration of thiol is displayed above. The adsorption takes a few hours to come to equilibrium. The Langmuir isotherm model in red is fit to the experimental data. For low concentration, slow adsorption processes the model works reasonably well, but is not an exact fit.

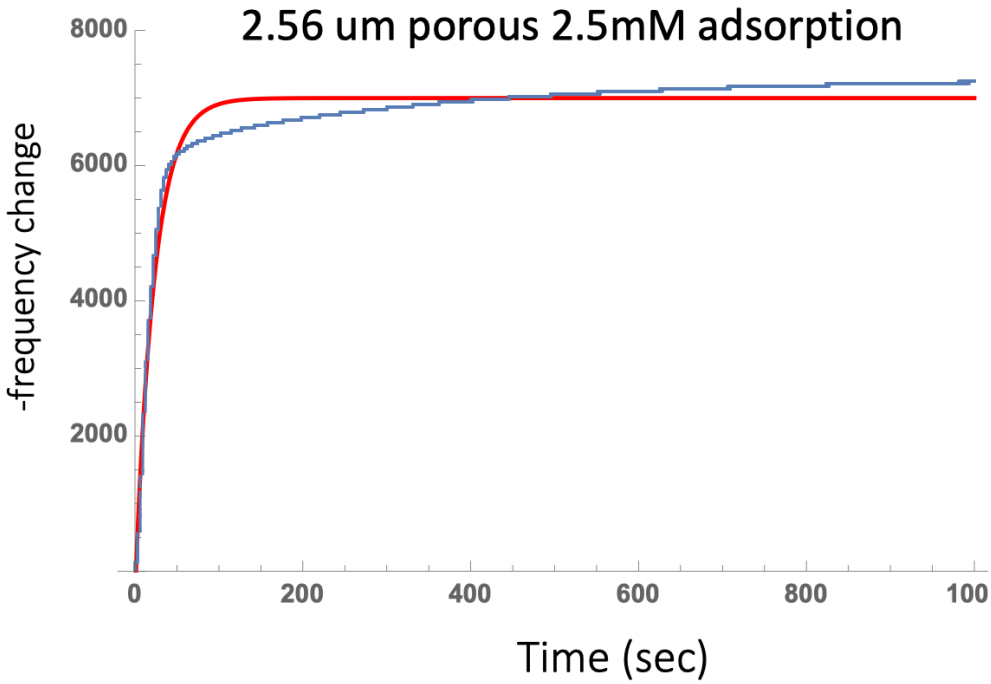

Figure 84: The adsorption of a high concentration of thiol onto a porous QCM is displayed above with the Langmuir model. The model does not exactly fit the two step adsorption characteristic of these porous substrates in high concentrations during the long term adsorption.

The two step adsorption process we observe is well explained by other authors [44,109]. Due to the fast diffusion rate of thiol, the analyte reaches the surface of the QCM quickly after injection and reach the gold surface. This quickly leads to a disordered formation of a monolayer over most of the surface. During the second stage, the disordered and defected layer is gradually consolidated due to Van der Waals interaction between neighboring thiol molecules. This explanation was verified by other groups using x-ray spectroscopy among other techniques [44].

The concentration dependence of our porous QCM and the results from Lee et. al. may be explained by defect sites. These results indicate a correlation between frequency change and the concentration of thiol used. We discussed earlier that defect sites on the QCM caused thiol to bind more strongly and not desorb from the surface. The sites that bind more strongly are pit shaped and provide additional gold surface area for the thiol to bind to. The counter-argument to this, is that there exist defect sites that have a weaker binding energy for thiol to adsorb to. The binding energy for a pit is greater than a flat surface, causing the thiol to be bound strongly and not desorb from the surface. For a weak defect site, thiol would only bind when it is more energetically favored than existing in the solution. These weak defect sites would only become populated at high concentrations. The concentration dependence observed by Lee et. al. could be easily explained by having QCM with a rough surface. The concentration dependence observed by our porous QCM is most likely the result of having a huge variety of defect sites with various binding energies. When a low concentration of thiol is used, the thiol only binds to sites with a strong binding energy. Whereas when high a concentration of thiol is used, it is energetically favored to bind to all sites, even those with a lower binding energy.

QCM	k_{as}
Blanchard 0.01mM 2-sided	0.24
Flat 0.01mM (150 RPM)	0.014
Flat 0.01mM (2500 RPM)	0.056
430nm 0.01mM (150 RPM)	0.004
2.56 μm 0.01mM (150 RPM)	0.0006
2.56 μm 0.01mM (2500 RPM)	0.0022
2.56 μm 2.5mM (2500 RPM)	0.0440

Table 8: A summary of the adsorption results k_{as} for various thicknesses of our porous QCM along with high and low stir speeds are displayed above. We compare our results to the contested results by Blanchard et. al. We further show the concentration dependence on adsorption speed.

The table above describes our adsorption constant using equation 39 to model our data. We note that while the adsorption constant is smaller for the porous substrates, these samples actually adsorb much more thiol per unit time compared to a flat QCM. For example, the flat QCM at its peak adsorption rate using a high concentration of 2.5 mM adsorbs 10 $\frac{\text{Hz}}{\text{s}}$ of thiol. Whereas our 3000 nm porous substrate using the same concentration adsorbs 650 $\frac{\text{Hz}}{\text{s}}$ of thiol. The porous substrates adsorb much more thiol per unit time than the flat substrates, however since they add so much more mass, they take longer to fully saturate. This causes the adsorption constant to be smaller than a flat QCM.

3.17 Thiol Desorption & Summary

With the kinetics of adsorption fully described, we now turn our attention to the desorption process of thiol in porous media. We have previously discussed the desorption results by Schlenoff et. al. using radiolabeled thiol on flat gold [42]. We perform our desorption experiment by first coating the 2.56 μm porous QCM in a thiol solution with a concentration of 0.01 mM. We allow the frequency to stabilize, indicating the QCM is at equilibrium with the thiol. In this trial the QCM adsorbs approximately 2750 Hz of thiol. We then take the QCM and holder out of the thiol solution and rinse the holder with clean

n-hexane to remove any additional thiol. The QCM itself is not rinsed with hexane. We then placed the now thiol coated porous QCM into clean hexane to observe the desorption of thiol. We find there is both a short term and long term desorption process. In the short term some of the thiol is rapidly removed from the surface. This short period is on the time scale of a few minutes. We continue monitoring desorption over the next 60 hours to determine the quantity of thiol desorbed.

In the Schlenoff et. al. experiment, the group found 30% of the octadecanethiol coated onto flat gold was removed when placed in clean hexane over a period of 60 hours. Since our porous surface has many defect sites, we predict the octadecanethiol will bind more strongly to the porous surface. This stronger binding of thiol will cause less of the thiol to be desorbed from the porous substrate when placed in clean n-hexane. Since we perform this experiment at a concentration of 0.01 mM, a relatively low concentration, we expect only the strong binding sites to be filled. The weak binding sites for this 2.56 μm substrate were only filled when using a high 2.5 mM concentration of thiol. Thus we expect the thiol to be strongly bound to the surface of the porous substrate, since a low concentration was used. We present the results for our desorption experiment in the figures below.

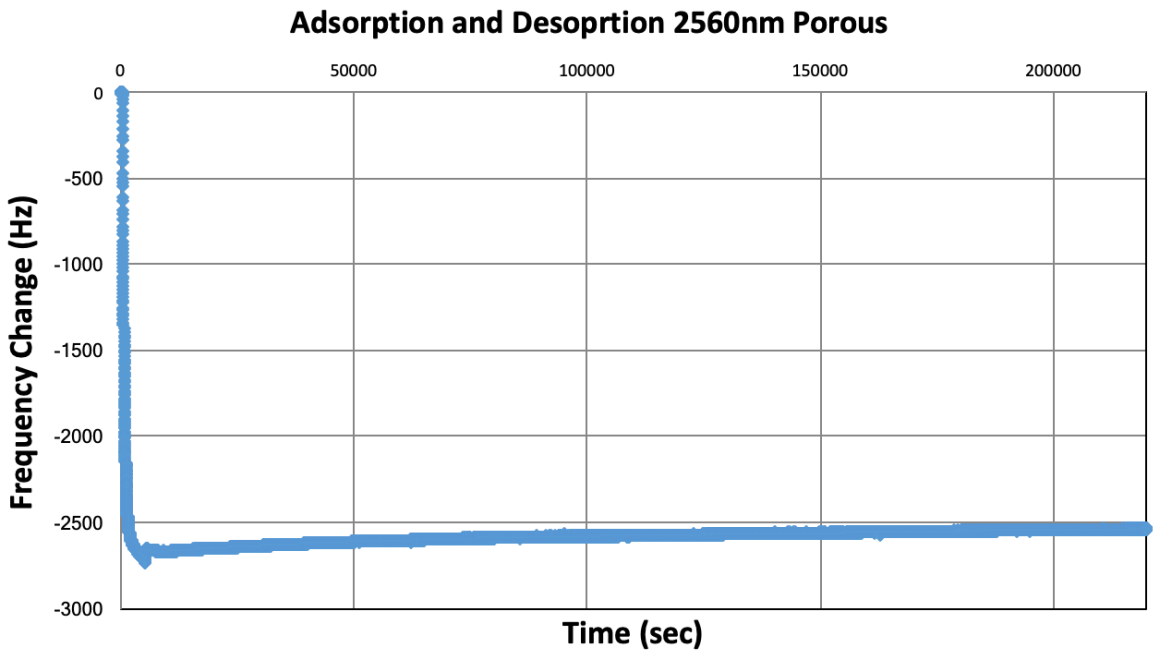

Figure 85: The entire adsorption and desorption process for the 2.56 µm porous gold QCM is displayed above. A 0.01 mM thiol concentration is used to coat the sensor. After 5000 seconds the sensor is removed from a thiol solution and placed into clean n-hexane. The desorption is allowed to continue for 60 hours.

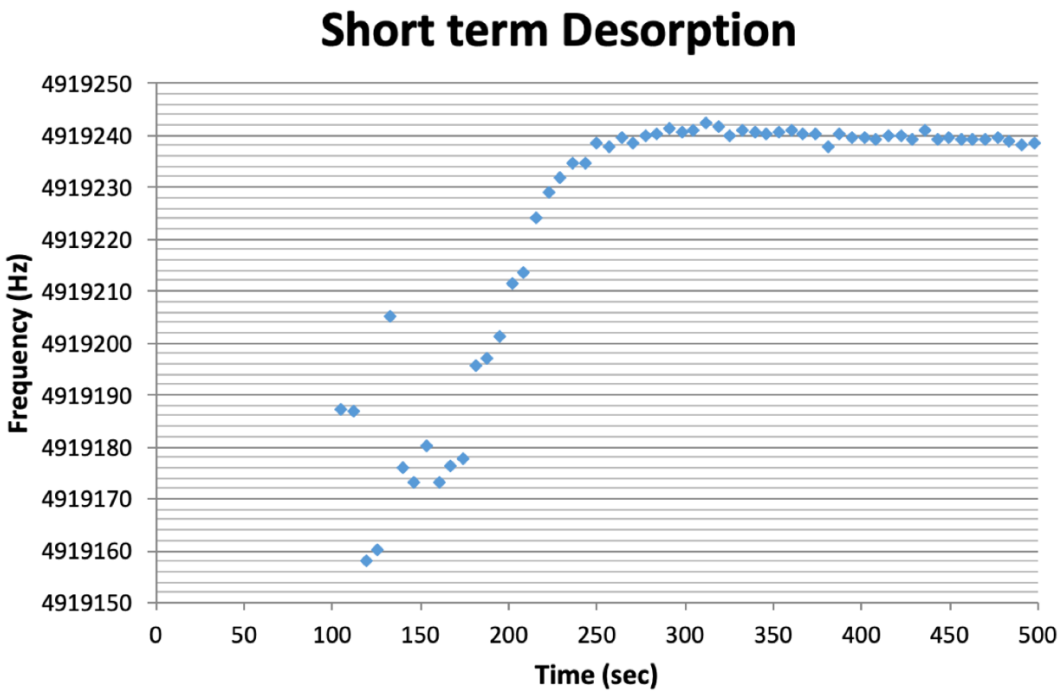

Figure 86: The short term desorption is displayed above. In the first few minutes loosely bound thiol is rapidly removed from the porous QCM. We observe 80 Hz of thiol is initially removed. The porous substrate began with 2750 Hz of thiol loaded onto the surface. This short term desorption removed approximately 3% of the thiol.

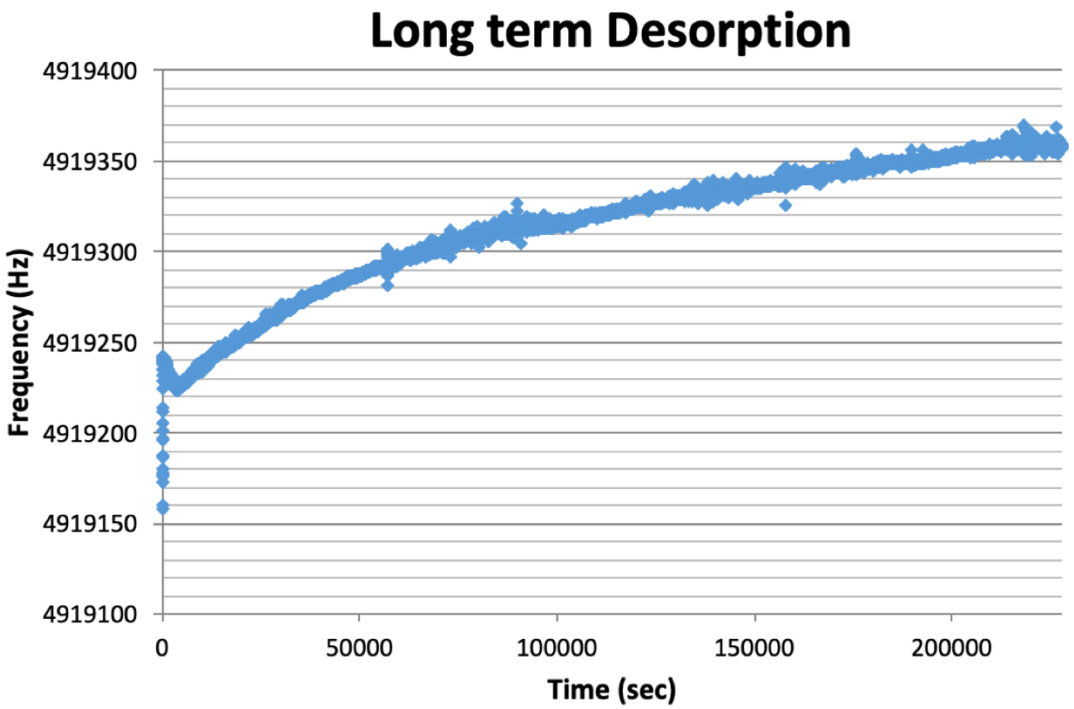

Figure 87: The entire desorption process is displayed above. The short term desorption rapidly removes 3% of the total thiol, followed by a slow desorption process over 60 hours. The long term desorption removes an additional 130 Hz of thiol before equalizing. We find the total amount of thiol removed is 210 Hz or roughly 8% of the total thiol on the porous QCM.

The results above demonstrate that our porous gold QCM desorbs much less thiol than a flat gold surface. A flat gold surface desorbs 30% of its initial thiol coating over 60 hours. Our porous QCM desorbs 8% of its initial thiol coating over this same period of time. We further note that after 55 hours of desorption, the desorption process stopped and the frequency stabilized. These results indicate that the porous structure has many more defect sites than traditional flat gold. These defect sites bind to thiol much stronger than a flat surface. This causes much less thiol to desorb from a porous structure than a flat surface. After the desorption process was complete we attempted to add thiol into the solution to determine if any of the thiol could be adsorbed. We present the results of this test below.

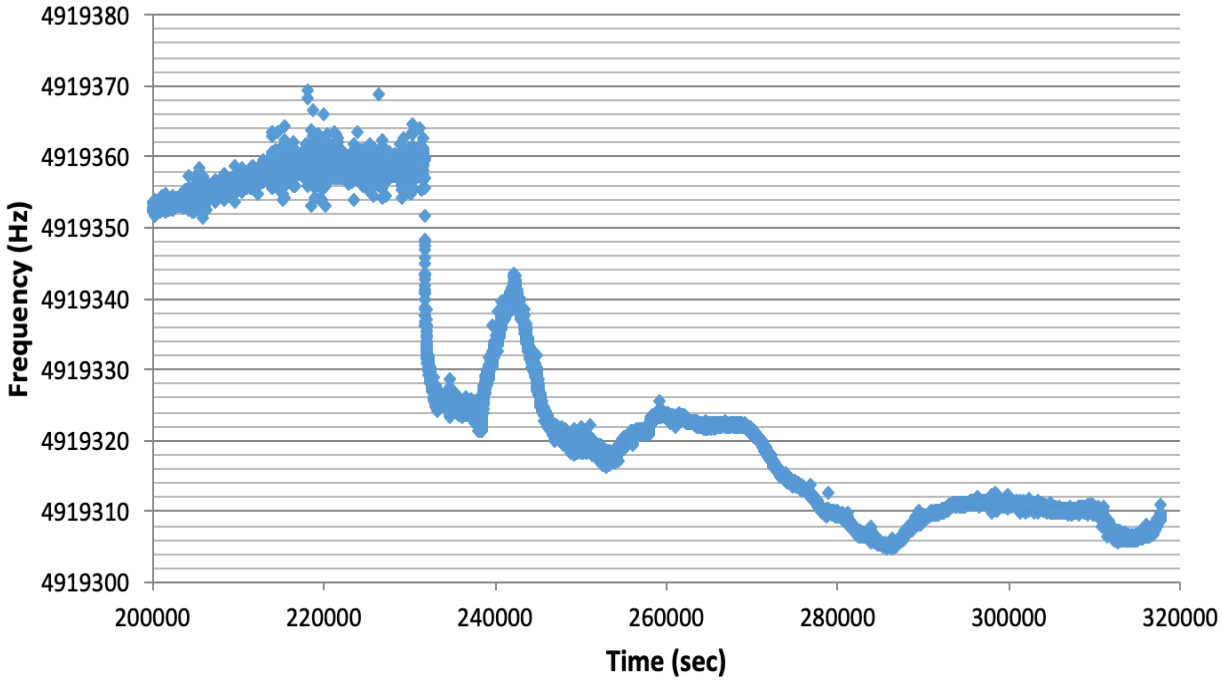

Figure 88: After the desorption process was completed and the frequency stabilized we injected a 0.01 mM concentration of thiol into the clean hexane solution. We found after desorption of 210 Hz of thiol, the porous substrate was capable of adding back on 50 Hz of thiol.

We summarize the results of our porous QCM in the table below. We include the thickness of the porous substrate, the gold atomic percent of the substrate, and the total concentration of 1-octadecanethiol in the solution. The frequency change relates to the total amount of thiol adsorbed. The sensitivity increase is the frequency change divided by the frequency change of a flat QCM indicating how much more thiol was adsorbed compared to a flat QCM. The efficiency is the thickness of the substrate divided by the sensitivity increase indicating how many nanometers of thickness were required to increase the sensitivity an additional time. These results summarize all the 5 MHz porous gold substrates presented in this dissertation. When comparing the efficiency at the 0.01 mM concentration, we find the most efficiency porous substrate has a ratio of 31.4 atomic percent gold, agreeing well with percolation theory.

Thickness	Gold at.%	Concentration	Δf (Hz)	Sensitivity Increase	Efficiency $\frac{\text{nm}}{\text{Sensitivity increase}}$
Flat	100	0.01 mM	17.4	1x	
Flat	100	2.5 mM	17.4	1x	
75nm	50	0.01 mM	87	5x	15.0
424nm	50	0.01 mM	160	9x	47.1
430nm	31.4	0.01 mM	1,479	85x	5.1
980nm	24	0.01 mM	1,838	106x	9.2
2.56μm	29.7	0.01 mM	4,017	231x	11.1
2.56μm	29.7	2.5 mM	8,654	497x	5.2
3.0μm	32.7	0.01 mM	7,775	447x	6.7
3.0μm	32.7	0.17 mM	12,956	745x	4.0
3.0μm	32.7	2.5 mM	18,167	1044x	2.9

Table 9: A summary of the results for our porous gold QCM presented in this dissertation are displayed above. We find by increasing the thickness we can increase the sensitivity of the QCM by over three orders of magnitude.

CHAPTER 4: SUMMARY AND CONCLUSIONS

Since the invention of the QCM by Sauerbrey in 1959 many advances in its uses and fabrication have been achieved [3,29]. The QCM has become commonplace in many experiments from vacuum systems, to liquids experiments, and can even be found on Mars. Quartz crystal microbalances have been written about in over 14,000 publications with a diverse set of uses and capabilities. More than 1,000 publications can be found on a QCM used to detect DNA, cells, or proteins. Just as many can be found for measuring thin films and surface properties. As a medical sensor, a QCM with functionalized thiols have been used for real time on-site detection of glucose levels, influenza, food chemical contaminants, and drug resistant bacteria [3,5–9,13,21,25–29,34,35,38,40,48]. Other popular targets are detection of explosives, pesticides, thiols, mercury, vapors, stem cells, salmonella, and many more [5–9].

More recently, surface modifications to QCM have provided a novel way to further increase the sensitivity. By increasing the surface area of the QCM in the z-direction, the sensitivity of the device can be increased [5–9]. Since most chemical and biological applications of the QCM require a gold sensing surface, we have focused on making a porous gold substrate. In this dissertation we have presented our results in fabricating porous gold surfaces that range in thickness from 75 nm to 3000 nm. We have characterized the efficiency of these substrates that range in gold from 24 to 50 atomic percent. We tested these devices using thiol adsorption with concentrations ranging from 10 nM to 2.5 mM. From these experiments we can conclude that our porous QCM are more sensitive than any other surface modified QCM ever published. Our substrates are also the most efficient per height than any other published result [5–9].

Our 430nm porous gold QCM was found to be near ideal, increasing the sensitivity of thiol adsorption 85 times using a concentration of 0.01 mM. This 31.4 atomic percent gold substrate increased the sensitivity by a factor of 10 for every 51 nm of height. The larger porous samples were not as efficient using a 0.01 mM concentration of thiol. The 430nm substrate was further capable of easily detecting 8 ppb concentrations of thiol as has been demonstrated. Our 430nm porous gold QCM has been used more than 50 times on our thiol experiments. This demonstrates we have discovered a reliable, and reusable porous sensor and cleaning technique. It has been successfully used for 7 months without deterioration.

We also created a 3 μm porous gold QCM that was found to be the most sensitive surface modified QCM ever fabricated. Our 3 μm substrate was 32.7 atomic percent gold, and was capable of adsorbing 1044 times more thiol than a flat QCM. This additional adsorption of thiol indicates we have increases the sensitivity of the QCM by more than three orders of magnitude using surface modification. The additional 4% of gold on the 3 μm substrate compared to the 430 nm sample made it slightly less efficient at adsorbing thiol in 0.01 mM concentrations. Nonetheless it was still capable of increasing the surface area to 0.133 m^2 and adsorbing 0.4 mg of thiol.

The 980 nm porous gold substrate we fabricated was 24 atomic percent gold, meaning it has 25% less gold than our 430 nm sample. This made the substrate less efficient at thiol adsorption, but provides a baseline of sensitivity increase for experiments that may require a pore size larger than 10 nm. The 10 nm pore size worked ideally for our 2 nm thiol. However, the larger pore size of our 980 nm substrate may be useful to detect

larger analytes. Nonetheless, we found our 980 nm 24 atomic percent QCM was capable of increasing the sensitivity ~100 times using a concentration of 0.01 mM.

Our concentration experiments on flat QCM have demonstrated agreement with Blanchard et. al.. We have found that both high and low concentrations of thiol added to a flat QCM produce a single monolayer with uniform surface coverage. Higher concentrations do increase the rate of adsorption of thiol. There is a further dependence of the adsorption rate on stir speed. Our results confirm the principles demonstrated by Blanchard's prior work. Our adsorption rate is found to be slower than Blanchard's results by a factor of 4.3 when a high stir speed of 2500 RPM is used. This result is still faster than Lee et. al. adsorption constant by an order of magnitude. We report the discrepancies observed by the community in adsorption rate is likely due to different stir speeds.

We can further provide insight into the controversy of the frequency change dependence of a QCM on the thiol concentration. We find that while a flat QCM observes no concentration dependence on thiol adsorption, a porous QCM does. Defect sites on the porous QCM provide an explanation for the dependency of the frequency change on the thiol concentration. The defect sites on porous gold have a range of binding energies. This range of binding energies causes some thiol to bind strongly, while others binds weakly. When a low concentration of thiol is used, the thiol is more likely to only bind to the strong binding sites. Whereas when a high concentration of thiol is used the thiol binds to all available binding sites as it is more energetically favorable than remaining in the solution. These findings are confirmed by our desorption experiments when compared to the desorption of thiol on a flat QCM. This defect site principle can also be applied to explain the concentration dependence found by Lee et. al. and others on thiol adsorption. If the flat

QCM used by Lee et. al. had a rough surface, they would indeed find a concentration dependence in thiol adsorption.

Since our porous QCM has such a huge surface area, it makes it an ideal detector for systems that wish to detect low concentrations for long periods of time. These porous QCM may be useful for biological, medical, or even long term chemical detection purposes. Since the QCM requires very little power, and can achieve such extreme selectivity and sensitivity, it may be an ideal use on an AUV. The sensor could easily detect part per billion concentrations of analyte for months or even years at a time.

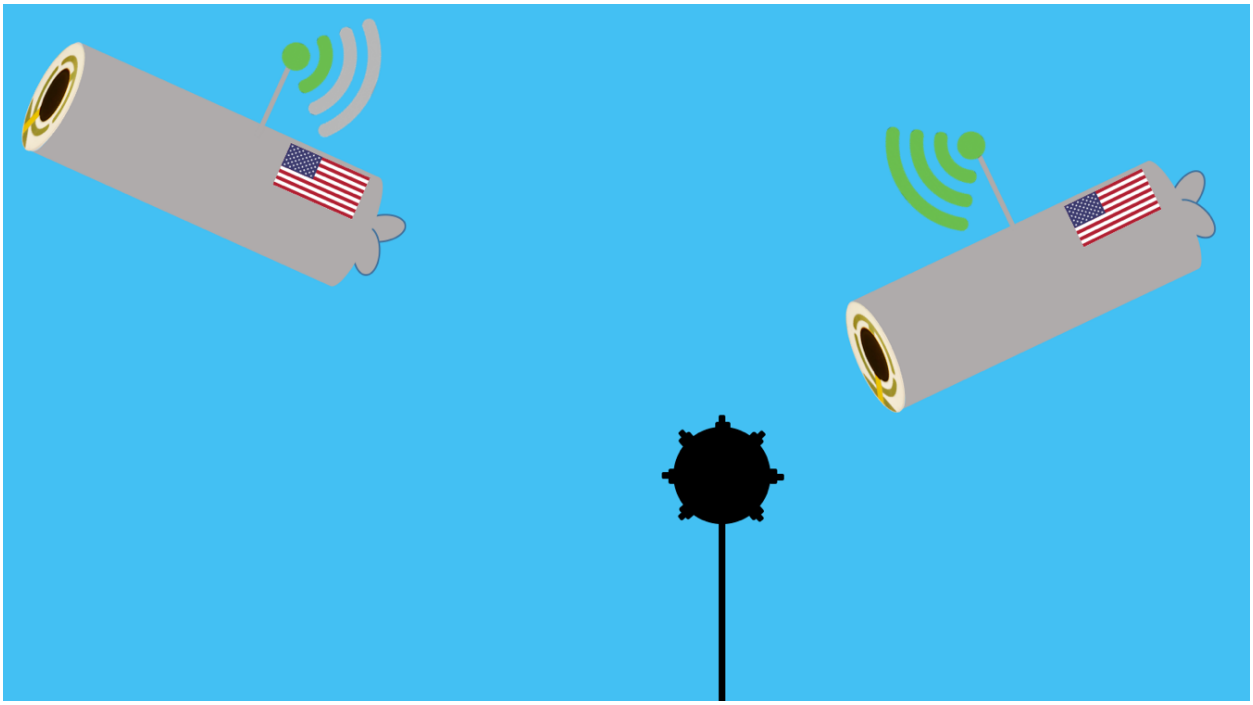

Figure 89: Given the versatility and robustness of porous QCM sensors, they are a clear advantage in the detection of unexploded ordinances found in our oceans. By adding a porous QCM sensor to an AUV, we could give ourselves a new tool to detect the previously undetectable. By adsorbing parts per billion quantities of the desired analyte, we can detect extremely low concentrations for months or even years at a time.

In conclusion, our research with porous gold QCM has confirmed our theory presented to be valid. We have documented our experimental process for collecting data, measuring thiol adsorption, cleaning the QCM, fabricating the porous gold, verifying our

results with SEM along with EDS, testing mM to nM concentrations of thiol, comparing substrates of different atomic percentage of gold, and transferring this process to a higher frequency QCM to further boost sensitivity. We have further provided insight into the controversy of kinetics of thiol adsorption. We find we have successfully increased the sensitivity of the QCM beyond that of any currently published result. Thus far we have focused our study on thiol adsorption, however there are literally thousands of applications our porous gold QCM could be used for. The potential uses for a device with such sensitivity and specificity are limitless.

REFERENCES

[1] Johannsmann, D. (2014) The Quartz Crystal Microbalance in Soft Matter Research: Fundamentals and Modeling Springer.
https://doi.org/10.1007/978-3-319-07836-6

[2] Sauerbrey, G. (1959) Use of Quartz Crystal Vibrator for Weighting Thin Films on a Microbalance. *Zeitschrift Fur Physik*, **155**, 206–222.

[3] Hussain, M., Rupp, F., Wendel, H.P. and Gehring, F.K. (2018) Bioapplications of acoustic crystals, a review. *TrAC - Trends in Analytical Chemistry*, Elsevier Ltd. **102**, 194–209.
https://doi.org/10.1016/j.trac.2018.02.009

[4] Nakhleh, M.K., Amal, H., Jeries, R., Broza, Y.Y., Aboud, M., Gharra, A. et al. (2017) Diagnosis and Classification of 17 Diseases from 1404 Subjects via Pattern Analysis of Exhaled Molecules. *ACS Nano*, **11**, 112–25.
https://doi.org/10.1021/acsnano.6b04930

[5] Lazarowich, R.J., Taborek, P., Yoo, B.Y. and Myung, N. v. (2007) Fabrication of porous alumina on quartz crystal microbalances. *Journal of Applied Physics*, **101**, 1–7.
https://doi.org/10.1063/1.2730563

[6] Lazarowich, R.J. and Taborek, P. (2006) Superfluid transitions and capillary condensation in porous media. *Physical Review B - Condensed Matter and Materials Physics*, **74**, 1–15.
https://doi.org/10.1103/PhysRevB.74.024512

[7] Bonroy, K., Friedt, J.M., Frederix, F., Laureyn, W., Langerock, S., Campitelli, A. et al. (2004) Realization and characterization of porous gold for increased protein coverage on acoustic sensors. *Analytical Chemistry*, **76**, 4299–306.
https://doi.org/10.1021/ac049893u

[8] Hieda, M., Garcia, R., Dixon, M., Daniel, T., Allara, D. and Chan, M.H.W. (2004) Ultrasensitive quartz crystal microbalance with porous gold electrodes. *Applied Physics Letters*, **84**, 628–30.
https://doi.org/10.1063/1.1643531

[9] Sabri, Y.M., Kandjani, A.E., Ippolito, S.J. and Bhargava, S.K. (2016) Ordered Monolayer Gold Nano-urchin Structures and Their Size Induced Control for High Gas Sensing Performance. *Scientific Reports*, Nature Publishing Group. **6**, 1–10.
https://doi.org/10.1038/srep24625

[10] Gufflet, N. (KVG). (2014) Quartz Crystal Resonators - Brief Review.
https://www.researchgate.net/publication/228766392

[11] Vig, J.R. (2001) Quartz Crystal Resonators and Oscillators. *Distribution*, **1**. https://www.vcamerica.com/pub/media/documents/vig3.pdf

[12] Goyal, A. (2006) Ultrasensitive quartz crystal microbalance integrated with carbon nanotubes. *ProQuest Dissertations and Theses*, 324. https://doi.org/10.1016/j.annemergmed.2014.07.115

[13] Microbalance, Q.C. and Oscillator, M.C. (2010) Operation and Service Manual Digital Controller QCM25. *Power*, **3**. https://www.thinksrs.com/downloads/pdfs/manuals/QCM200m.pdf

[14] Wilson, W.D., Yang, L., Jaiswal, A., and Poggi, M. A. (2011) Crystal Microbalance Methods for Detection. Chemosensors: Principles, Strategies, and Applications. P. 329. John Wiley & Sons, Inc.

[15] Kashan, M.A.M., Kalavally, V., Lee, H.W. and Ramakrishnan, N. (2016) Resonant characteristics and sensitivity dependency on the contact surface in QCM-micropillar-based system of coupled resonator sensors. *Journal of Physics D: Applied Physics*, IOP Publishing. **49**. https://doi.org/10.1088/0022-3727/49/19/195303

[16] 3T analytik. Automated Surface Interaction Analysis qCell T Series. 1–4. https://www.3t-analytik.de/sites/default/files/qCell_T_Series_features_2017_Web.pdf

[17] OpenQCM technology (2019). https://openqcm.com/technology

[18] INITIUM. (2019) AFFINIX Q4. 1–2. http://www.initium2000.com/product/q4.html#mainCont

[19] AWSensors. (2019) AWS-HFF, Scientific Technology. 1–4. https://awsensors.com/sensors/

[20] García, J. v., Rocha, M.I., March, C., García, P., Francis, L.A., Montoya, A. et al. (2014) Love Mode surface acoustic wave and high fundamental frequency quartz crystal microbalance immunosensors for the detection of carbaryl pesticide. *Procedia Engineering*, **87**, 759–62. https://doi.org/10.1016/j.proeng.2014.11.649

[21] Cervera-Chiner, L., Juan-Borrás, M., March, C., Arnau, A., Escriche, I., Montoya, Á. et al. (2018) High Fundamental Frequency Quartz Crystal Microbalance (HFF-QCM) immunosensor for pesticide detection in honey. *Food Control*, **92**, 1–6. https://doi.org/10.1016/j.foodcont.2018.04.026

[22] King, W.H. (1964) Piezoelectric Sorption Detector. *Analytical Chemistry*, **36**, 1735–9. https://doi.org/10.1021/ac60215a012

[23] Pensa, E., Cortés, E., Corthey, G., Carro, P., Vericat, C., Fonticelli, M.H. et al. (2012) The chemistry of the sulfur-gold interface: In search of a unified model. *Accounts of Chemical Research*, **45**, 1183–92. https://doi.org/10.1021/ar200260p

[24] Häkkinen, H. (2012) The gold-sulfur interface at the nanoscale. *Nature Chemistry*, Nature Publishing Group. **4**, 443–55. https://doi.org/10.1038/nchem.1352

[25] Hraybi, A., Mougharbel, I., Kassem, K. and Ghaziri, H. (2017) Quartz crystal microbalance (QCM) for the detection of explosive vapor - Measurements and simulations. *2017 1st International Conference on Landmine: Detection, Clearance and Legislations, LDCL 2017*, 16–21. https://doi.org/10.1109/LDCL.2017.7976933

[26] Erbahar, D.D., Gurol, I., Arisen, V., Öztürk, Z.Z., Musluoglu, E. and Harbeck, M. (2011) Explosives detection in sea water with phthalocyanine quartz crystal microbalance sensors. *Sensor Letters*, **9**, 745–8. https://doi.org/10.1166/sl.2011.1607

[27] Maglio, O., Costanzo, S., Cercola, R., Zambrano, G., Mauro, M., Battaglia, R. et al. (2017) A quartz crystal microbalance immunosensor for stem cell selection and extraction. *Sensors (Switzerland)*, **17**, 1–14. https://doi.org/10.3390/s17122747

[28] Waiwijit, U., Jaruwongrungsee, K., Chokesajjawatee, N., Promjai, J., Lomas, T., Sritongkham, P. et al. (2012) QCM-Based DNA biosensor for Salmonella typhimurium detection. *2012 IEEE International Conference on Electron Devices and Solid State Circuit, EDSSC 2012*, IEEE. 1–3. https://doi.org/10.1109/EDSSC.2012.6482844

[29] Bragazzi, Amicizia, Panatto, Tramalloni, Valle and Gasparini. (2015) Quartz-Crystal Microbalance (QCM) for Public Health: An Overview of Its Applications. *Adv Protein Chem Struct Biol*. https://doi.org/10.1016/bs.apcsb.2015.08.002

[30] Karpovich, D.S. and Blanchard, G.J. (1995) An undergraduate laboratory experiment for the direct measurement of monolayer-formation kinetics. *Journal of Chemical Education*, **73**, 466–70.

[31] Karpovich, D.S. and Blanchard, G.J. (1994) Direct Measurement of the Adsorption Kinetics of Alkanethiolate Self-Assembled Monolayers on a Microcrystalline Gold Surface. *Langmuir*, **10**, 3315–22. https://doi.org/10.1021/la00021a066

[32] Karpovich, D.S. and Blanchard, G.J. (1997) Vapor adsorption onto metal and modified interfaces: Evidence for adsorbate penetration of an alkanethiol monolayer on gold. *Langmuir*, **13**, 4031–7.

[33] Kim, Y.T., McCarley, R.L. and Bard, A.J. (1993) Observation of n-Octadecanethiol Multilayer Formation from Solution onto Gold. *Langmuir*, **9**, 1941–4. https://doi.org/10.1021/la00032a001

[34] Westen, R., Mei, H.C., de Raedt, H., Olsson, A.L.J., Busscher, H.J. and Sharma, P.K. (2016) Quantification of the viscoelasticity of the bond of biotic and abiotic particles adhering to solid-liquid interfaces using a window-equipped quartz crystal microbalance with dissipation. *Colloids and Surfaces B: Biointerfaces*, Elsevier B.V. **148**, 255–62. https://doi.org/10.1016/j.colsurfb.2016.08.062

[35] Vericat, C., Vela, M.E., Benitez, G., Carro, P. and Salvarezza, R.C. (2010) Self-assembled monolayers of thiols and dithiols on gold: New challenges for a well-known system. *Chemical Society Reviews*, **39**, 1805–34. https://doi.org/10.1039/b907301a

[36] Zimmermann, B., Lucklum, R., Hauptmann, P., Rabe, J. and Büttgenbach, S. (2001) Electrical characterisation of high-frequency thickness-shear-mode resonators by impedance analysis. *Sensors and Actuators, B: Chemical*, **76**, 47–57. https://doi.org/10.1016/S0925-4005(01)00567-6

[37] Noort, D., Rani, R. and Mandenius, C.F. (2001) Improving the sensitivity of a quartz crystal microbalance for biosensing by using porous gold. *Mikrochimica Acta*, **136**, 49–53. https://doi.org/10.1007/s006040170066

[38] Lazarowich, R. and Taborek, P. (2006) Phase behavior of helium in porous media. ProQuest Dissertations Publishing, 3236680. https://search.proquest.com/docview/305356788?accountid=14509

[39] Urbakh, M. and Daikhin, L. (1994) Roughness effect on the frequency of a quartz-crystal resonator in contact with a liquid. *Physical Review B*, **49**, 4866–70. https://doi.org/10.1103/PhysRevB.49.4866

[40] Chen, X., Chen, X., Li, N., Ding, X. and Zhao, X. (2016) A QCM Humidity Sensors Based on GO/Nafion Composite Films with Enhanced Sensitivity. *IEEE Sensors Journal*, **16**, 8874–83.
https://doi.org/10.1109/JSEN.2016.2617122

[41] Miller, J.G. and Bolef, D.I. (1968) Sensitivity Enhancement by the Use of Acoustic Resonators in cw Ultrasonic Spectroscopy. *Journal of Applied Physics*, **39**, 4589–93.

[42] Schlenoff, J.B., Li, M. and Ly, H. (1995) Stability and Self-Exchange in Alkanethiol Monolayers. *Journal of the American Chemical Society*, **117**, 12528–36. https://doi.org/10.1021/ja00155a016

[43] Chen, L., Liang, S., Yan, R., Cheng, Y., Huai, X. and Chen, S. (2009) N-Octadecanethiol self-assembled monolayer coating with microscopic roughness for dropwise condensation of steam. *Journal of Thermal Science*, **18**, 160–5.
https://doi.org/10.1007/s11630-009-0160-z

[44] Kim, D.H., Noh, J., Hara, M. and Lee, H. (2001) An adsorption process study on the self-assembled monolayer formation of octadecanethiol chemisorbed on gold surface. *Bulletin of the Korean Chemical Society*, **22**, 276–80.

[45] Glassford, A.P.M. (1978) Response of a Quartz Crystal Microbalance to a Liquid Deposit. *J Vac Sci Technol*, **15**, 1836–43.
https://doi.org/10.1116/1.569851

[46] Kanazawa, K.K. and Gordon, J.G. (1985) Frequency of a Quartz Microbalance in Contact with Liquid. *Analytical Chemistry*, **57**, 1770–1.
https://doi.org/10.1021/ac00285a062

[47] Martin, S.J., Granstaff, V.E. and Frye, G.C. (1991) Characterization of a Quartz Crystal Microbalance with Simultaneous Mass and Liquid Loading. *Analytical Chemistry*, **63**, 2272–81.
https://doi.org/10.1021/ac00020a015

[48] García-Martinez, G., Bustabad, E.A., Perrot, H., Gabrielli, C., Bucur, B., Lazerges, M. et al. (2011) Development of a mass sensitive quartz crystal microbalance (QCM)-based DNA biosensor using a 50 MHz electronic oscillator circuit. *Sensors*, **11**, 7656–64. https://doi.org/10.3390/s110807656

[49] Johannsmann, D., Reviakine, I. and Richter, R.P. (2009) Dissipation in films of adsorbed nanospheres studied by quartz crystal microbalance (QCM). *Analytical Chemistry*, **81**, 8167–76.
https://doi.org/10.1021/ac901381z

[50] Bingen, P., Wang, G., Steinmetz, N.F., Rodahl, M. and Richter, R.P. (2008) Solvation effects in the quartz crystal microbalance with dissipation monitoring response to biomolecular adsorption. A phenomenological approach. *Analytical Chemistry*, **80**, 8880–90.
https://doi.org/10.1021/ac8011686

[51] Tellechea, E., Johannsmann, D., Steinmetz, N.F., Richter, R.P. and Reviakine, I. (2009) Model-independent analysis of QCM data on colloidal particle adsorption. *Langmuir*, **25**, 5177–84.
https://doi.org/10.1021/la803912p

[52] Johannsmann, D., Reviakine, I., Rojas, E. and Gallego, M. (2008) Effect of sample heterogeneity on the interpretation of QCM(-D) data: Comparison of combined quartz crystal microbalance/atomic force microscopy measurements with finite element method modeling. *Analytical Chemistry*, **80**, 8891–9.
https://doi.org/10.1021/ac8013115

[53] Tsortos, A., Papadakis, G., Mitsakakis, K., Melzak, K.A. and Gizeli, E. (2008) Quantitative determination of size and shape of surface-bound DNA using an acoustic wave sensor. *Biophysical Journal*, Elsevier. **94**, 2706–15.
https://doi.org/10.1529/biophysj.107.119271

[54] Papadakis, G., Tsortos, A., Kordas, A., Tiniakou, I., Morou, E., Vontas, J. et al. (2013) Acoustic detection of DNA conformation in genetic assays combined with PCR. *Scientific Reports*, **3**, 1–8.
https://doi.org/10.1038/srep02033

[55] Larsson, C., Rodahl, M. and Höök, F. (2003) Characterization of DNA immobilization and subsequent hybridization on a 2D arrangement of streptavidin on a biotin-modified lipid bilayer supported on SiO2. *Analytical Chemistry*, **75**, 5080–7.
https://doi.org/10.1021/ac034269n

[56] Su, X., Wu, Y.J. and Knoll, W. (2005) Comparison of surface plasmon resonance spectroscopy and quartz crystal microbalance techniques for studying DNA assembly and hybridization. *Biosensors and Bioelectronics*, **21**, 719–26.
https://doi.org/10.1016/j.bios.2005.01.006

[57] Madaboosi, N., Neumann, F., Hernández-Neuta, I., Salas, J., Mecea, V. and Nilsson, M. (2017) Real-Time QCM Measurements of Rolling Circle Amplification Products. *Proceedings*, **1**, 509.
https://doi.org/10.3390/proceedings1040509

[58] Losic, D., Mitchell, J.G. and Voelcker, N.H. (2005) Complex gold nanostructures derived by templating from diatom frustules. *Chemical Communications*, 4905–7.
https://doi.org/10.1039/b508733c

[59] Lu, Y., Wang, Q., Sun, J. and Shen, J. (2005) Selective dissolution of the silver component in colloidal Au and Ag multilayers: A facile way to prepare nanoporous gold film materials. *Langmuir*, **21**, 5179–84. https://doi.org/10.1021/la0500878

[60] Haupt, M., Miller, S., Glass, R., Arnold, M., Sauer, R., Thonke, K. et al. (2003) Nanoporous gold films created using templates formed from self-assembled structures of inorganic-block copolymer micelles. *Advanced Materials*, **15**, 829–31. https://doi.org/10.1002/adma.200304688

[61] Li, K., Huang, J., Shi, G., Zhang, W. and Jin, L. (2011) A Sensitive Nanoporous Gold-Based Electrochemical DNA Biosensor for Escherichia coli Detection. *Analytical Letters*, **44**, 2559–70. https://doi.org/10.1080/00032719.2011.553004

[62] Wittstock, A., Wichmann, A., Biener, J. and Bäumer, M. (2011) Nanoporous gold: A new gold catalyst with tunable properties. *Faraday Discussions*, **152**, 87–98. https://doi.org/10.1039/c1fd00022e

[63] Chen, Z., Jiang, J., Shen, G. and Yu, R. (2005) Impedance immunosensor based on receptor protein adsorbed directly on porous gold film. *Analytica Chimica Acta*, **553**, 190–5. https://doi.org/10.1016/j.aca.2005.08.014

[64] Nyce, G.W., Hayes, J.R., Hamza, A. v. and Satcher, J.H. (2007) Synthesis and characterization of hierarchical porous gold materials. *Chemistry of Materials*, **19**, 344–6. https://doi.org/10.1021/cm062569q

[65] Zhao, W., Xu, J.J., Shi, C.G. and Chen, H.Y. (2006) Fabrication, characterization and application of gold nano-structured film. *Electrochemistry Communications*, **8**, 773–8. https://doi.org/10.1016/j.elecom.2006.03.009

[66] Shah, P.S., Sigman, M.B., Stowell, C.A., Lim, K.T., Johnston, K.P. and Korgel, B.A. (2003) Single-step self-organization of ordered macroporous nanocrystal thin films. *Advanced Materials*, **15**, 971–4. https://doi.org/10.1002/adma.200304903

[67] Losic, D., Mitchell, J.G. and Voelcker, N.H. (2006) Fabrication of gold nanostructures by templating from porous diatom frustules. *New Journal of Chemistry*, **30**, 908–14. https://doi.org/10.1039/b600073h

[68] Gu, H., Wang, C., Gong, S., Mei, Y., Li, H. and Ma, W. (2016) Investigation on contact angle measurement methods and wettability transition of porous surfaces. *Surface and Coatings Technology*, Elsevier B.V. **292**, 72–7. https://doi.org/10.1016/j.surfcoat.2016.03.014

[69] Politi, J., Dardano, P., Caliò, A., Iodice, M., Rea, I. and de Stefano, L. (2017) Reversible sensing of heavy metal ions using lysine modified oligopeptides on porous silicon and gold. *Sensors and Actuators, B: Chemical*, Elsevier B.V. **244**, 142–50. https://doi.org/10.1016/j.snb.2016.12.132

[70] Shulga, O. v., Jefferson, K., Khan, A.R., D'Souza, V.T., Liu, J., Demchenko, A. v. et al. (2007) Preparation and characterization of porous gold and its application as a platform for immobilization of acetylcholine esterase. *Chemistry of Materials*, **19**, 3902–11. https://doi.org/10.1021/cm070238n

[71] Zhang, R. and Olin, H. (2014) Porous gold films-a short review on recent progress. *Materials*, **7**, 3834–54. https://doi.org/10.3390/ma7053834

[72] Yin, H., Zhou, C., Xu, C., Liu, P., Xu, X. and Ding, Y. (2008) Aerobic Oxidation of D - Glucose on Support-Free Nanoporous Gold. 9673–8.

[73] Zhang, H., Xu, J.J. and Chen, H.Y. (2008) Shape-controlled gold nanoarchitectures: Synthesis, superhydrophobicity, and electrocatalytic properties. *Journal of Physical Chemistry C*, **112**, 13886–92. https://doi.org/10.1021/jp802012h

[74] Li, Y., Song, Y.Y., Yang, C. and Xia, X.H. (2007) Hydrogen bubble dynamic template synthesis of porous gold for nonenzymatic electrochemical detection of glucose. *Electrochemistry Communications*, **9**, 981–8. https://doi.org/10.1016/j.elecom.2006.11.035

[75] Xia, Y., Huang, W., Zheng, J., Niu, Z. and Li, Z. (2011) Nonenzymatic amperometric response of glucose on a nanoporous gold film electrode fabricated by a rapid and simple electrochemical method. *Biosensors and Bioelectronics*, Elsevier B.V. **26**, 3555–61. https://doi.org/10.1016/j.bios.2011.01.044

[76] Bai, Y., Yang, W., Sun, Y. and Sun, C. (2008) Enzyme-free glucose sensor based on a 3-dimensional gold film electrode. *Sensors and Actuators, B: Chemical*, **134**, 471–6. https://doi.org/10.1016/j.snb.2008.05.028

[77] Zhao, B. and Collinson, M.M. (2012) Hierarchical porous gold electrodes: Preparation, characterization, and electrochemical behavior. *Journal of Electroanalytical Chemistry*, Elsevier B.V. **684**, 53–9. https://doi.org/10.1016/j.jelechem.2012.08.025

[78] Hieda, M., Garcia, R., Dixon, M., Daniel, T., Allara, D. and Chan, M.H.W. (2004) Ultrasensitive quartz crystal microbalance with porous gold electrodes. *Applied Physics Letters*, **84**, 628–30.
https://doi.org/10.1063/1.1643531

[79] Wei, H., Minghua, W., Jufang, Z. and Zelin, L. (2009) Facile fabrication of multifunctional three-dimensional hierarchical porous gold films via surface rebuilding. *Journal of Physical Chemistry C*, **113**, 1800–5.
https://doi.org/10.1021/jp8095693

[80] Tavakkoli, N., Nasrollahi, S. and Vatankhah, G. (2012) Electrocatalytic Determination of Ascorbic Acid Using a Palladium Coated Nanoporous Gold Film Electrode. *Electroanalysis*, **24**, 368–75.
https://doi.org/10.1002/elan.201100414

[81] Kiani, A. and Hatami, S. (2010) Fabrication of platinum coated nanoporous gold film electrode: A nanostructured ultra low-platinum loading electrocatalyst for hydrogen evolution reaction. *International Journal of Hydrogen Energy*, Elsevier. **35**, 5202–9.
https://doi.org/10.1016/j.ijhydene.2010.03.014

[82] Gloria, D., Justin Gooding, J., Moran, G. and Brynn Hibbert, D. (2011) Electrochemically fabricated three dimensional nano-porous gold films optimised for surface enhanced Raman scattering. *Journal of Electroanalytical Chemistry*, Elsevier B.V. **656**, 114–9.
https://doi.org/10.1016/j.jelechem.2010.12.028

[83] Zhou, J., Huang, H., Xuan, J., Zhang, J. and Zhu, J.J. (2010) Quantum dots electrochemical aptasensor based on three-dimensionally ordered macroporous gold film for the detection of ATP. *Biosensors and Bioelectronics*, Elsevier B.V. **26**, 834–40.
https://doi.org/10.1016/j.bios.2010.05.021

[84] Deng, Y., Huang, W., Chen, X. and Li, Z. (2008) Facile fabrication of nanoporous gold film electrodes. *Electrochemistry Communications*, **10**, 810–3.
https://doi.org/10.1016/j.elecom.2008.03.003

[85] Kiani, A. and Fard, E.N. (2009) Fabrication of palladium coated nanoporous gold film electrode via underpotential deposition and spontaneous metal replacement: A low palladium loading electrode with electrocatalytic activity. *Electrochimica Acta*, **54**, 7254–9.
https://doi.org/10.1016/j.electacta.2009.07.037

[86] Chen, X., Wang, Y., Zhou, J., Yan, W., Li, X. and Zhu, J.J. (2008) Electrochemical impedance immunosensor based on three-dimensionally ordered macroporous gold film. *Analytical Chemistry*, **80**, 2133–40.
https://doi.org/10.1021/ac7021376

[87] Li, Y., Li, J., Xia, X.H. and Liu, S.Q. (2010) Direct electrochemistry of cytochrome c immobilized on a novel macroporous gold film coated with a self-assembled 11-mercaptoundecanoic acid monolayer. *Talanta*, Elsevier B.V. **82**, 1164–9. https://doi.org/10.1016/j.talanta.2010.06.036

[88] Jia, N., Cao, L. and Wang, Z. (2008) Platinum-coated gold nanoporous film surface: Electrodeposition and enhanced electrocatalytic activity for methanol oxidation. *Langmuir*, **24**, 5932–6.
https://doi.org/10.1021/la800163f

[89] Ciesielski, P.N., Scott, A.M., Faulkner, C.J., Berron, B.J., Cliffel, D.E. and Jennings, G.K. (2008) Functionalized nanoporous gold leaf electrode films for the immobilization of photosystem I. *ACS Nano*, **2**, 2465–72.
https://doi.org/10.1021/nn800389k

[90] Jia, F., Yu, C., Ai, Z. and Zhang, L. (2007) Fabrication of nanoporous gold film electrodes with ultrahigh surface area and electrochemical activity. *Chemistry of Materials*, **19**, 3648–53.
https://doi.org/10.1021/cm070425l

[91] Maaroof, A.I., Cortie, M.B., Gentle, A. and Smith, G.B. (2007) Mesoporous gold sponge as a prototype "metamaterial." *Physica B: Condensed Matter*, **394**, 167–70.
https://doi.org/10.1016/j.physb.2006.12.014

[92] Smith, G.B., Maaroof, A.I. and Gentle, A. (2007) Homogenized Lorentz-Drude optical response in highly nanoporous conducting gold layers produced by de-alloying. *Optics Communications*, **271**, 263–8.
https://doi.org/10.1016/j.optcom.2006.10.038

[93] Dixon, M.C., Daniel, T.A., Hieda, M., Smilgies, D.M., Chan, M.H.W. and Allara, D.L. (2007) Preparation, structure, and optical properties of nanoporous gold thin films. *Langmuir*, **23**, 2414–22.
https://doi.org/10.1021/la062313z

[94] Maaroof, A.I., Cortie, M.B. and Smith, G.B. (2005) Optical properties of mesoporous gold films. *Journal of Optics A: Pure and Applied Optics*, **7**, 303–9.
https://doi.org/10.1088/1464-4258/7/7/007

[95] Huang, J.F. and Sun, I.W. (2005) Fabrication and surface functionalization of nanoporous gold by electrochemical alloying/dealloying of Au-Zn in an ionic liquid, and the self-assembly of L-cysteine monolayers. *Advanced Functional Materials*, **15**, 989–94.
https://doi.org/10.1002/adfm.200400382

[96] Dourado, A.H.B., Silva, R.A., Torresi, R.M., Sumodjo, P.T.A., Arenz, M. and Cordoba de Torresi, S.I. (2018) Kinetics, Assembling, and Conformation Control of L-Cysteine Adsorption on Pt Investigated by in situ FTIR Spectroscopy and QCM-D. *ChemPhysChem*, **19**, 2340–8. https://doi.org/10.1002/cphc.201800380

[97] Zhang, Y., Yang, A., Zhang, X., Zhao, H., Li, X. and Yuan, Z. (2013) Highly selective and sensitive biosensor for cysteine detection based on in situ synthesis of gold nanoparticles/graphene nanocomposites. *Colloids and Surfaces A: Physicochemical and Engineering Aspects*, Elsevier B.V. **436**, 815–22. https://doi.org/10.1016/j.colsurfa.2013.08.016

[98] Martin, S.J., Frye, G.C., Ricco, A.J. and Senturia, S.D. (1993) Effect of Surface Roughness on the Response of Thickness-shear Mode Resonators in Liquids. *Analytical Chemistry*, **65**, 2910–22. https://doi.org/10.1021/ac00068a033

[99] He, H., Xie, Y. and Jiang, Y. (2011) A study of adsorption kinetics of alkanethiol and alkanedithiol on gold using cyclic voltammetry. *2011 International Conference on Information Science and Technology, ICIST 2011*, IEEE. 1248–53. https://doi.org/10.1109/ICIST.2011.5765067

[100] Hu, K. and Bard, A.J. (1998) In situ monitoring of kinetics of charged thiol adsorption on gold using an atomic force microscope. *Langmuir*, **14**, 4790–4. https://doi.org/10.1021/la971363o

[101] Sigma Aldrich. Cleaning Glassware. https://www.sigmaaldrich.com/technical-documents/articles/labware/cleaning-glassware.html

[102] Johnson, B.N. and Mutharasan, R. (2013) Regeneration of gold surfaces covered by adsorbed thiols and proteins using liquid-phase hydrogen peroxide-mediated UV-photooxidation. *Journal of Physical Chemistry C*, **117**, 1335–41. https://doi.org/10.1021/jp307983e

[103] Bewig, K.W. and Zisman, W.A. (1965) The wetting of gold and platinum by water. *Journal of Physical Chemistry*, **69**, 4238–42. https://doi.org/10.1021/j100782a029

[104] Dixon, M.C., Daniel, T.A., Hieda, M., Smilgies, D.M., Chan, M.H.W. and Allara, D.L. (2007) Preparation, structure, and optical properties of nanoporous gold thin films. *Langmuir*, **23**, 2414–22. https://doi.org/10.1021/la062313z

[105] Sieradzki, K., Erlebacher, J., Aziz, M.J., Karma, A. and Dimitrov, N. (2001) Evolution of nanoporosity in dealloying. **410**, 5–8.

[106] Nishio, K., Yuda, K. and Masuda, H. (2013) Fabrication of nanoporous gold film by electrochemical alloying and dealloying with li at room temperature. *ECS Electrochemistry Letters*, **2**, 3–5. https://doi.org/10.1149/2.009301eel

[107] Voss, R.F., Laibowitz, R.B. and Allessandrini, E.I. (1982) Fractal (scaling) clusters in thin gold films near the percolation threshold. *Physical Review Letters*, **49**, 1441–4. https://doi.org/10.1103/PhysRevLett.49.1441

[108] Smith, G.B., Maaroof, A.I. and Cortie, M.B. (2008) Percolation in nanoporous gold and the principle of universality for two-dimensional to hyperdimensional networks. *Physical Review B - Condensed Matter and Materials Physics*, **78**, 1–11. https://doi.org/10.1103/PhysRevB.78.165418

[109] Pan, W., Durning, C.J. and Turro, N.J. (1996) Kinetics of alkanethiol adsorption on gold. *Langmuir*, **12**, 4469–73. https://doi.org/10.1021/la9408634

[110] Bain, C.D., Troughton, E.B., Tao, Y.T., Evall, J., Whitesides, G.M. and Nuzzo, R.G. (1989) Formation of Monolayer Films by the Spontaneous Assembly of Organic Thiols from Solution onto Gold. *Journal of the American Chemical Society*, **111**, 321–35. https://doi.org/10.1021/ja00183a049